



Bruno Filipe Pinto Branco

Bachelor of Science in Chemical and Biochemical Engineering

Molecular Layer Deposition of Ultrathin Polyester Films

Dissertation submitted in partial fulfillment
of the requirements for the degree of

Master of Science in
Chemical and Biochemical Engineering

Adviser: Dr. ir. Jan Ruud van Ommen, Full Professor,
Technische Universiteit Delft

Co-adviser: Dr. Ana Isabel Nobre Martins
Aguiar de Oliveira Ricardo, Full Professor,
NOVA University of Lisbon

Examination Committee

Chairperson: Dr. Mário Eusébio, Assistant Professor, NOVA University of Lisbon
Rapporteur: Dr. César Laia, Assistant Professor, NOVA University of Lisbon
Member: Dr. Ana Aguiar Ricardo, Full Professor, NOVA University of Lisbon



FACULDADE DE
CIÊNCIAS E TECNOLOGIA
UNIVERSIDADE NOVA DE LISBOA

September, 2018

Molecular Layer Deposition of Ultrathin Polyester Films

Copyright © Bruno Filipe Pinto Branco, Faculty of Sciences and Technology, NOVA University Lisbon.

The Faculty of Sciences and Technology and the NOVA University Lisbon have the right, perpetual and without geographical boundaries, to file and publish this dissertation through printed copies reproduced on paper or on digital form, or by any other means known or that may be invented, and to disseminate through scientific repositories and admit its copying and distribution for non-commercial, educational or research purposes, as long as credit is given to the author and editor.

ACKNOWLEDGEMENTS

I would like to thank everyone who helped to get here and have the wonderful opportunity to work on this project.

Firstly, I want to express my gratitude to Prof. ir. J. Ruud van Ommen who welcomed me under his supervision and gave me the opportunity to do my thesis project in an interesting topic. I would like to thank my daily supervisor Damiano La Zara for all his support during this project. You taught me a lot not only project wise but also in new ways to look at things and to question everything. Thank you for all your patience to correct most of my writing and for the all the times I messed up in the lab. I would like to thank Prof. Dr. Ana Aguiar Ricardo for helping me. Thank you, Ankit Shekhar, for helping me with the photocatalytic tests.

A big thanks goes to the portuguese (with a bulgarian intruder) group of the Applied Sciences (Kostadin, Adriana and Cátia) with whom I spent most of my lunches and breaks during my project. A huge thanks to Cátia, the nicest aggressive person I met, who volunteered to read my entire thesis to correct it. A special thanks to Kostadin Petrov who made me company during the nights of the last few days of this project and made them easier to get through. I would also like to thank the amazing group of people I met during ESN trips and night-outs (Thea, Pietro, Daniel, Jordan, Jorris, Jernej, Diogo, May, Ross, Felix), you made my erasmus experience way better than ever thought it would be. To the danish girl who let me name her special friend, "hjemsøgt ansigt", and was always trying to get me more social.

Obviamente, que não podia esquecer aqueles três rapazes (Kostadin, Gonçalo e Patrícia) com quem passei a maior parte do tempo nos últimos 5 anos e especialmente o último ano em que basicamente tivemos a mesma morada durante umas semanas. Facilmente se ocupariam mais páginas com histórias nossas do que páginas de tese. Massa, Saibéssemos, Pupilas dilatadas, paredes que sofreram, 6 num churrasco, brincar com pinóquios e elefantes, disney, música irlandesa, novas unidades de medida do tempo, querer companhia para andar 10 m. Vocês tornaram a minha vida universitária muito mais engraçada e o caminho académico mais fácil. Muito obrigado Team Projecto.

Gostaria de agradecer também às pessoas que o secundário juntou neste caminho. Ao Nuno Aveiro por ser salvador de animais marinhos de grande porte e pelo abandono de pessoas em prol de comida e claro, mais conhecimento. À Catarina Simões por ser a companhia às 6h da manhã do primeiro dia de universidade e claro o seu amor incondicional

a animais.

À minha família académica (Inês Jóia, Filipa Bona e Rita Galrito) por terem feito a melhor escolha de sempre. À Inês Jóia por todos os momentos em que me deserdou, por todos os talheres e pelas vezes que íamos ao restaurante durante 4 anos para que eu pudesse estudar mais tranquilamente. À Filipa Bona, por ser, a amiga antes de afilhada e me apoiar nos bons e maus momentos. À Rita Galrito, pelo seu bom feitio e por ser uma surpresa que continuou sempre presente.

A todos aqueles que fizeram da faculdade o melhor possível (Ricardo Gouveia, Filipe Atouguia, João Calão, Ricardo Gomes, João Alves, Pedro Sobral, Crisanto Brito, André Silva, Miguel Domingues, Isabel Faustino, Ana Onofre).

Finalmente, quero agradecer à minha família e à minha namorada por todo o apoio e amor que me encorajaram nos tempos mais complicados.

This project has been a really excellent experience. Thank you all.

Este projecto foi realmente uma experiência excelente. Obrigado a todos.

"All things are difficult before they are easy."

Thomas Fuller

*"Study without desire spoils the memory, and it retains nothing
that it takes in."*

Leonard Da Vinci

ABSTRACT

Molecular Layer Deposition (MLD) is an attractive vapour-phase technique to deposit organic thin films with thickness control at the subnanometer level. Thus far, a large deal of research has been dedicated to study MLD on flat substrates. However, MLD on particle substrates is becoming increasingly relevant since depositing organic films is highly sought for several applications, such as controlled release of pharmaceutical and food products and protection of pigments.

This project focuses on the MLD growth of polyester films on both inorganic, TiO_2 , and organic particles, proteins. The deposition is executed in atmospheric-pressure fluidized bed reactors for a wide range of number of cycles, from 5 to 50, using either malonyl chloride or diethyl succinate as reactant, and either 1,2-butanediol or 1,4-butanediol as co-reactant. To verify the success of the process, the photocatalytic activity of MLD-coated TiO_2 and the dissolution behaviour of MLD-coated protein are tested.

FTIR and TGA show that the MLD growth on TiO_2 using malonyl chloride and 1,2-butanediol evolves linearly with the number of cycles, thus confirming one of the main characteristics of MLD. However, the film deposited with these precursors is not effective in suppressing the photocatalytic activity as the model pollutant is adsorbed by the coating. The MLD growth using diethyl succinate, independently of the diol, stops after a few cycles. Nonetheless, the photocatalytic activity of TiO_2 is reduced by one-half.

Regarding proteins, the MLD growth using malonyl chloride potentially leads to denaturation and thus to structural changes of the proteins, which affect the inherent dissolution behaviour. Therefore, no clear conclusion can be drawn by the comparison of the dissolution profiles of uncoated and MLD-coated proteins.

The results show that the only successful MLD approach for the deposition of polyesters involves the use of an acid dichloride (e.g. malonyl chloride) and a diol. However, it can only be applied to chemically stable particles as TiO_2 . Nonetheless, malonyl chloride changes the colour and thus the intrinsic photocatalytic properties of TiO_2 .

Keywords: Molecular Layer Deposition, polyester films, MLD growth, TiO_2 , Proteins, photocatalytic activity, dissolution behaviour

RESUMO

Deposição de camada molecular (MLD) é uma técnica de deposição na fase de vapor de filmes orgânicos finos que permite o controle da espessura ao nível subnanométrico. Até agora, a maioria dos estudos sobre MLD focaram-se na deposição em substratos planos. Contudo, a relevância de MLD em partículas tem aumentado devido ao interesse em depositar filmes orgânicos para diversas aplicações, tais como a libertação controlada de produtos farmacêuticos e alimentares e proteção de pigmentos.

Este projeto foca-se no crescimento por MLD de filmes de poliéster tanto sobre partículas inorgânicas, TiO_2 , como sobre partículas orgânicas, proteínas. A deposição é executada num reator de leito fluidizado à pressão atmosférica com um número de ciclos entre 5 e 50, usando cloreto de malonilo ou dietil succinato como reagente e 1,2-butanodiol ou 1,4-butanodiol como co-reagente. O sucesso do processo é verificado estudando a atividade fotocatalítica das partículas de TiO_2 revestidas por MLD e a dissolução das partículas de proteína revestidas por MLD.

A análise de FTIR e TGA mostram que o crescimento por MLD sobre TiO_2 usando cloreto de malonilo e 1,2-butanodiol evolui linearmente com o número de ciclos, confirmando uma das características principais da MLD. Contudo, o filme depositado com estes precursores não diminui a atividade fotocatalítica das partículas de TiO_2 , pois o poluente estudado é adsorvido pelo revestimento. O crescimento por MLD usando dietil succinato cessa após alguns ciclos, independentemente do diol utilizado. Porém, a atividade fotocatalítica de TiO_2 é reduzida para metade.

No caso das proteínas, o crescimento por MLD utilizando cloreto de malonilo provoca potencialmente a desnaturação, o que induz alterações estruturais nas proteínas, afetando assim a dissolução. Portanto, não pode ser retirada uma conclusão clara pela comparação dos perfis de dissolução de proteínas não revestidas e revestidas por MLD.

Os resultados obtidos mostram que a única abordagem com sucesso na deposição de poliéster envolve a reação entre um dicloreto ácido (e.g., cloreto de malonilo) e um diol sobre partículas quimicamente estáveis como as de TiO_2 . Todavia, o cloreto de malonilo modifica a cor destas partículas, alterando assim as suas propriedades fotocatalíticas.

Palavras-chave: Deposição de camada molecular, filmes de poliéster, crescimento de MLD, TiO_2 , Proteínas, actividade fotocatalítica, dissolução

CONTENTS

List of Figures	xv
List of Tables	xxi
Acronyms	xxiii
1 Introduction	1
1.1 Vapour-phase techniques for depositing thin films	1
1.2 Molecular Layer Deposition	2
1.3 Protection of Pigments	3
1.4 Controlled Release of Pharmaceutical and Food Products	4
1.5 Research Questions	5
1.6 Outline thesis	5
2 Theoretical Background	7
2.1 Molecular Layer Deposition	7
2.2 MLD on Particles: TiO ₂ and Protein	10
2.3 Fluidized Bed Reactors	11
2.4 Protection of Pigments	12
2.5 Controlled release of Pharmaceutical and Food Products	13
2.6 Characterization Techniques	13
2.6.1 Fourier Transform Infrared Spectroscopy	14
2.6.2 Thermogravimetric Analysis	15
2.6.3 Transmission Electron Microscopy	15
2.6.4 BET surface area Analysis	16
2.6.5 Ultraviolet-Visible Spectrophotometry	16
3 Experimental Procedure	17
3.1 Materials and Chemicals	17
3.2 Molecular Layer Deposition Setup	17
3.2.1 Coating of TiO ₂	18
3.2.2 Coating of Proteins	18
3.3 Characterization Techniques	19

CONTENTS

3.3.1	Fourier Transform Infrared Spectroscopy	19
3.3.2	Thermogravimetric Analysis	19
3.3.3	Transmission Electron Microscopy	19
3.3.4	BET-surface area analysis	19
3.4	Performance Testing	20
3.4.1	Photocatalytic Test	20
3.4.2	Dissolution Test	21
4	Results and Discussion	23
4.1	Molecular Layer Deposition on TiO ₂	23
4.1.1	Molecular Layer Deposition using Malonyl Chloride	23
4.1.2	Molecular Layer Deposition using Diethyl Succinate	30
4.2	Molecular Layer Deposition on Proteins	41
4.2.1	Molecular Layer Deposition using Malonyl Chloride	41
4.2.2	Molecular Layer Deposition using Diethyl Succinate as Reactant	47
5	Conclusion	49
6	Recommendations	53
	Bibliography	55
A	Overview of past Molecular Layer Deposition Experiments	71
B	Overview of the Experimental Work	73
B.1	Molecular Layer Deposition Experiments	73
B.2	Photocatalytic Experiments	77
B.3	Dissolution Tests	77
C	Characteristics of bare substrates	79
C.1	TiO ₂ P25 nanoparticles	79
C.2	Protein Particles	80
D	Fourier Transform Infrared Spectroscopy	83
E	Thermogravimetric Analysis	85
E.1	Interpreting a Thermogravimetric Curve	85
E.2	Calculation of the Loading and Thickness	86
E.3	Error propagation	87
F	Optimization of the operating conditions	89
G	Photocatalytic Test	95
G.1	Calculation of Kinetic Constant from UV-Vis	95

LIST OF FIGURES

1.1	Representation of different MLD growth models.	3
2.1	Representation of the precursor pulses in one MLD cycle on TiO ₂	7
2.2	Schematic representation of the MLD temperature window. Adapted from <i>Sundberg et al</i> [20]	8
2.3	Classification of particles in Gelgart A, B, C and D based on their particle size, d_p , and relative density, $(\rho_S - \rho_f)$. Adapted from Kunil and Levenspiel [97].	12
3.1	Chemical structure of Rhodamine B	20
4.1	FTIR spectra obtained for different number of MLD cycles on TiO ₂ using MC and 12BD. Figure (a) shows the spectra after being subtracted by the bare TiO ₂ spectrum in Kubelka-Munk units. Figure (b) shows a zoom of the FTIR spectra in the range 3100-2500 cm ⁻¹ . Figure (c) shows the peak area under the ester peak from 1808.930 cm ⁻¹ to 1685.507 cm ⁻¹ for all samples in (a). They were normalized with respect to highest one. The error bar represents the standard deviation.	24
4.2	Thermogravimetric analysis in air with an heating rate of 5°C.min ⁻¹ . Figure (a) shows the normalized weight as a function of temperature for increasing number of MLD cycles on TiO ₂ using MC and 12BD. These curves were consequently used to calculate the loading shown in Figure (b). The error bars, although they are too small to be visible, represent the uncertainty propagated in the TGA measurements.	25
4.3	Thickness estimated from the obtained loadings by TGA. The error bars represent the uncertainty propagated in the TGA measurements, the uncoated TiO ₂ diameter from BET and density of the coating. whereas the red line represents the linear fit of the data.	26

4.4	Figure (a) is a TEM picture of 50 MLD cycles coated TiO ₂ using MC and 12BD. The darker areas are TiO ₂ nanoparticles and it is possible to see that around most particles there is a lighter area which is the polyester coating. In (b), a comparison between the thicknesses estimated by TEM and TGA is given. The error bar in the TEM thickness represents the standard deviation obtained by measuring the thickness in three different parts of four different TEM pictures of the same sample. The red line represents the perfect agreement between the two methods.	27
4.5	TiO ₂ coated with 5, 20 and 50 MLD cycles using MC and 12BD.	28
4.6	UV-Vis spectra of bare TiO ₂ and MLD-coated TiO ₂ with MC and 12BD that were subjected to the photocatalytic test over time. In (a), (b) and (c) it can be seen the presence of the rhB by the peak present at $\lambda=554$ nm. In (d), the rhB peak is not present but two peaks around 360 nm and 400 nm appear.	29
4.7	rhB solutions with MLD-coated TiO ₂ after photocatalytic test and being centrifuged. In (a) and (b), it can be seen that the solution suffered discoloration over time. The numbers 0-9 correspond to 0, 5, 10, 15, 20, 30, 40, 50 and 60 minutes, respectively. In (c), the solution stayed with the same colour after the 60 minutes.	29
4.8	Figure (a) shows an aqueous solution with 50 MLD cycles coated TiO ₂ using MC and 12BD. Figure (b) is a comparison between the UV-Vis of the aqueous solution with coated TiO ₂ and the solution with rhB and coated TiO ₂	30
4.9	Subtracted FTIR spectra with increasing number of cycles of DS on TiO ₂ . These spectra were subtracted by the bare TiO ₂ spectrum in Kubelka-Munk units. These spectra were measured once.	31
4.10	Thermogravimetric analysis in air with an heating rate of 5°C.min ⁻¹ . Figure (a) shows the normalized weight as a function of temperature for increasing number of cycles of solely pulsing DS on TiO ₂ . These curves were consequently used to calculate the loading shown in Figure (b). The error bars, although they are too small to be visible, represent the uncertainty propagated in the TGA measurements.	32
4.11	Thickness estimated from the obtained loadings from TGA for increasing number of cycles with solely pulsing DS on TiO ₂ . The error bars represent the uncertainty propagated in the TGA measurements, the uncoated TiO ₂ diameter from BET and density of the coating.	32
4.12	FTIR spectra obtained for different number of MLD cycles using DS and 12BD. Figure (a) shows the spectra after being subtracted by the bare TiO ₂ spectrum in Kubelka-Munk units. Figure (b) shows the peak area under the ester peak from 1808.930 cm ⁻¹ to 1685.507 cm ⁻¹ for all samples in (a). They were normalized with respect to highest value. These spectra were measured once.	33

4.13 Thermogravimetric analysis in air with an heating rate o $5^{\circ}\text{C}\cdot\text{min}^{-1}$. Figure (a) shows the normalized weight as a function of temperature for increasing number of MLD cycles on TiO_2 using DS and 12BD. These curves were consequently used to calculate the loading shown in Figure (b). The error bars, although they are too small to be visible, represent the uncertainty propagated in the TGA measurements.	34
4.14 Thickness estimated from the obtained loadings from TGA for increasing number of MLD cycles with DS and 12BD on TiO_2 . The error bars represent the uncertainty propagated in the TGA measurements, the uncoated TiO_2 diameter from BET and density of the coating.	34
4.15 TEM picture of MLD-coated TiO_2 P25 nanoparticles after 50 cycles using DS and 12BD. The darker areas are TiO_2 nanoparticles. It was not possible to visualize any polyester film deposited on the particles.	35
4.16 FTIR spectra obtained for different number ofMLD cycles on TiO_2 using DS and 14BD. Figure (a) shows the spectra after being subtracted by the bare TiO_2 spectrum in Kubelka-Munk units. Figure (b) shows the peak area under the ester peak from 1808.930 cm^{-1} to 1685.507 cm^{-1} for all samples in (a). They were normalized with respect to highest value. These spectra were measured once.	36
4.17 Thermogravimetric analysis in air with an heating rate o $5^{\circ}\text{C}\cdot\text{min}^{-1}$. Figure (a) shows the normalized weight as a function of temperature for increasing number of MLD cycles on TiO_2 using DS and 14BD. These curves were consequently used to calculate the loading shown in Figure (b). The error bars, although they are too small to be visible, represent the uncertainty propagated in the TGA measurements.	37
4.18 Thickness estimated from the obtained loadings from TGA for increasing number of MLD cycles with DS and 14BD on TiO_2 . The error bars represent the uncertainty propagated in the TGA measurements, the uncoated TiO_2 diameter from BET and density of the coating.	37
4.19 Figure (a) and (b) are TEM pictures of MLD-coated TiO_2 P25 nanoparticles after 50 cycles using DS and 14BD. The darker areas are TiO_2 nanoparticles. Around most particles in (a) there is a lighter area which is the polyester coating. In (b) no coating is observable. In (c), a comparison between the thicknesses estimated by TEM in Figure (a) and TGA is given. The error bar in the TEM thickness represents the standard deviation obtained by measuring the thickness in three different parts of four different TEM pictures of the same sample. The red line represents the perfect agreement between the two methods.	38

4.20	Comparison between the 50 cycles on TiO ₂ using solely DS, 50 MLD cycles on TiO ₂ using DS and 12BD and 50 MLD cycles on TiO ₂ using DS and 14BD. Figure (a) shows FTIR spectra after being subtracted by the bare TiO ₂ spectrum in Kubelka-Munk units. Figure (b) shows the evolution of the loading with increasing number of cycles. The error bars represent the uncertainty propagated in the TGA measurements.	39
4.21	TiO ₂ P25 nanoparticles coated with 5 and 50 MLD cycles using DS and 14BD	40
4.22	UV-Vis spectra of MLD-coated TiO ₂ with DS and 14BD that were subjected to the photocatalytic test over time. In (a) and (b), it can be seen the presence of the rhB by the peak at $\lambda=554$ nm.	40
4.23	Figure (a) shows the evolution of $\ln(\frac{A_0}{A})$ over time for uncoated TiO ₂ P25 nanoparticles, 5 and 50 MLD cycles using DS and 14BD on TiO ₂ P25 nanoparticles. Figure (b) shows the kinetic constants calculated from (a). The kinetic constant for uncoated TiO ₂ P25 nanoparticles is represented as 0 cycles. The error bars represents the standard error as calculated by OriginPro 9 software.	41
4.24	Figure (a) shows the FTIR spectra obtained for different number of cycles of MLD using MC and 12BD while increasing the flow rate on protein after being subtracted by the bare protein spectrum in Kubelka-Munk units. Figure (a) shows the spectra Figure (b) shows the protein after being collected. The powder was fairly agglomerated however they were easily grinded afterwards.	42
4.25	FTIR spectra obtained for different number of cycles of MLD using MC and 12BD on protein and using a 4-port bottom windbox. Figure (a) shows the spectra after being subtracted by the bare protein spectrum in Kubelka-Munk units. Figure (b) shows the peak area under the ester peak from 1808.930 cm ⁻¹ to 1724.077 cm ⁻¹ for all samples in (a). All spectra were measured once.	43
4.26	Subtracted FTIR spectra obtained for 10 cycles of pulsing only one precursor on protein, heating the protein at 50°C and 10 complete MLD cycles using MC and 12BD. This spectra was subtracted by the bare protein spectrum in Kubelka-Munk units.	44
4.27	Normalized Absorbance at $\lambda=280$ nm of uncoated protein, 10 and 30 MLD cycles using MC and 12BD as a function of the time (a) until 30 minutes and (b) until 24 hours. The curves were normalized regarding the highest absorbance value.	45
4.28	Formation of strands during the dissolution of protein coated with 30 MLD cycles using MC and 12BD.	45
4.29	Normalized Absorbance at $\lambda=280$ nm of uncoated protein, heated protein, 10 MLD cycles using MC and 12BD and 10 cycles of solely pulsing one of the precursors as a function of the time until 30 minutes. The curves were normalized regarding the highest absorbance value.	46

4.30	Subtracted FTIR spectra obtained for different number of cycles using DS and 14BD on protein. This spectra was subtracted by the bare protein spectrum in Kubelka-Munk units.	47
4.31	Figure (a) shows the normalized absorbance at $\lambda=280$ nm of uncoated protein, 30 MLD cycles using DS and 14BD until 30 minutes. The curves were normalized regarding the highest absorbance value. Figure (b) shows the presence of strands after 30 min of dissolution of protein coated with 30 MLD cycles using DS and 14BD.	48
B.1	Molecular Layer Deposition Experimental Setup	74
B.2	Chemical Structure of both reactants and co-reactants used in this project.	75
C.1	FTIR spectrum obtained for bare TiO_2 measured in DRIFTS at room temperature.	79
C.2	Figure (a) is the thermogravimetric curve for bare TiO_2 in $100 \text{ ml}\cdot\text{min}^{-1}$ of air with an heating rate of $5^\circ\text{C}\cdot\text{min}^{-1}$ and (b) the respective first order derivative. As the derivative was too noisy (red), it was applied 50pt Savitzky-Golay smoothing in OriginPro 9.0 to observe the fundamental trend (green line).	80
C.3	FTIR spectrum obtained for bare protein measured in DRIFTS at room temperature.	81
C.4	Normalized Absorbance at $\lambda=280$ nm of uncoated protein as a funtion of the time (a) until 30 minutes and (b) until 24 hours. The curves were normalized regarding the highest absorbance value.	81
D.1	The procedure used in OMNIC 8.0 to calculate the ester peaks, C=O. As it can be seen, the range and baseline for integration can be adjusted.	84
E.1	Thermogravimetric curve for 50 MLD cycles of MC and 12BD on TiO_2 in $100 \text{ ml}\cdot\text{min}^{-1}$ of air with an heating rate of $5^\circ\text{C}\cdot\text{min}^{-1}$ (a) and the respective first order derivative (b). As the derivative was too noisy (grey), it was applied 50pt Savitzky-Golay smoothing in OriginPro 9.0 to observe the fundamental trend (blue line).	86
F.1	FTIR spectra obtained for different 12BD flow rates. Figure (a) shows the spectra after being subtracted by the bare TiO_2 spectrum in Kubelka-Munk units. Figure (b) shows the peak area under the ester peak from 1808.930 cm^{-1} to 1685.507 cm^{-1} for all samples in (a). They were normalized with respect to the highest one. These spectra were measured once.	89

F.2	Thermogravimetric analysis in air with an heating rate of $5^{\circ}\text{C}\cdot\text{min}^{-1}$. Figure (a) shows the normalized weight as a function of temperature for increasing flow rate of 12BD in MLD using MC and 12BD. These curves were consequently used to calculate the loading shown in Figure (b). The error bars, although they are too small to be visible, represent the uncertainty propagated in the TGA measurements.	90
F.3	Figure (a) shows the FTIR spectra after being subtracted by the bare TiO_2 spectrum in Kubelka-Munk units. Figure (b) shows the peak area under the ester peak from 1808.930 cm^{-1} to 1685.507 cm^{-1} for all samples in (a). These spectra were measured once.	91
F.4	Thermogravimetric analysis in air with an heating rate of $5^{\circ}\text{C}\cdot\text{min}^{-1}$. Figure (a) shows the normalized weight as a function of temperature for changing the pulsing flow rates and turning off the vibration. These curves were consequently used to calculate the loading shown in Figure (b). The error bars, although they are too small to be visible, represent the uncertainty propagated in the TGA measurements.	91
F.5	FTIR spectra obtained for different number of cycles for MLD using MC and 12BD at $T_{\text{Reactor}}=50^{\circ}\text{C}$ and $T_{\text{diol}}=50^{\circ}\text{C}$. Figure (a) shows the spectra after being subtracted by the bare TiO_2 spectrum in Kubelka-Munk units. Figure (b) shows the peak area under the ester peak from 1808.930 cm^{-1} to 1685.507 cm^{-1} for all samples in (a). The error bar represents the standard deviation.	92
F.6	Thermogravimetric analysis in air with an heating rate of $5^{\circ}\text{C}\cdot\text{min}^{-1}$. Figure (a) shows the normalized weight as a function of temperature for increasing number of MLD cycles on TiO_2 using MC and 12BD at $T_{\text{Reactor}}=50^{\circ}\text{C}$ and $T_{\text{diol}}=50^{\circ}\text{C}$. These curves were consequently used to calculate the loading shown in Figure (b). The error bars, although they are too small to be visible, represent the uncertainty propagated in the TGA measurements.	92
F.7	FTIR spectra obtained for different number of cycles of MLD using MC and 12BD at $T_{\text{Reactor}}=50^{\circ}\text{C}$ and $T_{\text{diol}}=90^{\circ}\text{C}$. Figure (a) shows the spectra after being subtracted by the bare TiO_2 spectrum in Kubelka-Munk units. Figure (b) shows the peak area under the ester peak from 1808.930 cm^{-1} to 1685.507 cm^{-1} for all samples in (a). These spectra were measured once.	93
F.8	Thermogravimetric analysis in air with an heating rate of $5^{\circ}\text{C}\cdot\text{min}^{-1}$. Figure (a) shows the normalized weight as a function of temperature for increasing number of MLD cycles on TiO_2 using MC and 12BD at $T_{\text{Reactor}}=50^{\circ}\text{C}$ and $T_{\text{diol}}=90^{\circ}\text{C}$. These curves were consequently used to calculate the loading shown in Figure (b). The error bars, although they are too small to be visible, represent the uncertainty propagated in the TGA measurements.	94

LIST OF TABLES

2.1	Physicochemical Properties of each substrate studied	11
2.2	List of the important organic groups for the identification of the deposited polyesters. The list was obtained from <i>Mayo et al</i> [104]	14
A.1	MLD precursors for: polyester, polyamide, polyimide, polyimine polythiourea, polyurea, polyurethane and polyacrylate. Adapted from D. La Zara[81] . . .	72
B.1	List of precursors with vapour pressure at the temperature inside the bubbler	75
B.2	MLD Experiments by Chronological order. T_{B-201} and T_{L-206} represent the temperatures for the reactant bubbler and line, respectively. T_{B-301} and T_{L-306} represent the temperatures for the co-reactant bubbler and line, respectively. T_{WB-401} and T_{R-401} are temperatures of the bottom windbox and reactor, respectively.	76
B.3	Photocatalytic Activity Tests by Chronological order	77
B.4	Dissolution Tests by Chronological order	77
E.1	Predicted polyester densities for each combination of precursors. The densities were estimated by setting up an oligomer consisting of ten repeating units. .	87
E.2	Expected Thickness for one layer of polyester according to each combination of precursors	87

ACRONYMS

12BD	1,2-butanediol.
14BD	1,4-butanediol.
ALD	Atomic Layer Deposition.
APS	(3-aminopropyl)triethoxysilane.
BET	Brunaur-Emmet-Teller.
CVD	Chemical Vapour Deposition.
DS	diethyl succinate.
FBR	fluidized bed reactor.
FTIR	Fourier Transform Infrared Spectroscopy.
GPC	growth per cycle.
MC	malonyl chloride.
MLD	Molecular Layer Deposition.
PET	polyethylene terephthalate.
PVD	Physical Vapour Deposition.
rhB	rhodamine B.
ROS	reactive oxygen species.
SE	Spectroscopic Ellipsometry.
STP	Standard Temperature and Pressure conditions.

ACRONYMS

TEM Transmission Electron Microscopy.

TGA Thermogravimetric Analysis.

UV Ultraviolet.

UV-Vis Ultraviolet-Visible Spectrophotometry.

XRR X-ray Reflexivity.

INTRODUCTION

1.1 Vapour-phase techniques for depositing thin films

There are many techniques for depositing thin films, one of them being Chemical Vapour Deposition (CVD). As the name indicates, it involves the formation of a thin solid film on a substrate by a chemical reaction between vapour-phase precursors. In this technique, two or more reactants are simultaneously introduced into a reaction chamber, where they react in the gas-phase to produce the desired material on the substrate surface. Therefore, it distinguishes itself from another technique, Physical Vapour Deposition (PVD) where atomic or molecular species adsorb on the substrate surface without reacting with it. However, the vapour-phase deposition methods currently employed, such as CVD and PVD cannot control the film growth nor the composition of the film[1–3].

Atomic Layer Deposition (ALD) and MLD, which are two vapour-phase techniques, have appeared as a response to the challenge of controlling the deposited film growth at the atomic level. These techniques allow the deposition of a conformal film and great control over the thickness and composition of this film by two sequential, self-limiting surface reactions of two precursors. The precursors are introduced into the reactor in alternating pulses which are separated by a purge pulse to remove any unreacted precursor or reaction by-products[2, 4–6]. In this manner, the precursors are chemisorbed onto the substrate instead of reacting on the gas-phase[3]. Typically, in ALD, the combination of a metal-containing compound, referred to as metal precursor, and an oxidizer, referred to as co-reactant, lead to the deposition of a metal or a metal-oxide. MLD is the organic counterpart of ALD and therefore instead of using metal precursors, it makes use of organic bifunctional precursors that undergo condensation polymerization reactions to yield organic polymers[4, 7].

1.2 Molecular Layer Deposition

Molecular layer deposition has seen a relevant development as a vapour-phase technique for the deposition of ultrathin organic films in many different applications such as microelectronics[2, 8], biomedical[9], luminescent materials[10, 11] and solar cell devices[12–14]. This deposition technique was developed during the 1990's by *Yoshimura et al*[15] to produce thin films of polyimides on a flat substrate. Since then, it has been an appealing method for the deposition of multiple organic polymers and currently hybrid inorganic-organic compounds such as titanocene, alucone, zincone, zircone[16].

The main advantage of MLD over other deposition techniques is that by relying on the same principle of self-limiting surface reactions as ALD, it provides precise control over multiple polymer film properties such as thickness, composition, morphology and conformality. MLD has been based on bifunctional monomers such as A-M-A and B-P-B, where “A” and “B” are the chemical functional groups, and “M” and “P” are the organic backbone[2, 17–20]. Both the organic backbone and organic functional groups of each monomer can be altered to tailor the film properties, i.e. chemical functionality, thermal stability, adhesion, and optical and electrical properties[21]. Ideally in MLD, each bifunctional precursor reacts with the surface merely with one functional group, adding a single monolayer per precursor pulse and thus by cycling between both precursors, a multilayer film can be achieved.[18]

Thus far, most research work on MLD focused on the deposition of the following polymers: polyimides[15, 22–26], polyureas[21, 27–32], polythiourea[33], polyurethanes[34], polyamides[17, 35–37], polyesters[7, 16], polyazomethines[38–42] and polyacrilates[43]. However, despite the extensive work to expand the applications of this technique and to develop new chemistries, little MLD work has been conducted on particles until now[16, 17, 35, 44]. The main reason for this is that MLD is mostly applied in microelectronics and energy-related devices which are preferably flat[7, 39, 43, 45, 46]. However, there is an increasing interest in applying MLD on particles as organic thin films with a well controlled thickness and composition are becoming more attractive for other applications such as controlled release of pharmaceutical and food particles[47, 48] and protection of pigments[49–51].

The major difference between MLD on particles and flat substrates is in the specific surface area, which is several order of magnitude higher for particles, resulting in longer pulse times to saturate the surface of the particles[52, 53]. The use of conventional ALD reactors, e.g. vacuum or viscous flow reactors, would bring economic problems as they lead to longer deposition times and lower precursor efficiency. Hence, when using high surface area substrates, i.e. particles, it is more appealing to use dedicated reactor designs, such as the rotary, the fixed bed reactor and fluidized bed reactor (FBR)[54]. The use of a FBR becomes attractive as these reactors ensure an efficient contacting between the vapour-phase precursors and the surface of the substrate, which is not verified with a fixed bed reactor. In addition, FBRs are also widely used for industrial processes and thus

the scale-up of MLD is feasible[44]. Despite also ensuring an efficient contacting between the precursors and the substrate, the rotary reactor due to the existence of moving parts and larger necessary volume, it is less appropriate for large scale operations[54]. Typically, most MLD experiments operate at low pressures as they facilitate lower pulse times and help mitigating the incorporation of impurities. Nonetheless, as the cost and complexity of vacuum equipment represent a big obstacle to scale-up of the process, there is a great effort to develop atmospheric pressure processes[17, 28, 54]. Hence, a scalable and cost-effective solution to satisfy industry requirements can be provided by atmospheric pressure FBRs[44].

Two major challenges arise in MLD, namely the deep understanding of the growth behaviour and the development of new coupling chemistries. In contrast to the vertical chain growth model that is typically used to illustrate MLD (Figure 1.1a), the polymer chains tend to have a severely tilted orientation, i.e. not aligning perpendicularly to the substrate surface (Figure 1.1b)[35], and to react twice with the surface due to the bifunctional reactants (Figure 1.1c) which decrease the overall growth[2, 20, 55]. The second challenge is the limited number of linking reactions as the absence of catalysts and solvents limit the type of reactions that can be applied to MLD. Therefore, MLD relies on the formation of polar linkages such as urea bonds[28–32], or ester bonds[7, 16]. For example, polyethylene, polystyrene and polyvinyl chloride cannot be deposited by MLD as there are no polar linkages in the backbones of these polymers. This shows that it is important to first study the fundamentals of MLD to understand how the growth proceeds on particles and what are the optimal precursors for the deposition of organic films.

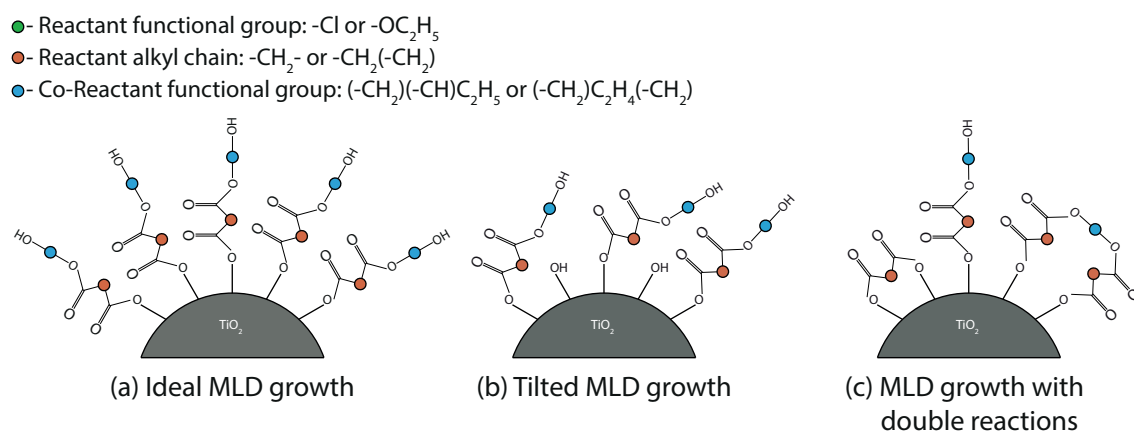


Figure 1.1: Representation of different MLD growth models.

1.3 Protection of Pigments

The bright white colour and great photostability of TiO_2 nanoparticles make them a highly attractive pigment for several industrial fields as paints, pharmaceuticals, plastics,

synthetic fibers, paper and cosmetics [49, 56–58]. However, due to their strong photocatalytic activity, these particles can cause degradation to materials around them when irradiated by ultraviolet radiation or sunlight. For instance, in paintings, the photocatalytic activity of TiO_2 causes the discoloration which reduces the lifetime of paintings[59, 60].

Currently, most studies about suppressing the photocatalytic activity of TiO_2 used ceramic oxides such as Al_2O_3 , SiO_2 , CeO_2 , ZrO_2 , NiO or CoO to cover the surface of the particles[60–64]. Nevertheless, organic coatings with the intent to suppress the photocatalytic activity have already been studied, however to a lesser extent than ceramic oxides, and proven to be efficient in reducing the photocatalytic activity[49–51]. *Liang et al* [62] reported that a 10 nm alucone film deposited by means of MLD onto TiO_2 lead to the complete suppression of the photocatalytic activity of TiO_2 . This shows that organic films are suitable for suppressing the photocatalytic activity of TiO_2 and thus MLD stands out as an excellent method for depositing organic films for protecting pigments.

1.4 Controlled Release of Pharmaceutical and Food Products

Controlled release systems currently represent one of the foremost areas of science as it involves multidisciplinary scientific approaches which contribute to human health care and well being[47]. Presently, there is a requirement for edible delivery systems to encapsulate, protect and release bioactive and functional constituents within the food and pharmaceutical industries[65, 66].

For instance, in the pharmaceutical industry these controlled release systems are mainly developed for slow release of drugs to decrease the fluctuation of drug concentration in plasma. Hence, the toxicity is reduced and the efficacy is increased since these systems do not easily degrade in the digestive tract before they get to the targeted organ and also improve patient compliance and convenience[16, 47, 67]. Furthermore, pharmaceutical companies by applying such method reduce the side effects of their old drugs and consequently save money on health care delivery[68].

In the food industry, controlled release systems are mainly utilized for protection of nutrients and to ensure the appropriate administration of heat- or oxidation-labile health actives[65, 69]. Delivery systems can be significantly useful for developing functional food designed to fight obesity, e.g. if such system can delay lipid digestion and increase the quantity of undigested food reaching the ileum, it can stimulate the ileal brake mechanism that modulates hunger, satiety and satiation[66, 70].

Proteins are emerging as the natural choice for nutraceuticals due to their high bioactivity and specificity. However, the administration of most of proteins is still limited to the parenteral route, i.e non-oral routes, since they degrade under the conditions found in the gastrointestinal tract[48, 71, 72].

There are two main methods used for controlled release of particles: the active ingredient can be embedded inside a polymeric matrix[73] or it can be coated by a polymeric

film[47, 74]. The latter allows control over the release time and targeting by either manipulating the thickness or composition[75, 76]. The complete control of these two aspects, thickness and composition, makes MLD an excellent candidate to produce new controlled release systems.

1.5 Research Questions

Based on the above described information, the main goal of this thesis was to understand how the growth of polyester films by means of molecular layer deposition evolves on both inorganic (i.e. TiO_2) and organic (protein) particles using different combinations of precursors, namely dichloride/diol and diester/diol.

In order to be able to achieve this goal, the following research questions were formulated:

1. Which operating conditions ensure the MLD growth of polyester films on TiO_2 nanoparticles using malonyl chloride and 1,2-butanediol?
2. How does the MLD growth proceed on organic particles such as protein containing $-\text{NH}_2$ surface groups?
3. Is it possible to grow polyester films by combining dialkyl diester (e.g., diethyl succinate) and diol (e.g., 1,2-butanediol or 1,4-butanediol)?
4. What is the influence of the MLD coating on the photocatalytic activity of TiO_2 P25 nanoparticles?
5. What is the effect of the MLD coating on the dissolution behaviour of the protein particles?

1.6 Outline thesis

In Chapter 2 the theoretical background for this project will be provided to support the choices made for experimental work and to support conclusions made from the results. In Chapter 3, the experimental procedure is described. In Chapter 4, the results are presented and discussed based on the given theoretical background. In Chapter 5, the conclusions of this project are summarized and in Chapter 6 a few recommendations are made based on the conclusions.

THEORETICAL BACKGROUND

2.1 Molecular Layer Deposition

MLD is a vapour-phase deposition technique based on two sequential, self-limiting, surface reactions[2, 4, 5]. This technique allows the deposition of conformal polymeric thin films on the surface of a substrate. The deposition is achieved by alternating pulses of two organic precursors which will react with the substrate surface rather than in the gas-phase. Between these pulses, a purge step with an inert gas, most commonly nitrogen gas, is applied to remove any unreacted precursor or reaction by-products. The inert gas is used as a carrier for the precursors as well. Normally, a MLD cycle consists of four steps: reactant, purge, co-reactant and purge again[1, 3, 77]. Hence, by simply adjusting the number of these cycles, the film thickness can be tuned[77]. Figure 2.1 represents the typical steps of one MLD cycle.

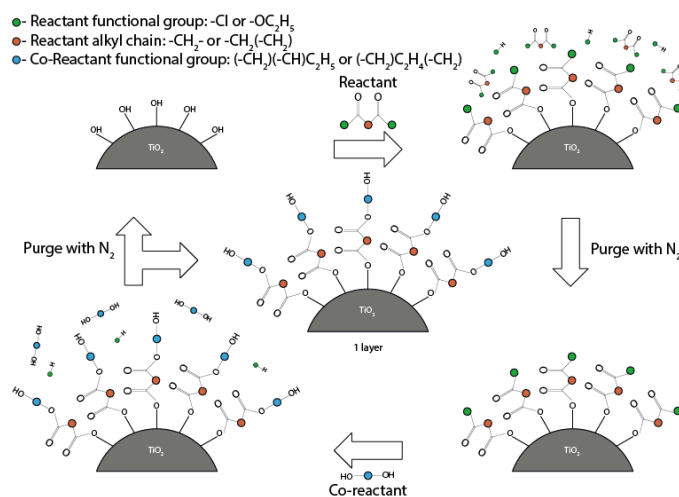


Figure 2.1: Representation of the precursor pulses in one MLD cycle on TiO₂

MLD, as well as ALD, is characterized by two major features, namely the linear growth of the film thickness with increasing number of cycles and saturation of the surface within one precursor pulse. The film growth is described in terms of growth per cycle (GPC), which represents the thickness increase in each cycle. Ideally, the GPC is constant and it is the slope of the plot of the evolution of the thickness as a function of the number of cycles[20, 35].

Usually, MLD growth depends on the deposition temperature. The temperature range where the GPC stays constant is called the MLD window as depicted in Figure 2.2. On one hand, at high deposition temperatures, the precursors may either desorb rapidly from the surface before the reaction takes place or decompose[2]. The desorption event is commonly attributed to a phenomenon named by *King et al*[78] as precursor-mediated reaction. On the other hand, at low deposition temperatures, the precursors may either condense in the reactor or not reacting on the surface.[1, 20, 55] However, low temperatures, that should be inside the MLD window, are preferable when performing MLD on organic particles, i.e. proteins, due to their temperature sensitive behaviour[79]. However, *Ivanova et al*[55] suggested that the MLD window is either fairly narrow or in some cases does not exist.

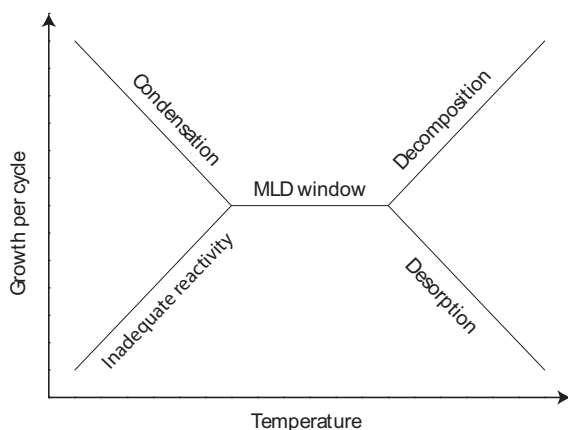


Figure 2.2: Schematic representation of the MLD temperature window. Adapted from *Sundberg et al*[20]

Even though much less experimental work has been done regarding MLD in comparison with ALD, the interest in this field is rising and more studies have arose in the last few years[55]. The major focus has been on the deposition of polyureas[21, 27–32], polyimides[15, 22–26], polyamides[17, 35–37] and polyazomethines[38–42]. Less work has described the MLD growth of polyesters[7, 16], polythioureas[33], polyurethanes[34] and polyacrilates[43]. Table A.1 in Appendix A shows the type of precursors used to deposit each of the referred polymer films. Thus far, most studies were done on flat substrates, e.g. Silica wafers, and not on particles[7, 17, 35, 39, 45, 46, 80]. This is due to ALD/MLD being mainly used in microelectronics and energy related devices which are preferentially flat[7, 39, 43, 45, 46]. In addition, precursor pulses for particles need to be several times higher than for flat substrates due to the higher specific surface area of particles[52, 53]. However, in the past years, the research work on MLD on particles has

increased mostly owing to the rising number of particle applications, e.g. protection of pigments and controlled release of pharmaceutical and food products. Such applications require films with a well controlled thickness and composition[16, 17, 35, 44].

Despite being a viable method for the deposition of thin films, MLD still faces many challenges that need to be addressed to improve its robustness and effectiveness in multiple applications. The main challenges are the profound understanding of the growth behaviour and the development of new and better coupling chemistries.

So far, most MLD related studies achieve a GPC lower than the length of one monomer. *Ivanova et al*[7] demonstrated the MLD of polyethylene terephthalate (PET), which is a polyester, on silica wafers. The surface of some wafers was functionalized with (3-aminopropyl)triethoxysilane (APS) to have amine groups on the surface. The results showed a better GPC with APS ($0.33 \text{ nm.cycle}^{-1}$) than without ($0.06 \text{ nm.cycle}^{-1}$) however these values only represent 33% and 6% of the monomer length, respectively. This low GPC was primarily attributed to the existence of double-reactions on the surface. These double reactions arise from the use of homobifunctional precursors, or in other words precursors that are terminated by the same functional group, and thus there is the decrease of the number of free active sites for the next step[2, 20, 55]. A study by *Bergsman et al*[32] showed the decrease of the GPC with increasing flexibility of the monomer chain. A more flexible precursor, i.e. the precursor has more aliphatic chains, has higher probability of reacting twice with the surface enabling more termination events to take place and thus reducing the overall growth rate. The low GPC was also attributed to a severely tilted orientation of the polymer chain[7, 20, 35, 36] which can cause steric hindrance and thus not allowing other precursor molecules to react with the substrate as shown by *Peng et al*[36]. *Peng* and his team observed the molecular orientation of films deposited by MLD using near-edge X-ray absorption fine structure (NEXAFS) spectroscopy. NEXAFS revealed significant tilting of the grown polymer with respect to the substrate normal.

Nevertheless, despite the occurrence of termination events as explained above, most MLD studies sustain constant film growth. It would be expected that by increasing the number of cycles, the number of active sites would decrease until all the sites were occupied and the growth rate completely ceased. A recent study by *Bent et al*[18] presented a possible explanation for this behaviour. It was suggested that new active sites are introduced into the organic film during the cycling process by either through absorption or adsorption of the precursors. They showed that on terminated surfaces of silicon wafers, the growth rate was initially slower than on un-terminated surfaces but eventually recovered and stayed constant after 16 cycles.

Another major challenge of MLD is the narrow number of linking reactions available due to the absence of solvent and catalyst in the vapour-phase. Thus far, MLD systems rely on the formation of polar linkages, i.e. ester, amide and urea bonds[2]. Deposition of polymers like polyethylene, polystyrene and polyvinyl chloride (PVC) is unfeasible due to the lack of these polar linkages. Therefore, novel strategies need to be studied to broaden the coupling chemistries applicable for MLD[2, 81].

Generally, in order to have an effective and well-controlled MLD process, the organic precursors must have high vapour pressure, high reactivity and show no, or weak, self-reactions[55]. To choose the ideal precursors for MLD, the first step is to examine their vapour pressures at the operating temperatures, which in this project were between 50°C and 120°C. If the vapour pressure is too low, i.e. less than 1 torr[81], around the operating temperatures, the precursors may not be suitable for MLD on heat-sensitive particles, e.g. protein particles. Therefore, polyimides and polyureas are not adequate as dianhydrides[82, 83] and diisocyanates[84] usually have low vapour pressures, as they are solid, at the lowest operating temperature. Polyesters and polyamides remain as appropriate coating materials since the vapour pressure of short aliphatic acid chlorides, diols and diamines are adequate[84–86]. Nevertheless, diamines are highly toxic in comparison with the diols and acid dichlorides[87–91]. Consequently, the deposition of polyester films was selected.

Ester bonds can be achieved as well by using a diacid as the carbonyl source as an alternative to acid dichlorides. However, diacids are solid at the room temperature and have too low vapour pressures at the operating temperatures[84]. The use of diesters as a carbonyl source is suggested by *J. Ruud van Ommen*[92] as they have suitable vapour pressure[84]. However, transesterification reactions are equilibrium reactions that require the presence of either an acid or a base catalyst[93, 94]. In *Ruud van Ommen's* work, it was also suggested that the catalyst could be added in the gas-phase or be present in the core material.

Previous work in the PPE research group of TU Delft, The Netherlands has shown low temperature deposition of polyester material using malonyl chloride (MC) and 1,2-butanediol (12BD)[16] and consequently, these two precursors were the major focus of this project. Other precursors such as diethyl succinate (DS), a diester, and 1,4-butanediol (14BD) were also tested even though no catalyst was employed.

2.2 MLD on Particles: TiO₂ and Protein

In this project, both inorganic and organic particles were studied. Titania P25 nanoparticles with $d_{1,0}=21$ nm were selected as the inorganic particles. These nanoparticles were studied as a model substrate to understand the optimal conditions to operate the MLD process and in addition the effect of the polyester film on their photocatalytic activity.

The organic particles studied were micron-sized protein particles which are used as dietary supplement for gluten-intolerant people. The used protein is a proline-specific endopeptidase or prolyl-oligopeptidase that is the only known dietary enzyme to successfully break down gluten in the stomach. Protein particles were studied as a model particle for organic particles to comprehend the feasibility of depositing polyester films by MLD and the influence of polyester thin films on its dissolution.

Table 2.1 shows some relevant physicochemical properties of each substrate used

during this project. Appendix C briefly describes the Fourier Transform Infrared Spectroscopy (FTIR) spectra of both bare TiO₂ and bare protein and the Thermogravimetric Analysis (TGA) curve for bare TiO₂.

Table 2.1: Physicochemical Properties of each substrate studied

Properties	TiO ₂	Protein
Density / g.cm ⁻³	4.1 [95]	N.A.
Surface Area / m ² .g ⁻¹	52.4	N.A.
Melting point / °C	1850 [95]	N.A.
Colour	White	Creamish

2.3 Fluidized Bed Reactors

In MLD, it is very important to ensure the contact between the precursors in the vapour-phase and the surface of the substrate. Furthermore, adequate mixing is necessary to make sure that all particles come into contact with the same amount of precursor[54]. Therefore, the ideal technology for coating bulk quantities of particles is gas fluidization[96] where the particles are suspended in a vessel in a fluid-like state by an up-flowing gas[97]. Moreover, FBRs provide excellent gas-particle heat and mass transfer as a consequence of the proper contact between the particles and the precursors in vapour-phase[98].

In FBRs, the fluidization of the particles is achieved when the pressure drop, Δp_{fb} , of gas passing through the fluidized bed is equal to the weight of the solids minus the buoyancy, divided by the cross-sectional area, A_t , of the reaction vessel as shown in Equation 2.1[98].

$$\Delta p_{fb} = \frac{A_t \times H \times (1 - \epsilon) \times (\rho_s - \rho_f) \times g}{A_t} \quad (2.1)$$

where H is the height of the bed, ϵ is the porosity of the bed divided by the total bed volume, ρ_s is the solids apparent density, ρ_f is the density of the fluid and g is the gravitic acceleration. To achieve this condition, the flow rate of the upward gas needs to exceed a certain limiting velocity, typically denoted by minimum fluidization velocity, v_{mf} [97].

In fluidization with gases, solids show characteristic differences in behaviour that also affect the operating characteristics of FBRs. Thus, particles are divided into four different classifications (A to D) regarding their particle size, d_p , and their relative density, $(\rho_s - \rho_f)$ as proposed by Geldart (Figure 2.3)[98]. Smaller particles are, typically, classified as Geldart A or C. The cohesive forces of Geldart C particles are stronger than the forces exerted by the fluid on the particles. Hence, this class of particles cannot be virtually fluidized without fluidization aids, e.g. assisting vibration[97, 98]. Due to their small size, both the TiO₂ and the protein particles studied in this project fall in the Geldart C classification.

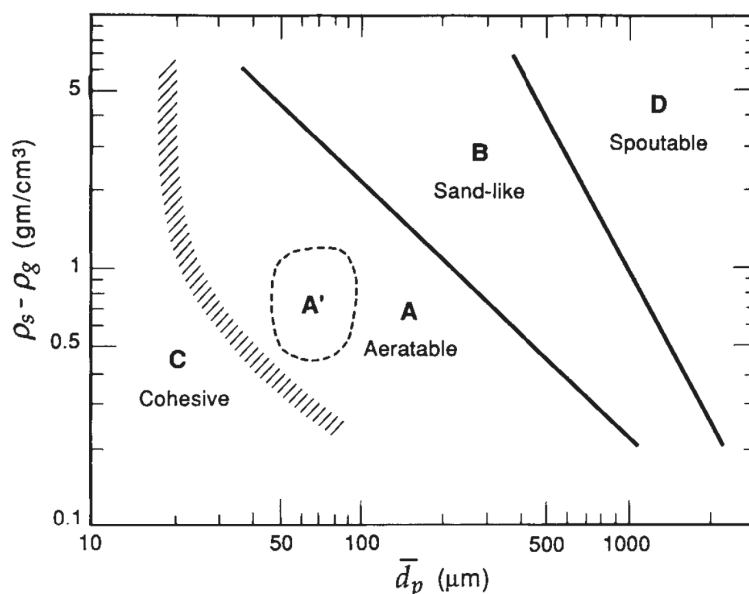


Figure 2.3: Classification of particles in Geldart A, B, C and D based on their particle size, d_p , and relative density, $(\rho_s - \rho_f)$. Adapted from Kunii and Levenspiel [97].

In contrast to micron-sized particles, nanoparticles do not fluidize individually but as very dilute agglomerates. Some nanopowders are able to fluidize without any sort of assistance with virtually no bubbles, large bed expansion and little elutriation whereas other nanopowders require significantly high superficial velocities to be fluidized and strong bubbling. Therefore, to fluidize these nanopowders some fluidization assistance such as vibration is needed[96].

2.4 Protection of Pigments

TiO_2 nanoparticles are widely used as a pigment due to its white colour and photostability. These particles are also largely used in sunscreens since they act as an inorganic Ultraviolet (UV) radiation filter owing to their high absorbance of UV radiation giving an extensive broadband protection across this whole electromagnetic region[49].

Nevertheless, due to their high photocatalytic activity, these particles tend to react with the surrounding materials, causing degradation, for example of paintings[59, 60]. Moreover, this irradiation-induced degradation of their surroundings also becomes a problem for sunscreens. In this case, the photoexcited species, formed by the interaction between UV light and TiO_2 nanoparticles, can react with other molecules, such as water, that are adsorbed on the surface of these particles producing reactive oxygen species (ROS). These ROS can cause cellular and even mutagenic damage[49]. As shown by *J. Wu et al*[99], after a long exposure, they induce significant oxidative stress potentially related to the formation of oxygen free radicals.

Most commonly, ceramic oxides are deposited on TiO_2 for suppressing its photoactivity. Ceramic oxides are chosen since they have the ability to prevent the transport of

electrons and holes caused by the absorption of UV light to the surface and have high transparency which conserves the white colour of TiO₂. Notwithstanding, a few studies reported the use of organic films to suppress the photocatalytic activity of TiO₂[49–51] *Morlando et al*[49] suggested a spray-drying method where TiO₂ nanoparticles would be encapsulated inside chitosan. In this work, a 10-fold decrease of the kinetic constant was observed when using a relative amount of chitosan to titania of 2:1. Also, a multicomponent polymer film with 11 nm was shown by *Lee et al*[51] to be also able to decrease almost entirely the photocatalytic activity of TiO₂ without affecting the core characteristics of these particles such as colour, UV absorption and sun protection factor. All in all, organic films seem to be a reasonable option for suppressing the photocatalytic activity of TiO₂ and hence, for protection of pigments.

2.5 Controlled release of Pharmaceutical and Food Products

The aim of controlled release of systems is to administer a constant concentration of one or more active ingredients over a specific length of time[81, 100]. In this way, the effectiveness of the ingredient can be increased while it is protected from different stimuli, e.g. pH and enzymes present in the gastrointestinal tract[48, 71, 72, 100].

Microencapsulation is the most used method to achieve controlled release of active ingredients. In this method, one or more materials are coated with or embedded within polymers[47, 74, 101]. Thus far, multiple polymers have been used to produce adaptable carriers of bioactive ingredients[102]. These polymers are generally hydrophobic, which is the case of the polyester studied in this project, to reduce water penetration and to lead to delayed diffusion and slowed release[81]. The controlled release can then be accomplished by modulating the environment temperature, formula of copolymer and the concentration of active agent[75, 76]. The full control of the thickness and composition of the polymer film is then a very important feature for controlled release systems. Hence, MLD is an excellent candidate to attain this new kind of active ingredient delivery systems[16].

2.6 Characterization Techniques

It is highly important to measure the thickness of the achieved coating since MLD is mainly characterized by the GPC. The main characterization techniques employed during this project were FTIR and TGA. To further characterize the particles, other characterization techniques such as Transmission Electron Microscopy (TEM), Brunaur-Emmet-Teller (BET) surface adsorption and Ultraviolet-Visible Spectrophotometry (UV-Vis) were employed.

Generally, on flat substrates the film thickness is analysed by Spectroscopic Ellipsometry (SE), X-ray Reflexivity (XRR) or TEM. However, SE and XRR can only be used with flat substrates and thus they were not used. TEM visualization of nanoscale deposited

organic films is easier on an inorganic substrate than on an organic substrate since areas with higher mass, e.g. TiO_2 , appear darker than regions with lower mass, e.g. proteins. Furthermore, the studied protein particles were micron-sized and thus they are too large to be analysed under TEM.

2.6.1 Fourier Transform Infrared Spectroscopy

FTIR is a characterization technique that allows the determination of structural characteristics of molecules by their interaction with infrared light, focusing on the mid-infrared region: $4000\text{-}400\text{ cm}^{-1}$. FTIR can be performed in different modes, e.g. transmission or diffuse reflectance (DRIFTS) mode. In transmission mode, potassium bromide (KBr) pellets are used to get the infrared spectra of powders. Despite the beam passing through the whole sample in this mode, principally bulk contributions are emphasized whereas surface contributions are minimized. KBr is used as it is inert and transparent for wavenumbers above 400 cm^{-1} . In DRIFTS mode, mainly surface contributions are recorded and sample preparation is quicker as the mix sample/KBr powder is just placed in the metal cup instead of having to prepare a pellet. The quantitative analysis of DRIFTS spectra should always be done in Kubelka-Munk units which is a reflectance unit. Therefore, the obtained spectra should always be converted from absorbance units to Kubelka-Munk units[103].

This technique was the most important method to characterize the coated particles throughout this project as it is the single one that enables the analysis of both substrates used. Table 2.2 shows the absorption peaks of interest in MLD of polyester films from MC, DS and diols[104].

Table 2.2: List of the important organic groups for the identification of the deposited polyesters. The list was obtained from Mayo *et al*[104]

Group	Type	Wavenumber / cm^{-1}	Signal
O-H (stretch)	Water	3450-3200	strong
C-H (stretch)	alkyl	3000-2800	strong
C=O (stretch)	Acid Halide	1880-1800	strong
C=O (stretch)	ester	1755-1735	strong
C=O (stretch)	aldehyde	1735-1720	strong
C=O (stretch)	Carboxylic Acid	1720-1706	strong
O-H (stretch)	Water	1640	strong
C-O (stretch)	ester	1250-1000	strong

It is not expected that all of these peaks appear if the coating process was successful. For instance, the carbonyl bond, $\text{C}=\text{O}$, at $1880\text{-}1800\text{ cm}^{-1}$ will only arise if part of the MC did not react. The most important peaks are the ester carbonyl peak around $1755\text{-}1735\text{ cm}^{-1}$ and the C-H peaks around $3000\text{-}2800\text{ cm}^{-1}$ since their arising guarantees the occurrence of reaction. The C-H peaks arise due to the methyl and methylene groups present in 12BD and 14BD, respectively.

A qualitative evaluation of the amount of polyester deposited can be done by analysing the ester carbonyl peak in the FTIR spectra[17, 35]. The integrated area under the ester carbonyl peak can be plotted as a function of the number of cycles giving an idea of the evolution of the amount of polyester deposited (see Appendix D). It is then possible to compare samples with different operating conditions such as number of cycles and temperature. However, these results are not as accurate as TEM, XRR and SE[35].

2.6.2 Thermogravimetric Analysis

Thermal Gravimetric Analysis consists of a pan where the sample is placed and it is supported by a high-precision balance. The pan is in a furnace that can be heated during the analysis. The mass of the sample is monitored throughout the heating in a pre-established and controlled atmosphere. The sample can be analysed under different conditions such as vacuum, a reactive gas as air or an inert gas as helium (He) or nitrogen (N_2). Since polyester is an organic molecule, it will combust if it is analysed under an oxidative atmosphere such as air or oxygen (O_2) or it will pyrolyse if it is analysed under an inert atmosphere such as N_2 . The former allows the determination of the amount of material that was deposited on the samples surface as shown in Appendix E. This technique can only be applied to evaluate the deposited material on TiO_2 since proteins would also decompose during the TGA[79, 105, 106].

2.6.3 Transmission Electron Microscopy

The Transmission Electron Microscope works on the same fundamental principles as the optical microscope but instead of light it uses an electron beam. A high energy electron beam passes through a very thin sample in a vacuum atmosphere and parts of it are transmitted whereas others are diffracted depending on the thickness and electron transparency of the sample. The transmitted part is focused by an objective lens into an image on a phosphor screen, creating light and allowing the user to observe the image. The amount of diffracted electrons will dictate the image contrast. In this way, the inner structure of the sample can be observed. The darker areas of the image arise due to heavier atoms that deflect more electrons whereas the lighter areas appear due to lighter atoms where more electrons can be transmitted through[107, 108]. Since protein particles and the polyester coating mainly consist of carbon atoms, it is not expected to be able to observe a contrast between the substrate and the coating. Consequently, this technique is only viable to analyse the coating on TiO_2 particles as the contrast between these heavier particles and the polyester is higher.

2.6.4 BET surface area Analysis

BET surface area analysis provides precise specific area evolution of materials by measuring the physisorption of N_2 gas as a function of the relative pressure. This determination is normally executed at the temperature of liquid nitrogen. From this method, two isotherms are obtained: an adsorption isotherm and a desorption isotherm. The BET adsorption isotherm equation, as represented in Equation 2.2, is fitted to the obtained isotherm curve and hence the specific surface can be calculated by Equation 2.3[109, 110]:

$$\frac{1}{V_\alpha \left(\frac{P_0}{P} - 1 \right)} = \frac{C - 1}{V_m C} \frac{P}{P_0} + \frac{1}{V_m C} \quad (2.2)$$

$$S_{BET} = \frac{V_m N_A \alpha}{V_{molar}} \quad (2.3)$$

where V_α represents the volume of the gas adsorbed at Standard Temperature and Pressure conditions (STP) conditions, P_0 is the saturated pressure of adsorbate gas, P is the partial pressure of adsorbate gas in equilibrium with the surface, C is a dimensionless constant that is related to the enthalpy of adsorption of the adsorbate gas on the sample and V_m is the volume of gas adsorbed at STP conditions to produce an apparent monolayer on the sample surface. N_A is the Avogadro constant, α is the effective cross-sectional area of one adsorbate molecule ($\alpha_{N_2} = 0.162 \text{ nm}^2$) and V_{molar} is the molar volume at STP conditions (assumed as 22.4 dm^3). As the surface area is related to the particle diameter by Equation E.3, this analysis can be used as well to evaluate the thickness of the deposited film.

2.6.5 Ultraviolet-Visible Spectrophotometry

UV-Vis is based on the principle that compounds absorb or transmit light over a defined interval of wavelengths if they possess chromophores such as aromatic nitro, azoxy, nitroso, carbonyl or azo groups[111]. A UV-Vis spectrophotometer is able to measure the intensity of a light beam, with variable wavelength from 185 to 700 nm, after it passed through a sample solution. The absorbance value given by this instrument can then be related to the concentration of the solution by Lambert-Beer's Law (Equation 2.4):

$$A = \epsilon \cdot l \cdot C \quad (2.4)$$

where A is the absorbance, ϵ is the molar extinction coefficient or molar absorptivity, l is the path length and C is the sample concentration. UV-Vis is a useful tool to analyse the results from dissolution and photocatalytic tests since it is able to indirectly measure a solution's concentration and thus monitor the amount of material dissolved at a certain moment during the test.

EXPERIMENTAL PROCEDURE

3.1 Materials and Chemicals

Crystalline TiO₂ P25 nanoparticles were purchased from *Evonik Aeroxide*[®] and prior to being used, they were sieved at a cut-off size of 150 μm for 20 min. Sieved TiO₂ nanoparticles were stored in an oven at 120°C for 12 hours. Protein particles were obtained from *Royal DSM* and stored in the fridge at 4°C.

Malonyl Chloride (97%), diethyl succinate ($\geq 99\%$), 1,4-butanediol (99%) and rhodamine B ($\sim 95\%$) were purchased from *Sigma-Aldrich*. Malonyl chloride was kept in the fridge after each experiment and it was replaced after at least 1 week of usage to avoid any decomposition. 1,2-butanediol ($\geq 98\%$) was acquired from *Fluka-analytical* and *Sigma-Aldrich*.

3.2 Molecular Layer Deposition Setup

Polyester thin films were deposited on different particle substrates using a fluidized bed reactor. The reactor consisted in a vertical glass tube with an inner diameter of 2.6 cm and a length of 50 cm with a thermocouple inserted inside the powder bed. When the pulses' flow rate was not enough to fluidize the particles, the reactor was attached to a mechanical vibration table (*PAJA Triltechnik*) with a frequency of 44-45 Hz. The vibration causes the breaking of agglomerates that could be formed thus helping the powder fluidization during the coating process. Attached to the bottom and top of the reactor there were two windboxes with one distributor plate each. To the bottom windbox, it was connected the inlet to the reactor, a type K thermocouple and an outlet for the manometer. To the top windbox, there were the outlet of the reactor and an inlet for backflow, used after every purge to prevent the powder getting stucked to the top distributor plate

avoiding in this way a pressure drop increase.

As seen in Figure B.1, there were three different sets of lines, one for each precursor and a third one for nitrogen gas at room temperature used as purge. The lines were connected at a mixing point before entering the reactor. The precursors were preheated inside bubblers which were placed in *Isopad*TM heating mantles and the temperature was measured by means of a type K thermocouple inserted in the precursor liquid. Table B.1 shows the temperatures and vapour pressures at which each precursor was kept inside the bubbler. The precursor gas in the bubblers was carried to the reactor by flowing nitrogen gas.

The unreacted gases after exiting the reactor flowed through four vessels as shown in Figure B.1. The second and third one were filled kaydol oil and sodium hydroxide, respectively, to clean the outlet gases of organic compounds and neutralize the hydrochloric acid arisen from the reaction between MC and 12BD. The first and last one are empty in order to prevent any backflow from the second vessel going to the reactor and any sodium hydroxide from the third one going into the building vents and damaging them, respectively. After the last vessel, there was a nanoparticle filter to impede nanoparticles from also going into the building vents.

The control of temperature in this process is an essential point as slight variations can induce problems such as substrate decomposition or condensation of the precursors inside the lines. The reactor temperature was maintained constant at a temperature between 50 and 120°C using an infrared lamp. This temperature was measured by inserting a type K thermocouple in the particle bed. Precursor lines (L-20# and L-30#) were wrapped in heating and isolating tape with type K thermocouples attached since the temperature in the line has to be higher than the bubbler's to avoid any precursor condensation inside these lines.

3.2.1 Coating of TiO₂

For the coating of TiO₂ nanoparticles, the reactor was filled with 1.5 g of sieved TiO₂, weighed prior to being stored in the oven. The nanoparticles were fluidized by a N₂ flow assisted by vibration only when needed. The operating conditions used for each experiment are present in Table B.2.

3.2.2 Coating of Proteins

For the coating of protein particles, the reactor was filled with 10 g of protein. The operating conditions used for each experiment are present in Table B.2. In experiments number 18 and 24, a four-port winbox was used. The fourth port was used to continuously send N₂ to be able to fluidize the particles. All the samples were later stored in the fridge to avoid further denaturation of the enzyme.

3.3 Characterization Techniques

Samples using TiO₂ as substrate were always characterized *ex-situ* by FTIR and TGA. Some samples were also characterized by TEM. Samples using protein were only characterized by FTIR.

3.3.1 Fourier Transform Infrared Spectroscopy

FTIR analyses were executed in diffuse reflectance mode on a Nicolet 8700 spectrometer (*ThermoFisher Scientific*) equipped with a DTGS (Deuterated Triglycine Sulfate) detector. Before analysing the samples, a background was made using a freshly grinded potassium bromide sample, KBr (99+% FTIR grade, *Harrick Scientific Corporation*). The spectra were recorded over the range of 4000-400 cm⁻¹ using a resolution of 4 cm⁻¹ and 128 scans. The spectra were then analysed using the software OMNIC 8.0 (*ThermoFisher Scientific*). Since DRIFTS spectra should be analysed in Kubelka-Munk units, all spectra were firstly converted from absorbance units using an OMNIC 8.0 built-in function. This enabled to qualitatively evaluate the deposition of polyester films by calculating the integrated area under the ester peak (C=O) in different ranges. These measurements were performed three times to estimate the error in this analysis unless otherwise specified.

3.3.2 Thermogravimetric Analysis

TGA's were performed using a TGA2/SF1100 STAR^e system (*METTLER TOLEDO*). All samples were heated in the range of 30°C-600°C under an air flow of 100 mL.min⁻¹ with an heating rate of 5 K.min⁻¹. The analysed samples had an initial mass between 5 mg to 7.5 mg. Similar to FTIR, this analysis were performed in three different instances in time. This is only false when the collected powder was not enough to execute it.

3.3.3 Transmission Electron Microscopy

To prepare the samples for TEM, the powders were dispersed in the dry phase on copper TEM grids. The images from TEM were recorded at several locations in the sample by a JEM-1400 transmission electron microscope (*JEOL*) operating at a voltage of 120 kV and a current density of 10 to 30 pA.cm⁻²

3.3.4 BET-surface area analysis

Physisorption of N₂ at 77 K was done on a TriStar II 3020 (*Micromeritics Instrument Corp*). Before doing the physisorption of N₂, the samples were degassed at room temperature over 24 h.

3.4 Performance Testing

The next two sections, Subsection 3.4.2 and Subsection 3.4.1, will explain how the dissolution and the photocatalytic tests were performed.

3.4.1 Photocatalytic Test

In this test, the concentration of rhodamine B (Figure 3.1), a model pollutant, in a continuously stirred photocatalytic slurry reactor was measured over time. This provided a profile of the concentration from which a kinetic constant could be calculated as described in Section G.1. To prepare the samples, 30 mg of powder was added to a 30 ml solution of RhB with a concentration of 12 mg.l^{-1} along with a 1.5 cm magnetic stirrer in a 100 ml glass beaker. The samples were placed onto a stirring plate for 5 minutes and after they were mixed in an ultrasonic bath for 10 minutes at room temperature.

Afterwards, the samples were taken to the Atlas Suntest XXL+ sun simulator and placed inside a water bath and onto a RO 15 power *IKAMAG*® magnetic stirring plate with 15 different stirring positions. The water bath was maintained at 20°C using a *Watson Marlow* 323 peristaltic pump and a *Julabo* FL300 recirculating cooler. All samples were stirred for 20 minutes inside the closed sun simulator without any irradiation.

Subsequently, the samples were irradiated by Xe lamps in the range of 300-400 nm with an irradiation power of 45 W/m^2 . Samples of 1 ml were taken from solutions at different instances with a *Gilson* apipatman P1000 and placed in a 1.5 ml vial. These vials with solution were covered by aluminium foil to prevent any additional degradation of the model pollutant.

Afterwards, all the vials were centrifuged for 10 min at 12500 rpm in a *Thermo Scientific* MicroCL 21R. With a *Gilson* apipatman P100, 0.4 ml was taken from the supernatant and placed in another vial. The remaining solution was centrifuged again for the same time and speed. Once again, 0.4 ml was taken and placed in the same vial as previously.

From these new vials, 0.4 ml was taken and analysed by *ex situ* UV/Vis using a *HACH LANGE* DR 5000™ UV-Vis Spectrophotometer in the range of 350 to 700 nm as the maximum absorbance of rhodamine B (rhB) is at $\lambda_{\text{max}}=554 \text{ nm}$.

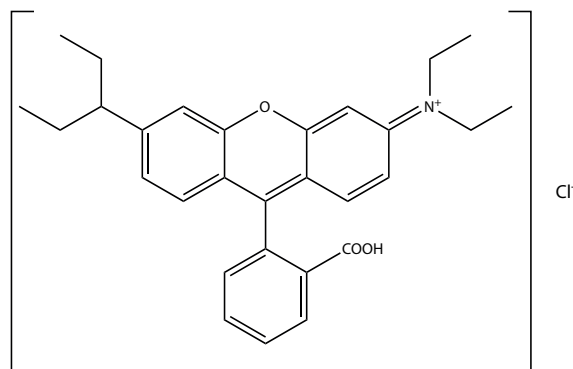


Figure 3.1: Chemical structure of Rhodamine B

3.4.2 Dissolution Test

The dissolution tests were performed at room temperature and using a stirring rate of 8 Mot which corresponds to roughly 880 rpm. It was used 100 mg of sample in 100 ml of deionized water to execute the dissolution test. The dissolution was monitored by taking around 2 ml of solution and filtering it through a 0.22 μ l pore size polyvinylidene difluoride membrane (*Millex*[®]) and then analyzing it *ex situ* UV/Vis using a *HACH LANGE* DR 5000[™] UV-Vis Spectrophotometer. Before any measurements, a blank measurement was made using deionized H₂O. All measurements were made in the range of 240-320 nm, since the maximum absorbance for the used protein is at $\lambda_{\text{max}}=280$ nm.

RESULTS AND DISCUSSION

In this Chapter, the results of the experiments at high reactor temperature, meaning $T_{R-401} \geq T_{\text{precursor bubblers}}$, with TiO_2 and the experiments with proteins described previously will be shown. In Section 4.1, the deposition of polyester films on TiO_2 P25 nanoparticles using different precursors will be presented. More specifically, the MLD processes using MC and DS as a first precursor are presented in Subsection 4.1.1 and 4.1.2, respectively. In section 4.2, the results of the MLD experiments on proteins will be discussed.

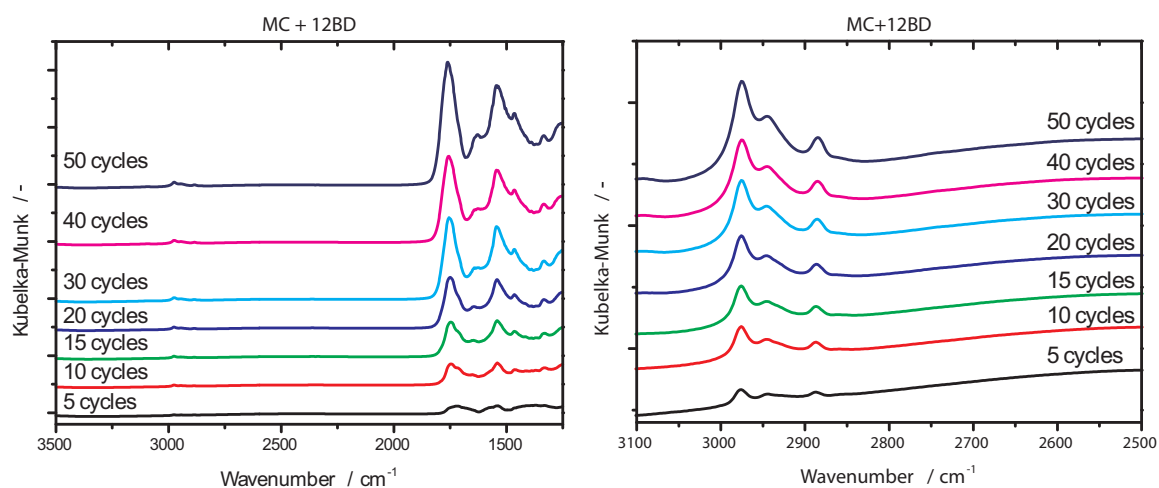
4.1 Molecular Layer Deposition on TiO_2

4.1.1 Molecular Layer Deposition using Malonyl Chloride

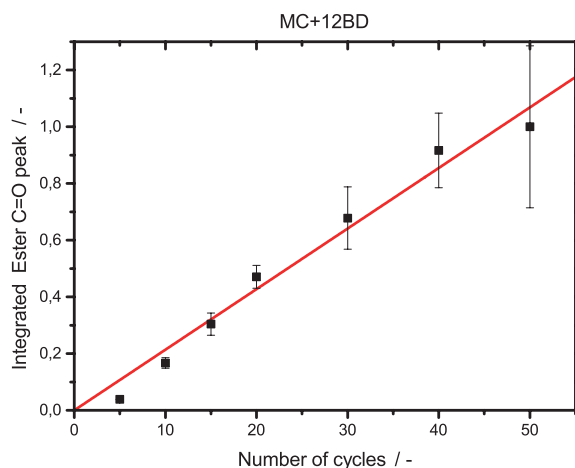
In this section only the experiments with reactor and windbox temperatures higher than the precursor bubbler temperatures will be considered. By using these conditions, it was ensured that no condensation occurred neither inside the bottom windbox nor inside the reactor and thus a proper MLD process was performed. The set of experiments with lower temperatures and/or lower flow rates, experiments identified with number 1-9, 14 and 16 in Table B.2, were performed to understand the optimal conditions to operate the setup when using MC and 12BD as precursors. A brief discussion of these experiments is present in Appendix F.

In order to study the evolution of the growth using MC as reactant and 12BD as a co-reactant, an experiment up to 50 cycles was performed. During the experiment, samples were collected after 5, 10, 15, 20, 30 and 40 cycles. In this way, it is guaranteed that all these samples were under the same operating conditions.

The FTIR spectra for each sample are shown in Figure 4.1. The ester peak $\text{C}=\text{O}$ between 1735 and 1755 cm^{-1} is present in all samples except on the 5 cycles one. This



(a) Subtracted FTIR spectra with increasing number of cycles. (b) Subtracted FTIR spectra between 3100 to 2500 with increasing number of cycles.



(c) Normalized ester peak area from 1808.930 to 1685.507 cm⁻¹.

Figure 4.1: FTIR spectra obtained for different number of MLD cycles on TiO₂ using MC and 12BD. Figure (a) shows the spectra after being subtracted by the bare TiO₂ spectrum in Kubelka-Munk units. Figure (b) shows a zoom of the FTIR spectra in the range 3100-2500 cm⁻¹. Figure (c) shows the peak area under the ester peak from 1808.930 cm⁻¹ to 1685.507 cm⁻¹ for all samples in (a). They were normalized with respect to highest one. The error bar represents the standard deviation.

sample shows a peak around 1720 cm⁻¹ which is also related to a C=O bond but it is predominantly determined by the presence of a carboxylic acid[104]. This can be an indication that part of the MC reacted with some moisture present on the surface of TiO₂[112] since it is widely known that the surface of TiO₂ nanoparticles contains water[113]. There is also the presence of three distinct peaks in the range 3000-2880 cm⁻¹ that appear due to the C-H stretch of methyl (CH₃) and methylene (CH₂) groups as shown in Figure 4.1b. The peak at 2974 cm⁻¹ can be attributed to the asymmetric CH₃ stretch whereas the peaks at 2945 cm⁻¹ and 2884 cm⁻¹ are due to the symmetric CH₃ stretch split due to Fermi resonance. Methylene C-H stretch peaks are expected to have a low intensity since only short alkyl chains are deposited [104, 112, 114, 115]. Since the methyl groups emerge due to the reaction with 12BD, the increase of both the CH₃

stretches and the ester C=O peak with the number of cycles is further proof that the precursors have reacted on the surface of TiO₂ to form a polyester film. Another peak at 1545 cm⁻¹ appears in every spectra and it shows an increase with increasing cycles. This peak is typically assigned to the carboxylate ion (COO⁻) which can most probably be due to the interaction of carboxylic groups with the TiO₂ surface[116].

In Figure 4.1c, the normalized integrated area under the ester peak between 1808-1685 cm⁻¹ as a function of the number of cycles is shown. It is possible to observe that the area under the peak linearly increases with the number of cycles, thus substantiating one of the key characteristics of the MLD process. Each sample was analysed by FTIR in three different instances in time as explained in Appendix D. The high standard deviations observed are due to the time difference between FTIR analysis, which was around three weeks, suggesting that the polyester coating from this combination of precursors is not stable for large periods of time, i.e. one month.

These samples were also analysed by TGA and the respective curves are represented in Figure 4.2a. The weight loss between 120°C and 500°C, which is attributed to the loss of the polyester coating, increases with increasing the number of cycles. Figure 4.2b shows the calculated loading, which represents the weight loss between 120°C and 500°C, for each sample. In Appendix E, there is a brief demonstration of the calculation of the loading and respective error. The trend of the calculated loading is found to be quite linear. The linear evolution of both the integrated ester peak area from FTIR and the weight loss from TGA with the number of cycles is a strong indication of the success of the MLD process.

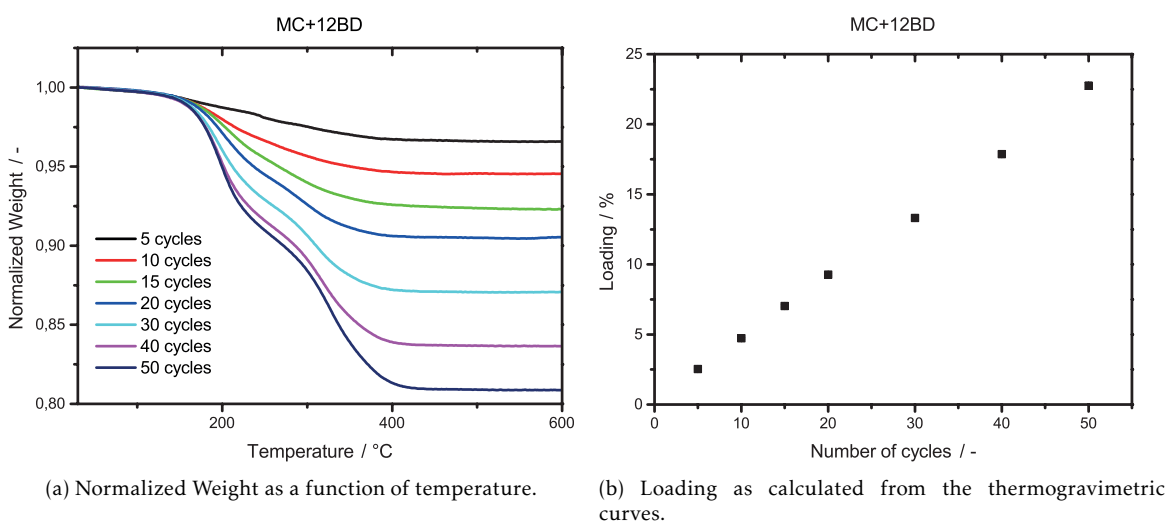


Figure 4.2: Thermogravimetric analysis in air with an heating rate of 5°C.min⁻¹. Figure (a) shows the normalized weight as a function of temperature for increasing number of MLD cycles on TiO₂ using MC and 12BD. These curves were consequently used to calculate the loading shown in Figure (b). The error bars, although they are too small to be visible, represent the uncertainty propagated in the TGA measurements.

From the obtained loadings, the thickness of the polyester film could be estimated using Equation 4.1 and it can be observed in Figure 4.3.

$$\delta = \frac{d_{core}}{2} \times \left(\sqrt[3]{\frac{f_{coating}}{100} \times \frac{\rho_{core}}{\rho_{coating}} + 1} - 1 \right) \quad (4.1)$$

where δ is the thickness, d_{core} is the diameter of bare TiO₂ as determined by BET measurements, $f_{coating}$ is the loading of the deposited film, ρ_{core} is the density of TiO₂ and $\rho_{coating}$ is the density of the polyester coating.

The GPC can be obtained by the slope of the linear fitting represented by the red line in Figure 4.3 and it is 0.057 ± 0.001 nm/cycle. The expected value of a monolayer thickness of the polyester formed by MC and 12BD is 1.023 nm. This was estimated assuming that the polyester monomer is completely linear and depending on the number of C–O and C–C bonds and their usual lengths, which are 0.141 and 0.153 nm respectively[93]. The theoretical monolayer thickness of all the polyesters deposited in this project are present in Table E.2. Therefore, the GPC obtained from TGA represents only 5.6% of the theoretical monolayer thickness of the polyester formed by MC and 12BD. Several studies in literature report GPC's lower than the length of one monomer and generally attribute this behaviour to either tilted growth of the polymer chains [2, 20, 21, 35, 36, 55] or double reactions with the surface [2, 20, 55]. *Adamczyk et al* [35] reported a GPC 4- to 25-fold lower than the expected value and attributed it to tilted growth of the polymer and to homobifunctional precursors, such as terephthaloyl chloride and p-phenylenediamine, which can react twice with the surface thus occupying active sites needed for the next layers.

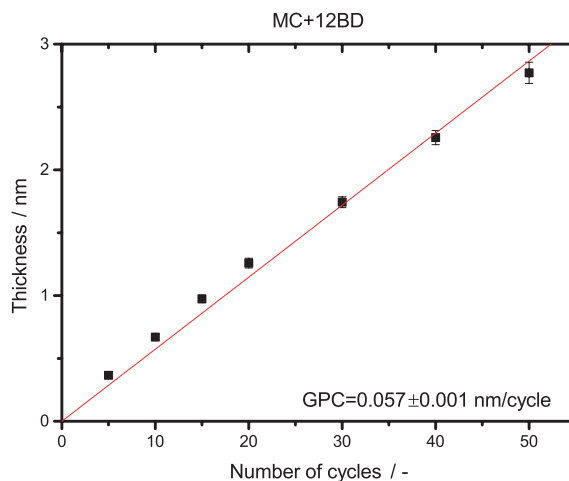


Figure 4.3: Thickness estimated from the obtained loadings by TGA. The error bars represent the uncertainty propagated in the TGA measurements, the uncoated TiO₂ diameter from BET and density of the coating, whereas the red line represents the linear fit of the data.

Furthermore, as shown by *Bergsman et al* [32], the GPC is fairly dependent on the flexibility of the precursors. It was stated that more flexible precursors tend to double-react with substrate surface. Since in the current experiment the precursors used have mainly aliphatic chains, this can also be the reason for the lower GPC as well. However, all these reasons would cause termination events and it would be expected that all active

sites would be occupied by increasing the number of cycles. *Bent et al*[18] proposed that new active sites are established inside the organic film during the cycling process either through absorption or adsorption of the precursors. This work showed that the initial growth rate on terminated surfaces was slower than on un-terminated surfaces but after 16 cycles it recovered and stayed constant. Hence, the absorption of precursors into the film seems a reasonable explanation for the lower but constant GPC obtained.

The sample with 50 cycles of MLD was also visualized under TEM. From Figure 4.4a, it is possible to observe a uniform and conformal carbonaceous coating, assumed to be polyester, around the particles. From Figure 4.4b, it is possible to observe that there is a difference of around 1.5 nm between the thicknesses estimated by TEM (1.3 nm) and TGA (2.8 nm) techniques. This difference can be attributed to two distinct reasons. The first is an inaccurate estimation of the density of the polyester coating, since a small variation in density yields a slightly distinct thickness. The second is the presence of excess precursor physisorbed on the substrate surface as the colour of the powder changed from white to orange, which is the colour of MC, with increasing cycles as shown in Figure 4.5. The excess precursor can induce a higher loading estimation from TGA which is translated into a higher thickness as well. The physisorbed species are, potentially, removed due to high vacuum produced during the TEM and thus are not observed.

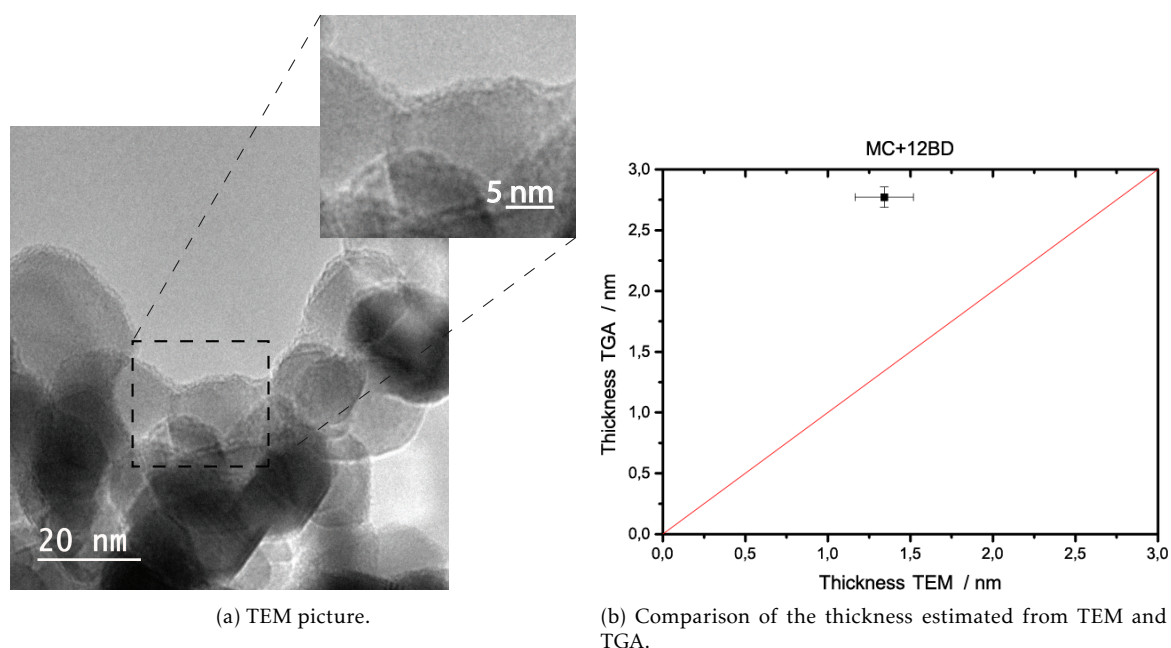


Figure 4.4: Figure (a) is a TEM picture of 50 MLD cycles coated TiO₂ using MC and 12BD. The darker areas are TiO₂ nanoparticles and it is possible to see that around most particles there is a lighter area which is the polyester coating. In (b), a comparison between the thicknesses estimated by TEM and TGA is given. The error bar in the TEM thickness represents the standard deviation obtained by measuring the thickness in three different parts of four different TEM pictures of the same sample. The red line represents the perfect agreement between the two methods.

This study, using MC as a reactant and 12BD as a co-reactant, revealed that it is, in fact, possible to deposit a polyester film on the surface of TiO₂ by MLD. The FTIR spectra showed the presence of both the ester C=O peak (1755 cm⁻¹) and the CH₃ stretches (2974,

2945 and 2884 cm^{-1}), proving the occurrence of the reaction between precursors. Both the integrated ester C=O peak and the film thickness ($\text{GPC}=0.057\pm 0.001$ nm) evolved linearly with increasing number of cycles, upholding one of the key characteristics of MLD. In addition, a carbonaceous film, most probably polyester, deposited on the 50 MLD cycles was visualized by TEM. However, the thickness estimated by TGA and TEM were not similar. Hence, experiments with higher number of cycles should be carried out to better understand the evolution of the MLD growth and to ensure that the visualized coating is indeed polyester.

As TiO_2 is widely used as a pigment, the bulk optical properties should not change with the addition of a coating [51, 61, 64]. It is certain that part of the optical properties have changed since there is a colour change as shown in Figure 4.5.



Figure 4.5: TiO_2 coated with 5, 20 and 50 MLD cycles using MC and 12BD.

Nonetheless, a photocatalytic test of uncoated TiO_2 and 5, 20 and 50 MLD cycles was performed as described in Section 3.4.1 to study the influence of the polyester coating formed by MC and 12BD in the photocatalytic activity of TiO_2 P25 nanoparticles. Figure 4.6 shows the absorption curves obtained from UV-Vis for each sample. It is possible to observe that there is a clear decrease in the rhB maximum absorbance peak at $\lambda_{max}=554$ nm over time. This decrease indicates that rhB is being degraded over time. The maximum absorbance peak suffers a shift to lower wavelengths with time. This shift is due to the de-ethylation of rhB and the fact that the fully de-ethylated rhB exhibits a major absorption band at $\lambda_{max}=506$ nm[117].

However, by comparing the intensity of the peak at λ_{max} at 0 minutes in Figure 4.6c and Figure 4.6d with Figure 4.6a and Figure 4.6b, it can be seen that in the 20 MLD cycles sample the absorbance is less than half and in the 50 MLD cycles this peak does not even appear. Furthermore, the solution with 50 MLD cycles coated TiO_2 is "orangish", as shown in Figure 4.7c, and remained with the same colour throughout the entire photocatalytic test. The low value of absorbance at 0 min suggests that part of the dye was adsorbed on the sample surface instead of being degraded. This is further supported by Figure 4.7 where it is possible to observe that the powder coated with 5 MLD cycles is white whereas the powder coated with 20 and 50 MLD cycles is pink during the whole photocatalytic

4.1. MOLECULAR LAYER DEPOSITION ON TiO₂

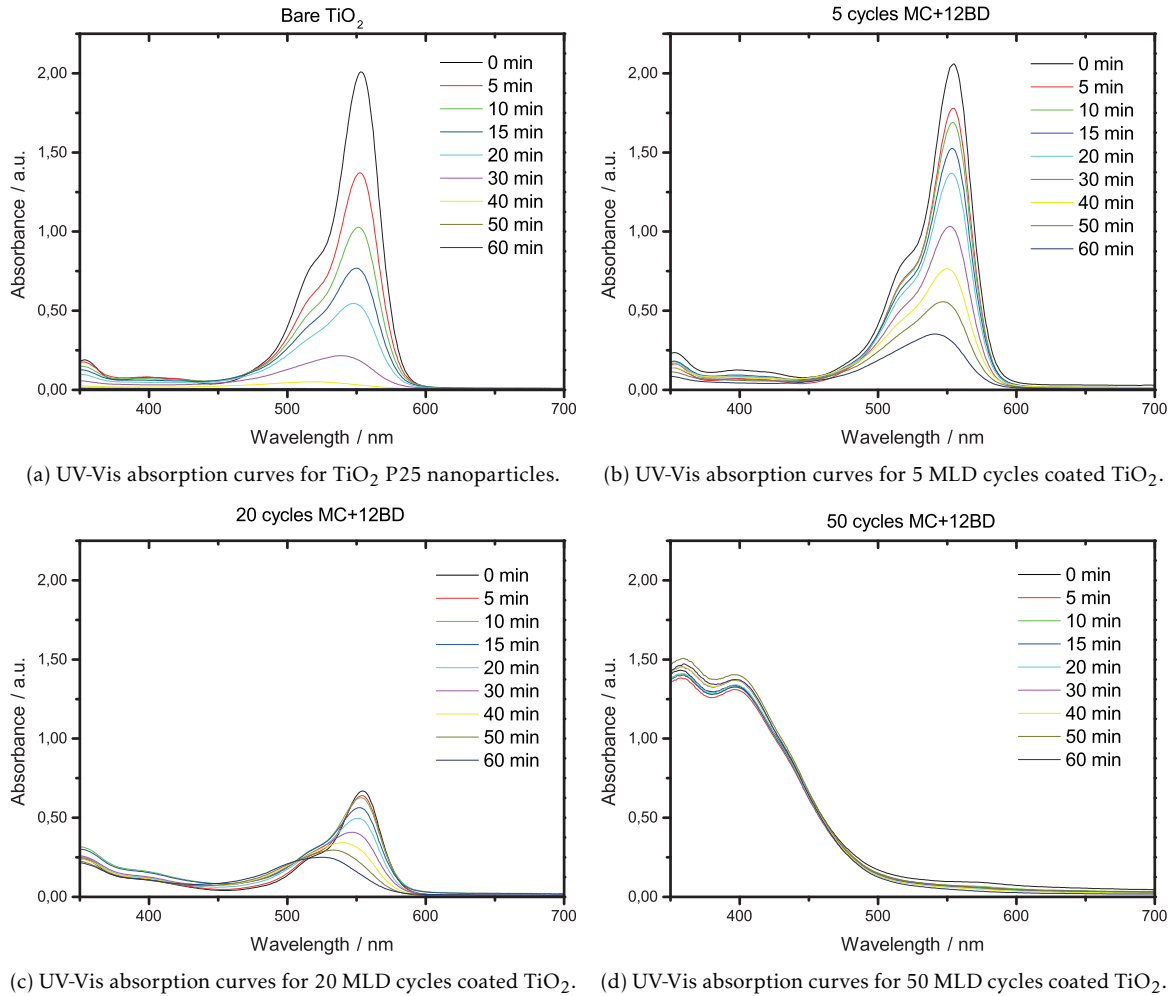
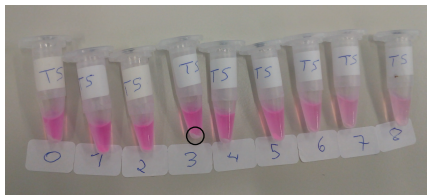
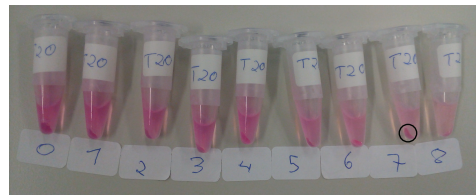


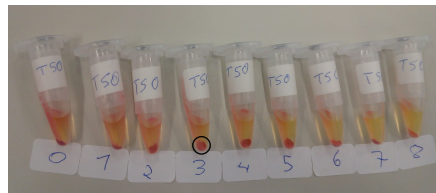
Figure 4.6: UV-Vis spectra of bare TiO₂ and MLD-coated TiO₂ with MC and 12BD that were subjected to the photocatalytic test over time. In (a), (b) and (c) it can be seen the presence of the rhB by the peak present at $\lambda=554$ nm. In (d), the rhB peak is not present but two peaks around 360 nm and 400 nm appear.



(a) 5 MLD-cycles on TiO₂ at the end of photocatalytic test.



(b) 20 MLD-cycles on TiO₂ at the end of photocatalytic test.

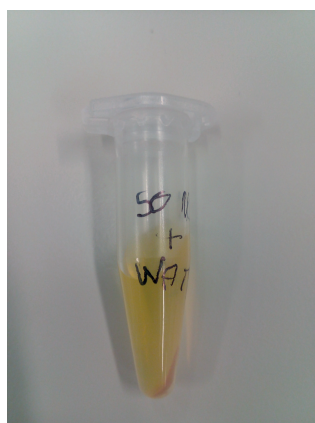


(c) 50 MLD-cycles on TiO₂ at the end of photocatalytic test.

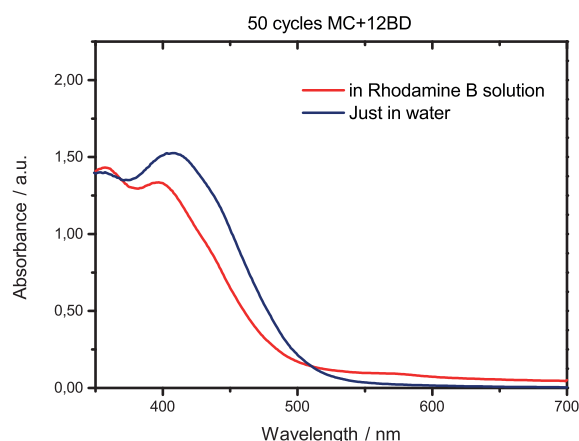
Figure 4.7: rhB solutions with MLD-coated TiO₂ after photocatalytic test and being centrifuged. In (a) and (b), it can be seen that the solution suffered discoloration over time. The numbers 0-9 correspond to 0, 5, 10, 15, 20, 30, 40, 50 and 60 minutes, respectively. In (c), the solution stayed with the same colour after the 60 minutes.

test. The colour of a solution with just water and TiO₂ coated with 50 MLD cycles using MC and 12BD (Figure 4.8a) is similar to the colour of the solution with 50 MLD coated TiO₂ and rhB (Figure 4.7c). Moreover, the UV-Vis absorption curve obtained for the solution with just water and TiO₂ coated with 50 MLD cycles using MC and 12BD is identical to the curve obtained for TiO₂ coated with 50 MLD cycles using MC and 12BD in a solution with rhB. The similarity of the obtained curves gives additional support to the initial assumption that the dye may get adsorbed onto the surface without being degraded.

This shows that suppressing the photocatalytic activity of TiO₂ P25 nanoparticles by depositing a polyester film by MLD using MC and 12BD is not feasible as the particles coated with higher number of cycles adsorb the dye instead of slowing down the degradation by TiO₂. The presence of malonyl chloride also induces colour change which modifies the optical properties of TiO₂.



(a) 50 MLD cycles coated TiO₂ P25 nanoparticles in water.



(b) UV-Vis of 50 MLD cycles coated TiO₂ in water and a rhB solution.

Figure 4.8: Figure (a) shows an aqueous solution with 50 MLD cycles coated TiO₂ using MC and 12BD. Figure (b) is a comparison between the UV-Vis of the aqueous solution with coated TiO₂ and the solution with rhB and coated TiO₂.

4.1.2 Molecular Layer Deposition using Diethyl Succinate

As described in Subsection 4.1.1, a polyester film was deposited on TiO₂ P25 nanoparticles by MLD using MC and 12BD but the photocatalytic activity of TiO₂ P25 nanoparticles was not suppressed as the coated particles adsorbed the dye. Therefore, it was decided to use DS as a new reactant to replace MC. It should be stated that for the experiments with DS, every characterization technique was done once for each sample due to the lack of powder collected during each sampling unless otherwise specified.

To study the evolution of the film growth by only using DS, an experiment up to 50 cycles was carried out. The operating conditions used for this experiment, experiment number 21, are shown in Table B.2. It is worth noting that in this case, one cycle comprises only two steps: (i) pulsing DS and (ii) purging. In addition, no saturation tests were performed prior to this trial and therefore the chosen pulse times and flow rates were

the same used with MC and 12BD. Therefore, the pulses times were 1/5 min and the flow rates were 1.5/1.5 l.min⁻¹. Samples at 5, 10, 15, 20, 30 and 40 cycles were collected during the experiment to understand the behaviour of this reactant on the surface of TiO₂.

The FTIR spectra obtained for each sample are shown in Figure 4.9. As it is possible to observe, in all spectra there is a peak around 1720 cm⁻¹, which is also attributed to a ester C=O peak as referred previously. It can be ascribed to the formation of carboxylic acid upon reaction of the diester with moisture present on the surface of TiO₂[112]. The intensity of this peak apparently ceases increasing after a few cycles, suggesting the saturation of the surface occurred between 15 and 20 MLD cycles instead of occurring in the first cycle. Furthermore, a more pronounced shoulder at 1740 cm⁻¹ starts to appear from 20 cycles onwards, indicating the presence of an ester[104]. However, both peaks should have appeared even with less cycles as DS is a diester and only one ester functional group is supposed to react with the surface. This fact suggests the occurrence of double-reactions with the substrate surface. Since the ester C=O peak is not well defined, the integrated area of the ester carbonyl peak was not calculated for any sample. Here, also a peak at 1540 cm⁻¹ appears which, as previously referred, can be attributed to the interaction of carbonyl groups with the surface of TiO₂ leading to the formation of the carboxylate ion (COO⁻)[116].

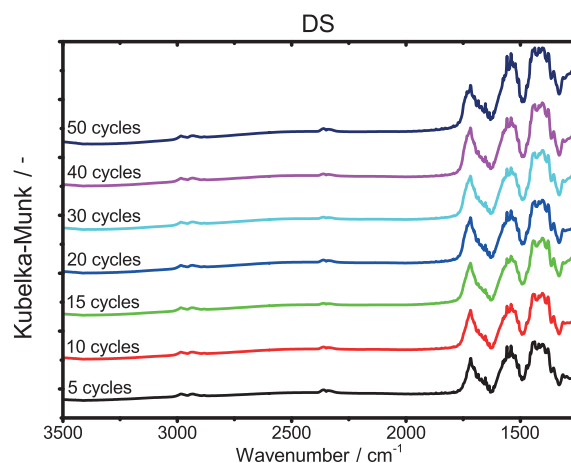
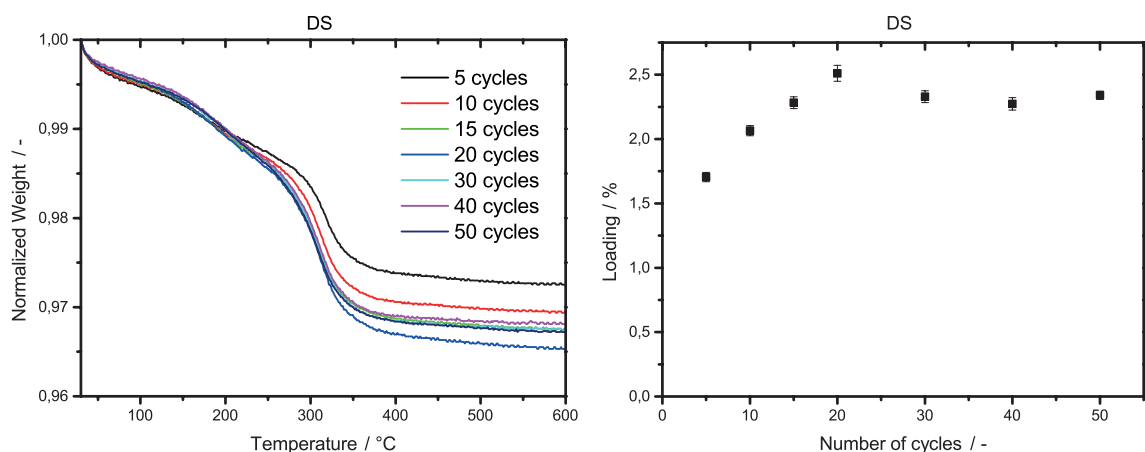


Figure 4.9: Subtracted FTIR spectra with increasing number of cycles of DS on TiO₂. These spectra were subtracted by the bare TiO₂ spectrum in Kubelka-Munk units. These spectra were measured once.

The TGA curves and estimated loadings for all samples are represented in Figure 4.10. Every sample was analysed under TGA twice. The loading estimated from the TGA curves increases until 20 cycles and then had a little decrease, remaining constant with increasing number of cycles. The higher loading value from 20 cycles can be due to an error in the TGA machine and thus it was not accounted for the calculation of the film thickness. By comparing both the FTIR spectra and TGA curves with increasing number of cycles, it is possible to observe that there is an identical saturation behaviour after 20 cycles. The late saturation behaviour may be caused by the fact that operating conditions



(a) Normalized weight as a function of the temperature. (b) Loading as calculated from the thermogravimetric curves.

Figure 4.10: Thermogravimetric analysis in air with an heating rate of $5^{\circ}\text{C}\cdot\text{min}^{-1}$. Figure (a) shows the normalized weight as a function of temperature for increasing number of cycles of solely pulsing DS on TiO_2 . These curves were consequently used to calculate the loading shown in Figure (b). The error bars, although they are too small to be visible, represent the uncertainty propagated in the TGA measurements.

in terms of flow rate and pulse times were not the ideal.

From the estimated loading, the DS film thickness could be obtained using Equation 4.1 and it is shown in Figure 4.11. The GPC was not calculated for this film as the estimated thickness has remained almost constant with increasing number of cycles.

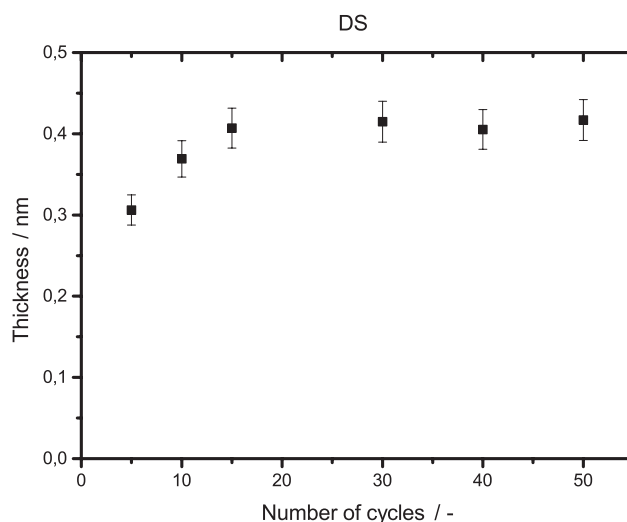
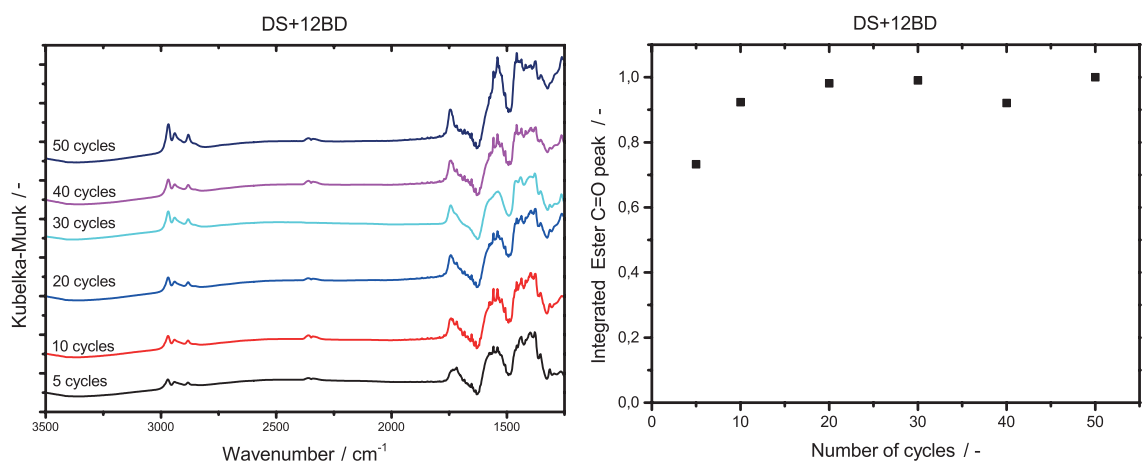


Figure 4.11: Thickness estimated from the obtained loadings from TGA for increasing number of cycles with solely pulsing DS on TiO_2 . The error bars represent the uncertainty propagated in the TGA measurements, the uncoated TiO_2 diameter from BET and density of the coating.

Afterwards, to study the MLD growth using DS and 12BD on TiO_2 P25 nanoparticles, an experiment of 50 MLD cycles was performed. Identical to previous experiments, samples were collected at 5, 10, 20, 30 and 40 cycles. The operating conditions used were the same as the conditions used with MC, therefore the pulse times were 1/5/1/5 min and the flow rates were 1.5/1.5/1.5/1.5 $\text{l}\cdot\text{min}^{-1}$ as shown in Table B.2.

The obtained FTIR spectra and respective integrated ester C=O peak are shown in

Figure 4.12. The ester C=O peak is identifiable in every spectrum at 1744 cm⁻¹. For the 5 MLD cycles on TiO₂ using DS and 12BD, a peak appears at 1720 cm⁻¹, analogous to what occurs when solely pulsing DS. This can be attributed to the formation of carboxylic acid by the reaction of DS and moisture present on the surface. However, in this case, there is the presence of three peaks in the range 3000-2880 cm⁻¹. As explained before, these peaks arise due to the symmetric CH₃ stretch split (2940 and 2881 cm⁻¹) and the asymmetric CH₃ stretch (2967 cm⁻¹). It is also possible to observe a broad peak in the range 1370-1475 cm⁻¹ that is ascribed to the C-H bend of CH₃[104]. As mentioned in Subsection 4.1.1, the simultaneous appearance of the ester C=O peak and the symmetric and asymmetric CH₃ stretches are an excellent indication that at least part of the precursors have reacted to form a polyester.



(a) Subtracted FTIR spectra with increasing number of cycles. (b) Normalized ester peak area from 1808.930-1685.507 cm⁻¹.

Figure 4.12: FTIR spectra obtained for different number of MLD cycles using DS and 12BD. Figure (a) shows the spectra after being subtracted by the bare TiO₂ spectrum in Kubelka-Munk units. Figure (b) shows the peak area under the ester peak from 1808.930 cm⁻¹ to 1685.507 cm⁻¹ for all samples in (a). They were normalized with respect to highest value. These spectra were measured once.

Typically, as previously referred, transesterification reactions require the presence of a base or acid catalyst [93, 94]. *Martra*[118] reported the existence of Lewis acid-base pairs on the surface of TiO₂ that can catalyze reactions between adsorbed species. Hence, these Lewis acid-base pairs may have catalysed the reaction between DS and 12BD. This proposition is further supported by *Kim et al*[119]. *Kim et al* reported the gas-phase transesterification of dimethylcarbonate and phenol over supported TiO₂ in a fixed bed reactor. The supported TiO₂ catalyst achieved a conversion of over 35% and a selectivity of almost 90% with 10 wt% Ti. The high selectivities were maintained above 10 wt% indicating that both monolayer and bulk TiO₂ serve as active sites.

Nevertheless, when comparing the FTIR spectra in Figure 4.12a, it can be seen that the ester peak at 1740 cm⁻¹ stops increasing after 20 cycles, as shown by the integrated ester C=O peak in Figure 4.12b. This behaviour implies that initially, the precursors can reach the surface and consequently react to yield an ester. However, after a few cycles, the surface of TiO₂ becomes shielded, i.e. all catalytic active sites are occupied, and

hence, it cannot act as a catalyst anymore, causing the growth cease. Furthermore, double reactions and the tilted growth of the polymer chain may also occur.

The TGA curves with increasing number cycles for MLD on TiO_2 using DS and 12BD are shown in Figure 4.13a. From 30°C to 120°C , all samples present similar weight loss except the 5 MLD cycles sample. This can be attributed to an increased amount of moisture, although it is highly unlikely as the FTIR spectra does not show any peak related to $-\text{OH}$ groups ($3400\text{-}3250\text{ cm}^{-1}$) or water (1640 cm^{-1}). Between 120°C and 500°C , all samples have an identical weight loss (Figure 4.13b), despite some negligible fluctuation attributed to the TGA machine.

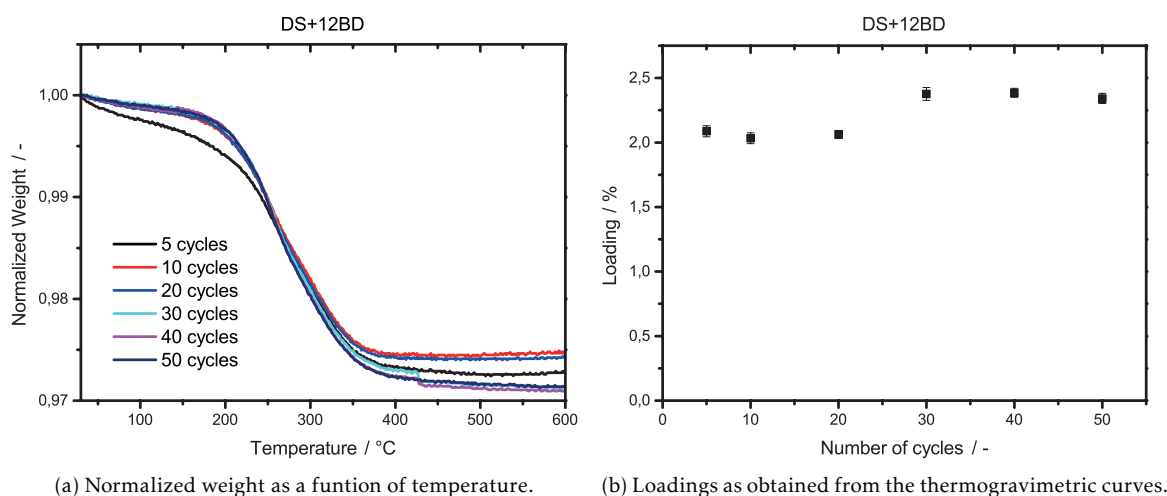


Figure 4.13: Thermogravimetric analysis in air with an heating rate of $5^\circ\text{C}\cdot\text{min}^{-1}$. Figure (a) shows the normalized weight as a function of temperature for increasing number of MLD cycles on TiO_2 using DS and 12BD. These curves were consequently used to calculate the loading shown in Figure (b). The error bars, although they are too small to be visible, represent the uncertainty propagated in the TGA measurements.

The thickness for each sample was then calculated by Equation 4.1 and it is shown in Figure 4.14. Since the growth apparently reached a saturation point, the GPC was not calculated for this experiment either.

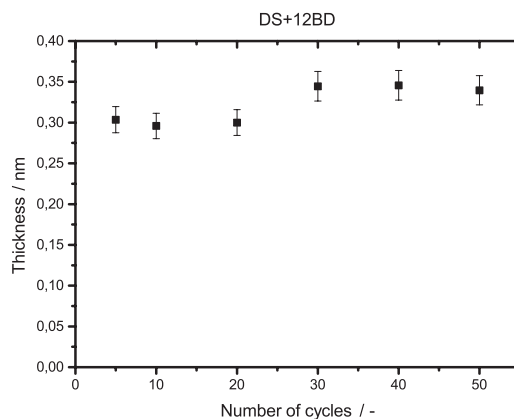


Figure 4.14: Thickness estimated from the obtained loadings from TGA for increasing number of MLD cycles with DS and 12BD on TiO_2 . The error bars represent the uncertainty propagated in the TGA measurements, the uncoated TiO_2 diameter from BET and density of the coating.

Subsequently, the sample with 50 MLD cycles of DS and 12BD was also visualized under TEM as depicted in Figure 4.15. As it can be seen, it is not possible to observe any organic film on TiO₂ nanoparticles. This can be ascribed to the fact that the film is too thin, as the expected thickness from TGA is lower than the maximum resolution of the used TEM. Therefore, high resolution TEM should be performed[120] to verify the existence of a polyester coating.

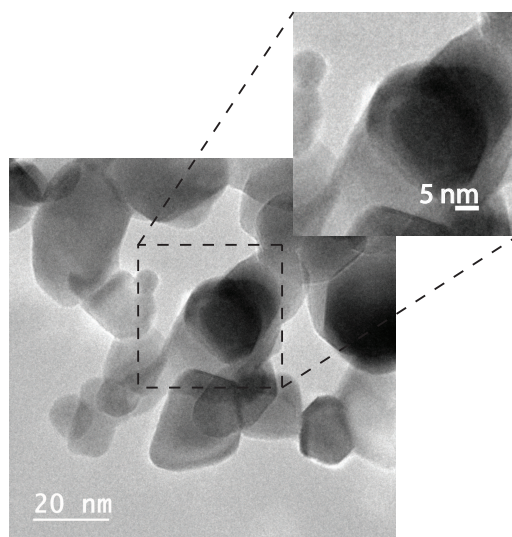
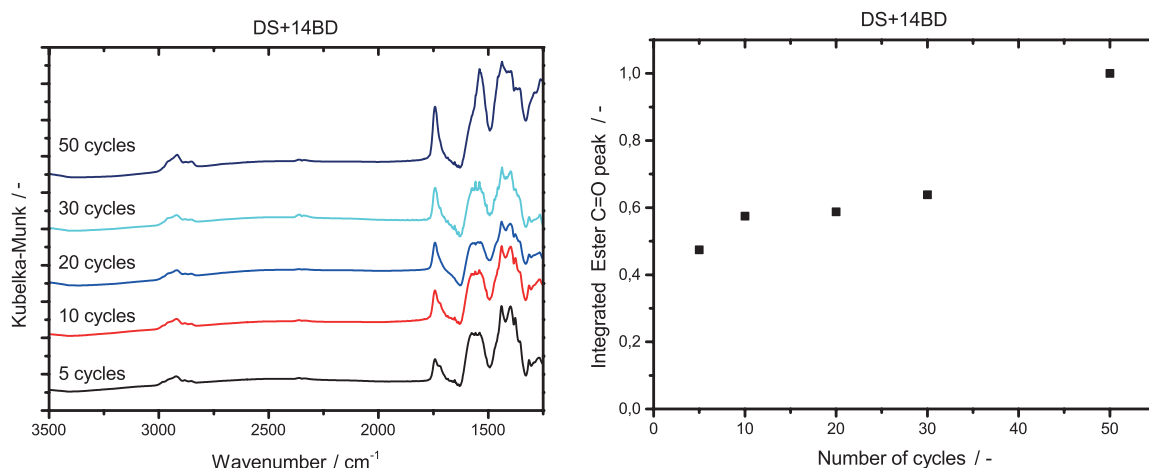


Figure 4.15: TEM picture of MLD-coated TiO₂ P25 nanoparticles after 50 cycles using DS and 12BD. The darker areas are TiO₂ nanoparticles. It was not possible to visualize any polyester film deposited on the particles.

Since the experiments using only DS and complete MLD using DS and 12BD had similar results in terms of growth, it was decided to test another diol. A list of possible co-reactants for MLD of polyester films is suggested by *J. Ruud van Ommen*[92]. This list is divided in two categories: (i) start-end, meaning the OH functional groups are at both ends of the molecule and (ii) start-next, meaning the OH functional groups are next to each other. As 12BD is a start-next diol, it was determined to use its start-end counterpart, 14BD. An experiment up to 50 cycles was performed. The operating conditions, identified as experiment number 23, are described in Table B.2. The pulse times and flow rates were maintained the same as the previous experiments with DS. During the experiment, samples were collected at 5, 10, 20, 30 cycles.

Figure 4.16a shows the subtracted FTIR spectra obtained for each sample. The characteristic ester C=O around 1741 cm⁻¹ appears in every sample's spectra confirming the presence of polyester. In the 5 cycles spectrum, there is also the presence of a shoulder at 1724 cm⁻¹ which can be attributed to the formation of carboxylic acid from the reaction between DS and moisture present on the surface of TiO₂. Despite the reactor temperature of 120°C, some moisture could still be present before 5 cycles were complete, explaining the existence of a more pronounced carboxylic acid peak. However, since this shoulder disappears with increasing number of cycles, possibly the moisture was vaporized over time during the subsequent purge pulses. Three peaks at 2916, 2880, 2850 cm⁻¹ and a



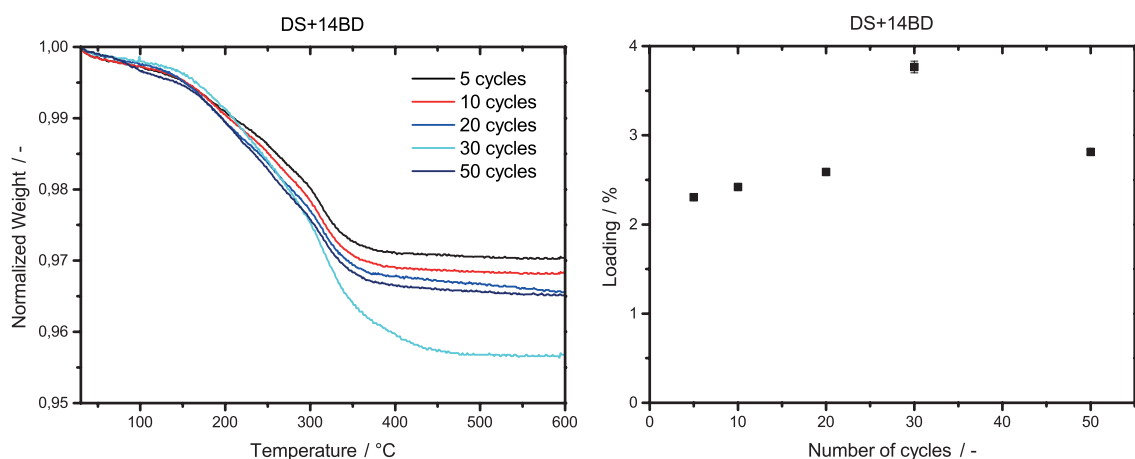
(a) Subtracted FTIR spectra with increasing number of cycles. (b) Normalized ester peak area from 1808.930-1685.507 cm⁻¹.

Figure 4.16: FTIR spectra obtained for different number of MLD cycles on TiO₂ using DS and 14BD. Figure (a) shows the spectra after being subtracted by the bare TiO₂ spectrum in Kubelka-Munk units. Figure (b) shows the peak area under the ester peak from 1808.930 cm⁻¹ to 1685.507 cm⁻¹ for all samples in (a). They were normalized with respect to highest value. These spectra were measured once.

short shoulder at 2980 cm⁻¹ arise with increasing number of cycles. The peaks at 2916 and 2850 are typically assigned to the symmetric and antisymmetric CH₂ groups, respectively[115]. The appearance of these two peaks was expected as there is no methyl (CH₃) groups in a polyester formed by DS and 14BD. In this instance, there is also a broad peak in the range of 1370-1475 cm⁻¹ that can be attributed to the C-H bend of CH₂, instead of CH₃[104]. Both the appearance of the ester C=O peak at 1741 cm⁻¹ and the methylene group stretches indicate that the reaction between the two precursors occurred to form a polyester. The 2880 cm⁻¹ peak and 2980 cm⁻¹ shoulder, as described earlier in Subsection 4.1.1, are attributed to the symmetric CH₃ stretch split due to Fermi resonance and can be assigned to some unreacted DS present in the reactor. The integrated ester C=O peak under the range 1809-1685 cm⁻¹ increased slightly until 30 MLD cycles whereas between 30 and 50 MLD cycles increased about 36% as shown in Figure 4.16b.

The TGA curves and loadings obtained for MLD coated TiO₂ using DS and 14BD are present in Figure 4.17. In this experiment, each sample was analysed twice in TGA. The TGA curves depicted in Figure 4.17a show little difference up to 120°C, meaning that their water content is fairly similar. Between 120°C and 500°C, it can be seen that the loading increases with increasing number of cycles until 30 cycles and then decreases as shown in Figure 4.17b. The temperature of the 14BD bubbler was not well controlled from cycle 20 to cycle 30, reaching temperatures higher than the temperature of the reactor several times. This temperature difference may have induced the condensation of precursor inside the reactor causing the weight loss to increase. Thus, the 50 MLD cycles should have higher loading as well which is not verified. The last 20 cycles were done the following day, as this experiment took over 2 days. During this day, despite the inefficient control of the temperature of diol bubbler, the reactor temperature raised

4.1. MOLECULAR LAYER DEPOSITION ON TiO₂



(a) Normalized weight as a function of temperature.

(b) Loadings as obtained from the thermogravimetric curves.

Figure 4.17: Thermogravimetric analysis in air with an heating rate of $5^{\circ}\text{C}\cdot\text{min}^{-1}$. Figure (a) shows the normalized weight as a function of temperature for increasing number of MLD cycles on TiO₂ using DS and 14BD. These curves were consequently used to calculate the loading shown in Figure (b). The error bars, although they are too small to be visible, represent the uncertainty propagated in the TGA measurements.

from 120°C to 140°C with the IR lamp switched off. This increased reactor temperature could have managed to vaporize the excess precursor and therefore remove it from the reactor.

Subsequently, the thickness of the film from the estimated loadings was calculated by Equation 4.1 and it is shown in Figure 4.18. The evolution of the thickness of the polyester film is analogous to the previous experiments with DS as reactant. In the first 20 cycles there is a negligible increase and afterwards the growth practically stops.

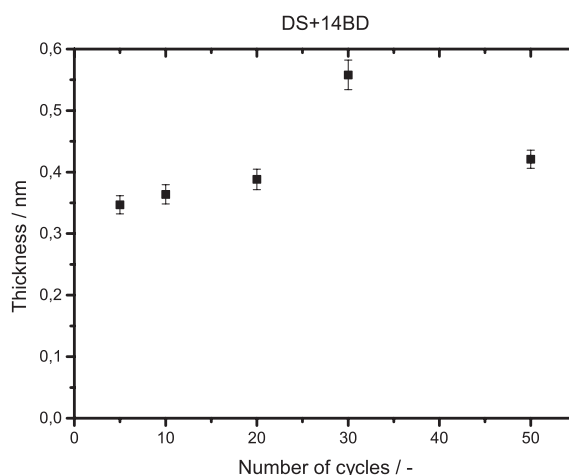


Figure 4.18: Thickness estimated from the obtained loadings from TGA for increasing number of MLD cycles with DS and 14BD on TiO₂. The error bars represent the uncertainty propagated in the TGA measurements, the uncoated TiO₂ diameter from BET and density of the coating.

The sample with 50 MLD cycles on TiO₂ using DS and 14BD was also visualized by TEM. In Figure 4.19a, it is possible to observe a conformal thin coating on most particles. However, several pictures were taken in different sites of the powder and as it can be seen in Figure 4.19b, a significant amount of particles were not coated during the MLD

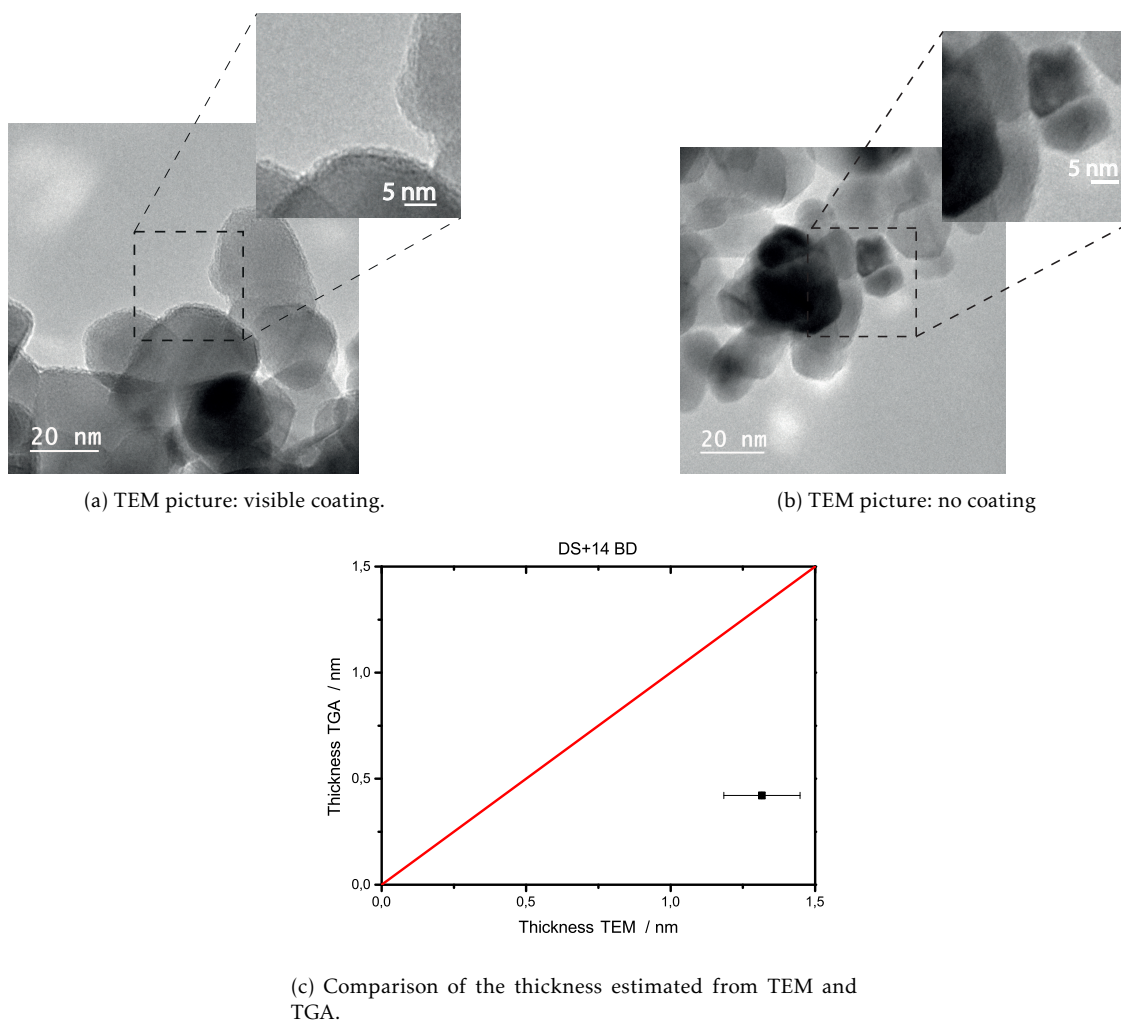


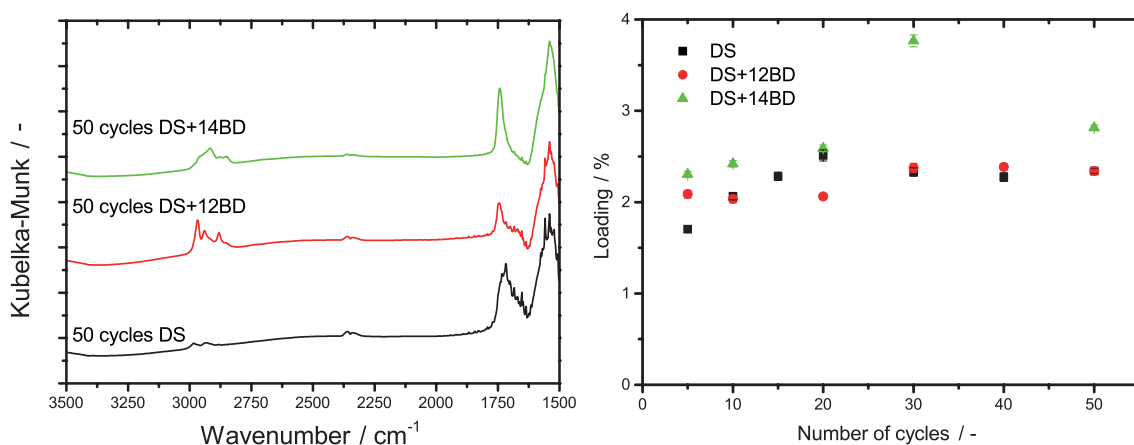
Figure 4.19: Figure (a) and (b) are TEM pictures of MLD-coated TiO_2 P25 nanoparticles after 50 cycles using DS and 14BD. The darker areas are TiO_2 nanoparticles. Around most particles in (a) there is a lighter area which is the polyester coating. In (b) no coating is observable. In (c), a comparison between the thicknesses estimated by TEM in Figure (a) and TGA is given. The error bar in the TEM thickness represents the standard deviation obtained by measuring the thickness in three different parts of four different TEM pictures of the same sample. The red line represents the perfect agreement between the two methods.

process. This shows a weakness of the process using DS and 14BD as it cannot provide a conformal thin film around every particle. This weakness may arise from the absence of a proper catalyst. Although the TiO_2 nanoparticles may catalyze the transesterification reaction as stated previously, the film growth is not conformal and stops after some time due to the occupation of the catalytic active sites.

Consequently, a comparison between the thickness estimated from TEM and the thickness estimated from TGA was done as shown in Figure 4.19c. It can be seen that there is a difference of 0.9 nm between both thicknesses ($\delta_{TEM}=1.32$ nm and $\delta_{TGA}=0.42$) and, as stated before in Subsection 4.1.1, this difference can arise from an inaccurate estimation of the density of the polyester coating or the presence of carbonaceous impurities. Moreover, the thickness measured under TEM for this polyester film using DS and 14BD is identical to the measured thickness using MC and 12BD whereas the thicknesses measured by

TGA are quite different.

Figure 4.20 shows a comparison of the FTIR spectra and estimated loading obtained for every 50 cycles sample done with DS. The ester peak of the 50 MLD cycles using is clearly better defined, meaning that there is only the presence of this peak without any visible shoulder, than in 50 MLD cycles using DS and 12BD. Besides, the 50 MLD cycles using DS and 14BD presents a higher loading than the combination of DS and 12BD. Hence, the samples of MLD coated TiO₂ using DS and 14BD were chosen to study the influence of a polyester film on the photocatalytic activity of TiO₂ P25 nanoparticles.



(a) Subtracted FTIR spectra for every 50 cycles sample using DS. (b) Estimated loading from TGA every 50 cycles sample using DS.

Figure 4.20: Comparison between the 50 cycles on TiO₂ using solely DS, 50 MLD cycles on TiO₂ using DS and 12BD and 50 MLD cycles on TiO₂ using DS and 14BD. Figure (a) shows FTIR spectra after being subtracted by the bare TiO₂ spectrum in Kubelka-Munk units. Figure (b) shows the evolution of the loading with increasing number of cycles. The error bars represent the uncertainty propagated in the TGA measurements.

From the study using DS as a reactant, it can be concluded that there is indeed deposition of polyester as the FTIR spectra from both the MLD using 12BD and using 14BD showed a C=O peak around 1740 cm⁻¹ which is generally related to an ester carbonyl bond[104]. However, the weight losses estimated from TGA do not present significant difference between solely pulsing DS and doing a fully MLD process using DS and 12BD. Moreover, it was not possible to visualize any polyester film deposited onto TiO₂ coated with 50 MLD cycles using DS and 12BD by TEM. This proved that although there was polyester, the film was too thin or not uniformly present to be visualized. The experiment using DS and 14BD showed a clear ester C=O peak at 1740 cm⁻¹, slightly higher weight losses from TGA and a carbonaceous coating was visualized by TEM. Nevertheless, for all experiments the growth after 20/30 cycles ceased. Therefore, experiments with higher number of cycles are required to gain insights into the morphology of the MLD films deposited with these combinations and the evolution of the ester C=O peak.

As described in Subsection 4.1.1, the bulk optical properties of TiO₂ P25 nanoparticles should not be affected by the deposited film, thus visually the colour should stay white. From Figure 4.21, it can be seen that the colour of the powder almost did not change from

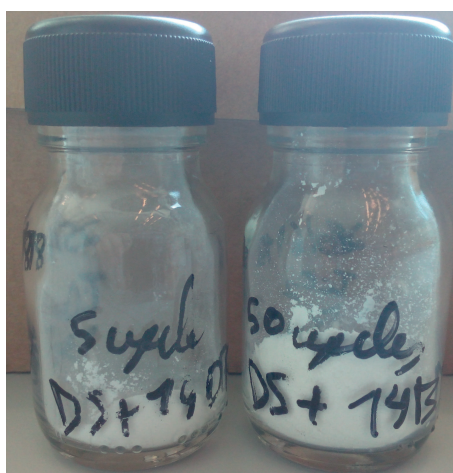


Figure 4.21: TiO₂ P25 nanoparticles coated with 5 and 50 MLD cycles using DS and 14BD

5 MLD cycles to 50 MLD cycles. Only two samples are shown since there was no powder left from the other samples after the characterization techniques.

To test the influence of the polyester coating formed by diethyl succinate and 14BD in the photocatalytic activity of TiO₂ P25 nanoparticles, photocatalytic tests of the 5 and the 50 MLD cycles, as described in subsection 3.4.1, were conducted.

From Figure 4.22, it can be seen that the characteristic rhB peak at $\lambda=554$ nm at 0 min is present in both the 5 MLD cycles and the 50 MLD cycles practically with the same intensity as the peak found in the uncoated TiO₂ P25 nanoparticles (see Figure 4.6a). This means that, unlike with the polyester deposited by MLD using MC and 12BD, this polyester coating does not cause the adsorption of the dye onto the surface of TiO₂.

Subsequently, the kinetic constants for the degradation of rhB using uncoated TiO₂ P25 nanoparticles and using 5 and 50 MLD cycles using DS and 14BD on TiO₂ P25

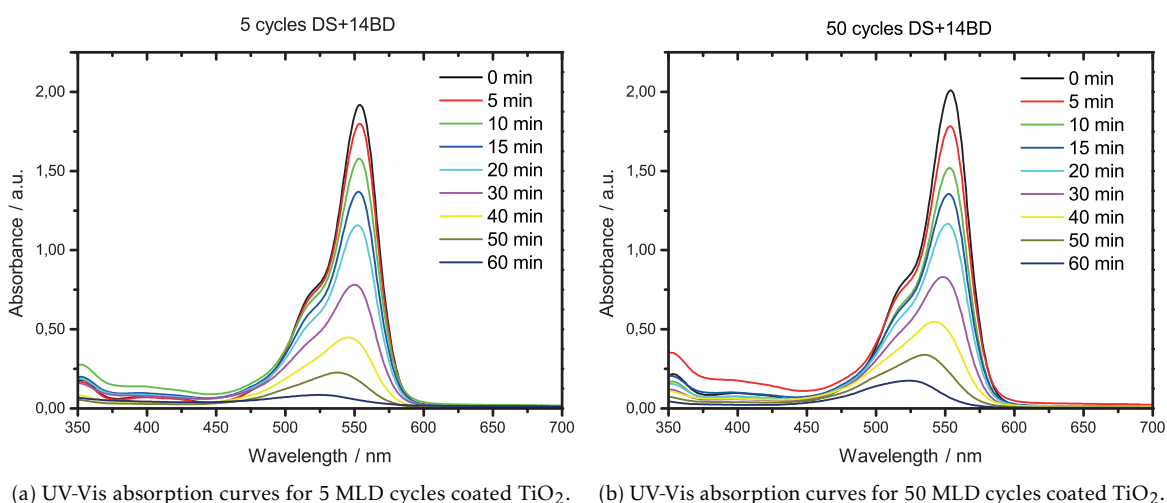


Figure 4.22: UV-Vis spectra of MLD-coated TiO₂ with DS and 14BD that were subjected to the photocatalytic test over time. In (a) and (b), it can be seen the presence of the rhB by the peak at $\lambda=554$ nm.

nanoparticles shown in Figure 4.23 were calculated by the slope of Equation 4.2 as described in section G.1.

$$\ln\left(\frac{A_0}{A_t}\right) = k \times t \quad (4.2)$$

where A_0 is the absorbance at 0 minutes and A_t is the absorbance at time t , both at $\lambda=554$ nm.

From Figure 4.23b, it can be seen that the kinetic constant was reduced about 52% from uncoated TiO_2 to 5 MLD cycles. The kinetic constants of the 5 and the 50 MLD cycles are identical ($k_{5 \text{ cycles}} = 47.77 \times 10^{-3} \text{ min}^{-1}$ and $k_{50 \text{ cycles}} = 45.39 \times 10^{-3} \text{ min}^{-1}$). As these two samples exhibit similar film thickness estimated by TGA, it was expected that their ability to suppress the photocatalytic activity of TiO_2 P25 nanoparticles was equally identical. Therefore, a polyester film deposited by MLD using DS and 14BD can, in fact, partially suppress the photocatalytic activity of TiO_2 P25 nanoparticles. However, further work is necessary to gain more insight on how to achieve thicker polyester films by MLD using DS and 14BD and their influence in the photocatalytic activity of TiO_2 P25 nanoparticles. It is important to state again that typically a transesterification reaction takes place in the presence of an acid or base catalyst[92, 93] which was not the case of this study.

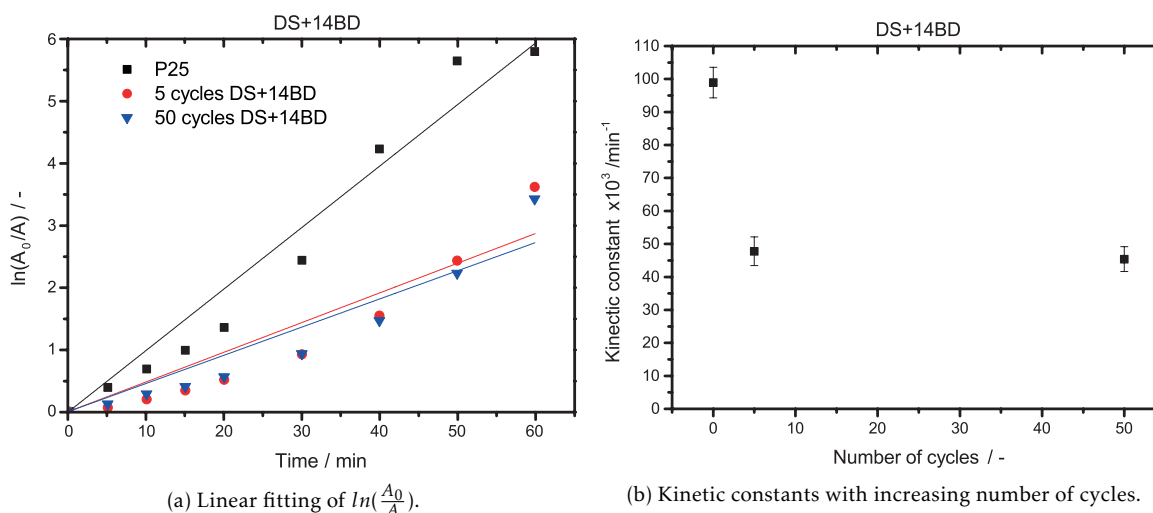


Figure 4.23: Figure (a) shows the evolution of $\ln\left(\frac{A_0}{A}\right)$ over time for uncoated TiO_2 P25 nanoparticles, 5 and 50 MLD cycles using DS and 14BD on TiO_2 P25 nanoparticles. Figure (b) shows the kinetic constants calculated from (a). The kinetic constant for uncoated TiO_2 P25 nanoparticles is represented as 0 cycles. The error bars represents the standard error as calculated by OriginPro 9 software.

4.2 Molecular Layer Deposition on Proteins

4.2.1 Molecular Layer Deposition using Malonyl Chloride

In this section, the experiments with 10 MLD cycles on proteins using MC and 12BD while increasing the flow rate from 1.5 till $4 \text{ l}\cdot\text{min}^{-1}$, 30 MLD cycles on proteins using MC and 12BD while using 4-port bottom windbox where the 4th port was used to continuously

send nitrogen gas to be able to fluidize the particles, 10 cycles of solely pulsing one of the precursors and heating up protein at 50°C over 2 hours will be discussed. A summary of the conditions used for these experiments (experiment numbers 12, 18-21), is shown in Table B.2. It should be noted that no saturation tests were performed during this project and thus the chosen operating conditions are similar to the conditions used for MLD on TiO₂ P25 nanoparticles using MC and 12BD. All experiments were executed with a reactor and bottom windbox temperature of 50°C.

To understand the MLD growth behaviour on proteins using MC and 12BD, two experiments up to 10 and 30 cycles were performed. The 10 MLD cycles on proteins using MC and 12BD while increasing the flow rate from 1.5 till 4 l.min⁻¹ was performed first.

The subtracted FTIR spectrum is depicted in Figure 4.24a. The subtracted FTIR spectrum of 10 MLD cycles on protein shows a peak at 1750 cm⁻¹, which can be assumed as the ester peak, indicating that a polyester film was deposited onto the protein. The integrated area under the ester peak was not calculated as in this experiment no powder was collected at lower number of cycles. During the experiment, the fluidization of the protein particles was lost everytime a precursor was being pulsed and then returning back while being purged. However, the fluidization got worse with increasing number of cycles and thus the flow rates were increased to counter this effect. In the end of this experiment, the protein particles were quite agglomerated as it can be seen in Figure 4.24b. The presence of such big agglomerates inside the reactor is probably the cause of the loss of fluidization.

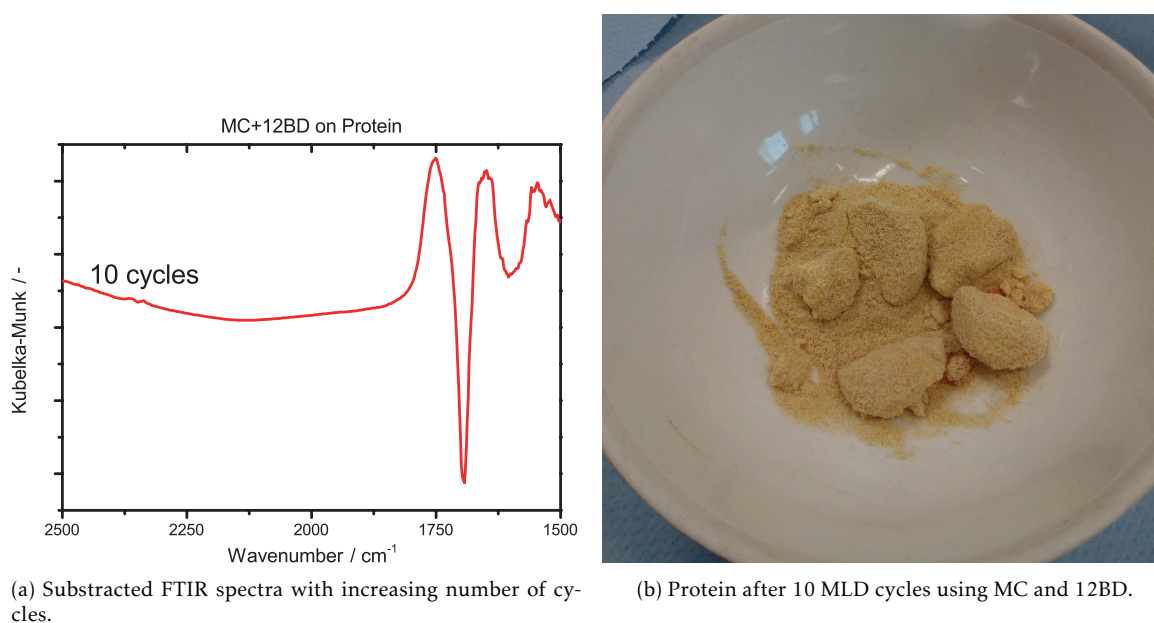


Figure 4.24: Figure (a) shows the FTIR spectra obtained for different number of cycles of MLD using MC and 12BD while increasing the flow rate on protein after being subtracted by the bare protein spectrum in Kubelka-Munk units. Figure (a) shows the spectra Figure (b) shows the protein after being collected. The powder was fairly agglomerated however they were easily grinded afterwards.

Consequently, for the 30 MLD cycles experiment, it was decided to use a 4-port bottom windbox in order to enhance the fluidization of the particles without sending excess precursor. Therefore, the flow rates used were 1.5 (5 N₂)/5/1.5 (5 N₂)/5 l.min⁻¹. Identical to what was done with MLD on TiO₂, samples were collected during the experiment at 10, 15 and 20 cycles. It was observed that the pressure drop evolved in a similar manner as the previous experiment, however, there were no agglomerates formed at the end.

The FTIR spectra obtained for each sample are shown in Figure 4.25a. It is possible to see that with increasing number of cycles a peak at 1760 cm⁻¹ emerges. Even though this is slightly out of the usual range for an ester C=O peak, it can still be assigned to an ester. The higher carbonyl peak can result from the resonance competition for the lone-pair electrons of the ether oxygen (C–O) by the carbonyl group and the new conjugating group, i.e. the protein[104]. Furthermore, a peak begins to arise after 20 cycles at 1830 cm⁻¹. This peak is typically related to acid halides (X-C=O, X represents an halogen atom) and thus it implies the existence of unreacted MC. Subsequently, the integrated ester C=O peak was calculated in the range 1809 to 1724 cm⁻¹ as shown in Figure 4.25b. This range was chosen since with the range used for TiO₂, the baseline would be too skewed and a proper conclusion could not be drawn from it. The integrated area under the ester peak around 1760 cm⁻¹ seems to be quite linear with increasing number of cycles.

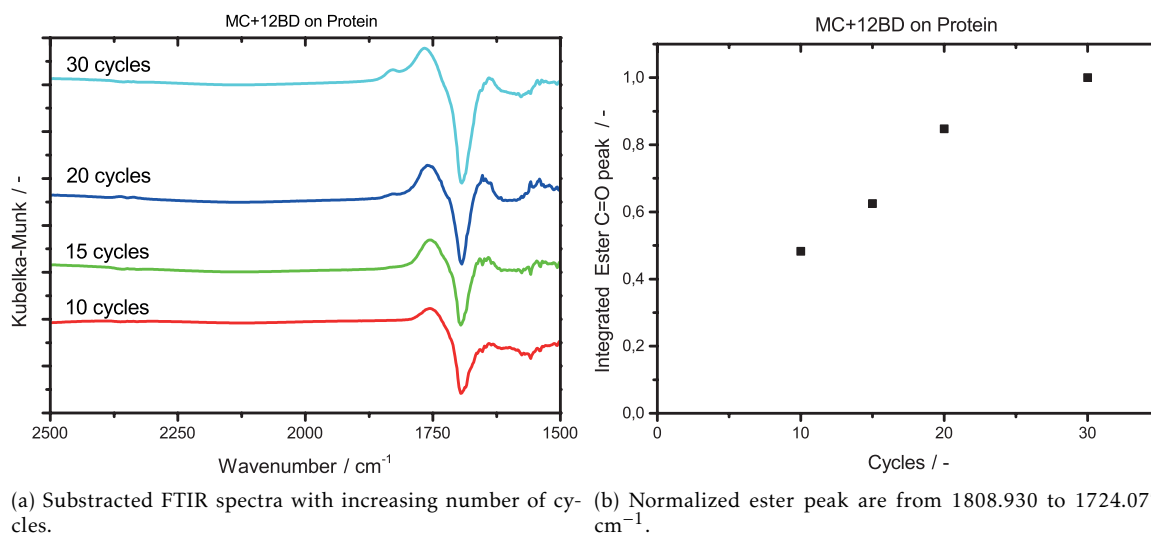


Figure 4.25: FTIR spectra obtained for different number of cycles of MLD using MC and 12BD on protein and using a 4-port bottom windbox. Figure (a) shows the spectra after being subtracted by the bare protein spectrum in Kubelka-Munk units. Figure (b) shows the peak area under the ester peak from 1808.930 cm⁻¹ to 1724.077 cm⁻¹ for all samples in (a). All spectra were measured once.

Proteins can undergo denaturation for several different reasons such as: presence of chemical denaturants, e.g. guanidinium chloride, temperature, pressure and pH[121–125]. As the MLD process was executed at atmospheric pressure, the protein should not be affected by it. Therefore, to study the influence of each precursor and temperature on proteins, two experiments till 10 cycles of solely pulsing one the precursors and one

experiment of heating up the protein at 50°C for 2 hours were executed. The operating conditions for the 10 cycles pulsing only one precursor were similar to the conditions used in the first 10 MLD cycles on protein and they are present in Table B.2. The flow rate used for each pulse was 4 l.min⁻¹. The experiment of heating up the protein at 50°C was performed by merely switching on the IR lamp, the lines' and bottom windbox's heating tapes without any gas flow.

Figure 4.26 compares the FTIR spectra obtained for both the 10 cycles of pulsing just one precursor, the 10 MLD cycles using MC and 12BD with the 4th-port bottom windbox and protein heated for 2 hours. The FTIR spectrum of the heated sample is practically an horizontal line. Hence, the heating does not have a significant effect on the protein as there is no particular difference between bare protein and the protein after being heated to 50°C. The FTIR spectrum of 10 cycles of 12BD shows a peak at 1700 cm⁻¹ but it is due to the used subtraction factor as this peak also appears in the spectrum of bare protein as shown in Figure C.3. By comparing both spectra from sending only MC and from the complete MLD process, it can be seen that in both a peak around 1760 cm⁻¹ appears. Therefore this peak cannot be completely assigned to the formation of an ester. Moreover, in the spectrum of just MC, similar to what is shown in the 30 MLD cycles spectrum, a shoulder at 1830 cm⁻¹ arises, which is attributed to an acid halide[104]. Thus, this peak can surely be assigned to the presence of unreacted MC in both FTIR spectra.

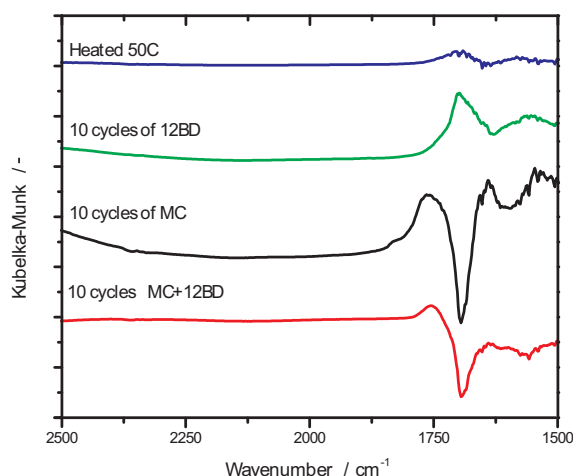
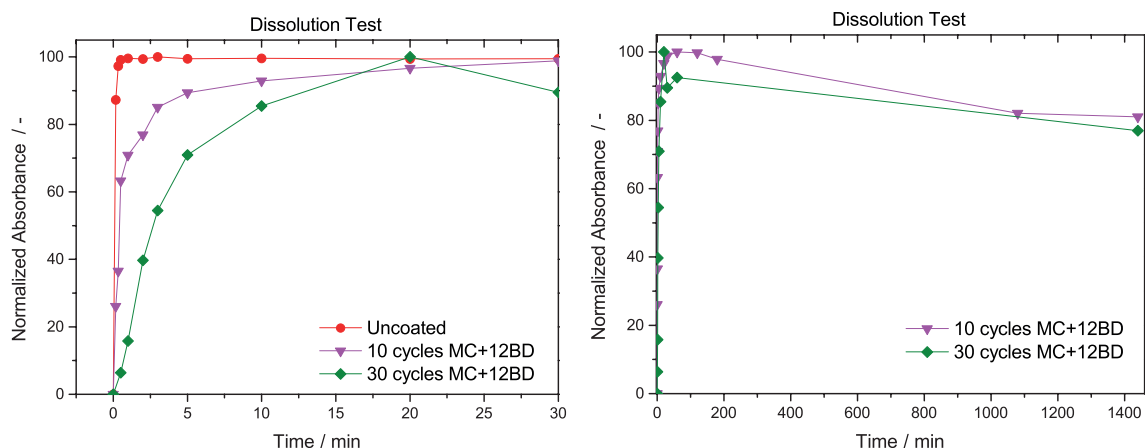


Figure 4.26: Subtracted FTIR spectra obtained for 10 cycles of pulsing only one precursor on protein, heating the protein at 50°C and 10 complete MLD cycles using MC and 12BD. This spectra was subtracted by the bare protein spectrum in Kubelka-Munk units.

To study the influence of different number of MLD cycles, precursors and heating up on the dissolution of the used protein, dissolutions tests of bare protein, 10 MLD cycles with higher flow rate (1.5 till 4 l.min⁻¹), 30 MLD cycles using the 4-port windbox, protein heated at 50°C for 2 hours, and 10 cycles with only one of the precursors were executed.

Figure 4.27a shows the normalized absorbance at $\lambda=280$ nm for uncoated protein and 10 and 30 MLD cycles. It is possible to observe that the dissolution of the uncoated protein

4.2. MOLECULAR LAYER DEPOSITION ON PROTEINS



(a) Normalized Absorbance at $\lambda=280$ nm as a function of the time until 30 minutes.

(b) Normalized Absorbance at $\lambda=280$ nm as a function of the time until 24 hours.

Figure 4.27: Normalized Absorbance at $\lambda=280$ nm of uncoated protein, 10 and 30 MLD cycles using MC and 12BD as a function of the time (a) until 30 minutes and (b) until 24 hours. The curves were normalized regarding the highest absorbance value.

is fairly fast and reaches full dissolution in just 20 seconds whereas the coated particles seem to take more time, in the order of minutes, to reach full dissolution. The dissolution tests of the 10 MLD cycles and the 30 MLD cycles were done over 24h as depicted in Figure 4.27b and it can be seen that the absorbance after reaching full dissolution starts to slowly decrease over time. Furthermore, during the dissolution test, small strands of material formed and the solution became more blurry over time as shown in Figure 4.28. The formation of strands and the decrease in absorbance occurred during the dissolution test of uncoated protein as well, although in this case the decrease was not significant and it was attributed to the hydrolysis of the protein[126].

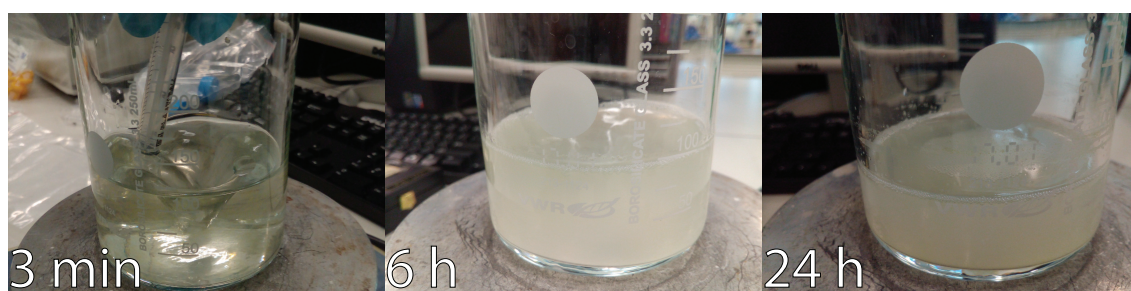


Figure 4.28: Formation of strands during the dissolution of protein coated with 30 MLD cycles using MC and 12BD.

The appearance of strands and the decrease in absorbance at longer dissolution times can be explained by the denaturation of the protein since the solubility of denatured protein tends to be lower than the solubility of the native protein [127, 128]. As previously referred, proteins can suffer denaturation by multiple reasons as pH and the presence of chemicals. Furthermore, several studies in literature report the use of chloride molecules such as guanidinium chloride[121–125] and cetyltrimethylammonium chloride[122] to induce the denaturation of proteins. Hence, the presence of MC, an acid chloride, most

probably, induced the denaturation of the protein causing the observed behaviour. Other reason for this behaviour can be a faster hydrolysis of the protein provoked by the presence of hydrochloric acid (HCl), which is a by-product of the reaction between MC and 12BD. HCl is generally used, together with heating, as an hydrolysis agent[129, 130].

The solution of 30 MLD cycles using MC and 12BD on protein was centrifuged after the 24h to separate the undissolved material from the liquid phase. The mass of undissolved particles was around 15 mg which means that 15% of the particles were not dissolved. This value is comparable with the difference between the maximum absorbance value obtained for bare protein and the absorbance value obtained for 30 MLD cycles coated protein after 24h of stirring. Hence, the results from every dissolution test were normalized regarding to the highest value to avoid the contribution of undissolved material.

Since the FTIR spectra of solely pulsing MC and of the complete MLD process were similar, a dissolution test of both the 10 cycles of solely pulsing one of the precursors and the protein heated at 50°C for 2 hours were performed. These tests were carried out to ensure that the slower dissolution is in fact due to a polyester coating and not to any different factor as denaturation of the protein.

From Figure 4.29, it can be observed that both dissolution curves of the 10 cycles of solely pulsing 12BD and of the heated protein present the same trend and they are not significantly different from the uncoated protein curve. Thus, substantiating that neither the heating at 50°C nor the 12BD have a significant effect on the protein and its dissolution. Nevertheless, a more interesting finding emerges from dissolution curves of 10 MLD cycles and 10 cycles of solely pulsing MC as they almost superimpose over each other. This is further indication that most probably the coating was not deposited on the protein, as shown before in Figure 4.26. In addition, the observed delay in dissolution is due to the presence of MC which possibly denatures the protein and consequently decreases the solubility of the protein.

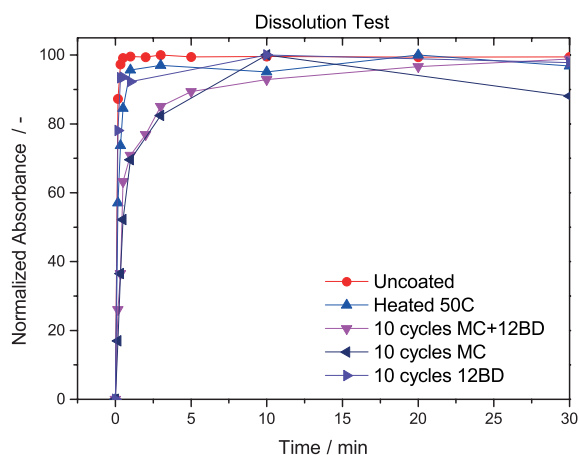


Figure 4.29: Normalized Absorbance at $\lambda=280$ nm of uncoated protein, heated protein, 10 MLD cycles using MC and 12BD and 10 cycles of solely pulsing one of the precursors as a function of the time until 30 minutes. The curves were normalized regarding the highest absorbance value.

4.2.2 Molecular Layer Deposition using Diethyl Succinate as Reactant

Based on the results of MLD growth using DS on TiO₂ P25 nanoparticles described in Subsection 4.1.2, it was determined to use 14BD as co-reactant to study the evolution of the growth of MLD using DS on protein particles. Therefore, to perform this study, an experiment up to 30 cycles (experiment number 24 in Table B.2) was executed. Analogous to previous experiments, some powder was collected at 10 and 20 cycles during the experiment. For this experiment, it was used the 4-port bottom windbox to avoid loss of fluidization during the process. The reactor and windbox temperatures were the same as the temperatures used for 30 MLD cycles on protein using MC, as shown in Table B.2, whereas the temperatures for the precursor bubblers and lines were identical to the temperatures used in 50 MLD cycles on TiO₂ using DS and 14BD.

The subtracted spectra for each sample is shown in Figure 4.30. As it can be seen, there is a peak at 1700 cm⁻¹, as explained in Subsection 4.2.1, this peak is due to the used subtraction factor as it also appears in the spectrum of bare protein as shown in Figure C.3. Hence, there is no clear evidence that a polyester film was indeed deposited during this MLD experiment. This can be due to the fact that a transesterification reaction, as mentioned earlier in Subsection 4.1.2, usually occurs in the presence of a catalyst[92–94] which is not the case of the experiment described above.

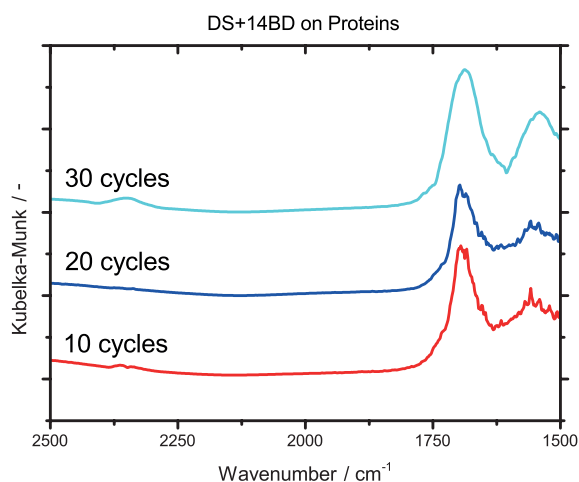
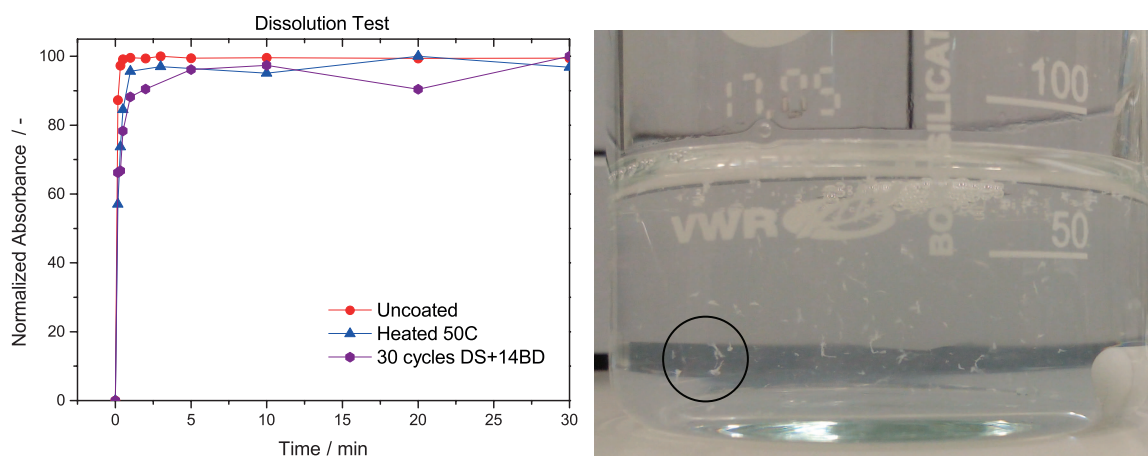


Figure 4.30: Subtracted FTIR spectra obtained for different number of cycles using DS and 14BD on protein. This spectra was subtracted by the bare protein spectrum in Kubelka-Munk units.

Despite the lack of evidence of the deposition of polyester film on protein particles, a dissolution test of the 30 MLD cycles using DS and 14BD was carried out. Only this sample was considered for a dissolution merely because of the higher probability of having polyester deposited onto the particles. Figure 4.31a shows the obtained dissolution curve for 30 MLD cycles using DS and 14BD on protein. A slight delay is observed however it is comparable with the delay caused by heating up the protein at 50°C implying that the delay was entirely caused by heating up the protein rather than by the presence



(a) Normalized Absorbance at $\lambda=280$ nm as a function of the time until 30 minutes.

(b) Strands in solution.

Figure 4.31: Figure (a) shows the normalized absorbance at $\lambda=280$ nm of uncoated protein, 30 MLD cycles using DS and 14BD until 30 minutes. The curves were normalized regarding the highest absorbance value. Figure (b) shows the presence of strands after 30 min of dissolution of protein coated with 30 MLD cycles using DS and 14BD.

of a polyester coating. In Figure 4.31b, small strands are observable in solution after 30 minutes of dissolution which were attributed to the hydrolysis of the protein as discussed for uncoated protein particles. Hence, it was not possible to deposit a polyester film on protein particles using the precursor combination DS and 14BD and thus there was no significant effect on the dissolution of these particles.

CONCLUSION

The main goal of this project was to understand how the growth of polyester films by means of molecular layer deposition evolves on both inorganic (i.e. TiO_2) and organic (protein) particles using different combinations of precursors, namely dichloride/diol and diester/diol.

Firstly, it was shown that to be able to deposit a conformal thin polyester film onto TiO_2 P25 nanoparticles using MC and 12BD, it is crucial that the MLD process has a high enough flow rate ($1.5 \text{ l}\cdot\text{min}^{-1}$) that ensures the transport of the precursor vapour from the bubbler to the reactor and to fluidize the bed without the help of vibration. The flow rate has also to be low enough not to quickly increase the pressure drop and not to form agglomerates. The reactor temperature ($T_{R-401}=100^\circ\text{C}$) should be higher than the bubblers temperature ($T_{B-201}=40^\circ\text{C}$ and $T_{B-301}=90^\circ\text{C}$) to make sure that no condensation of precursors takes place inside the reactor. As this would increase the weight loss while decreasing the amount of polyester chemisorbed on the particles. The use of such conditions allowed the deposition of a conformal polyester film with constant GPC, shown by both FTIR and TGA, onto the TiO_2 particles. The polyester film was also thick enough to be visualized under TEM. However, disagreements in the estimated thickness arised when comparing both the value estimated by TEM (1.34 nm) and the value estimated by TGA (2.77 nm). Therefore, higher number of cycles are necessary to understand the growth of this polyester and to ensure that the carbonaceous coating visualized is indeed polyester.

New combinations of precursors, such as DS + 12BD and DS + 14BD, were tested to understand the feasibility of growing a polyester film by combining a dialkyl diester and a diol. From FTIR and TGA, it was concluded that by using the combination DS and 12BD, a polyester was deposited on the surface of TiO_2 , despite the existence of growth cease after a few cycles. However, the supposed polyester coating was not visualized by tem.

These results were also identical to the results obtained from solely pulsing DS. Instead, by using DS and 14BD, a carbonaceous coating, that was attributed to polyester, was visualized under TEM. However, the TGA and integrated ester C=O peak also showed a cease of growth after a few cycles. The growth cease can be explained by the fact that the transesterification reaction between the diester and the diol usually occurs in the presence of an acid or base catalyst. Thus, different operating conditions should be studied to guarantee that the precursors react with each other.

The influence of the polyester coating in the photocatalytic activity of TiO₂ P25 nanoparticles was subsequently studied by performing a photocatalytic test using a solution of rhodamine B. For the MLD using MC and 12BD, it was observed that rhodamine B was adsorbed on the surface of the particles rather than being degraded. This was supported by the colour of the particles and the solution at the end of the test, which were pink and "orangish" in the case of the 20 and the 50 MLD cycles using MC and 12BD, respectively. Furthermore, the absorbance curve obtained for the 50 MLD cycles coated TiO₂ using MC and 12BD also provided support to the dye adsorption since the characteristic rhodamine B peak at $\lambda=554$ nm was absent right from the start of the test. The obtained absorbance curve was also identical to the absorbance curve obtained for a solution of just water and 50 MLD cycles coated TiO₂ using MC and 12BD. Therefore, for purposes of suppression of the photocatalytic activity, a polyester coating formed by MC and 12BD is not feasible, as it improves the adsorption of the surrounding material. For the MLD using DS and 14BD, a decrease of about 50% in the kinetic constant was observed when both the 5 MLD cycles and the 50 MLD cycles coated particles were present in solution. This is clear evidence that these particles were modified due to the MLD process. Hence, as previously mentioned, the MLD process for depositing polyester films onto TiO₂ should be further studied in order to optimize the operating conditions to reach thicker polyester films.

The operating conditions used in the MLD using MC and 12BD, except the reactor and windbox temperature, were extended towards the protein. To be able to fluidize the protein particles, flow rates higher than 1.5 l.min⁻¹, even with vibration switched on, were needed. Two different approaches were used on this project. On the first, all flow rates were increased during the experiment from 1.5 l.min⁻¹ to 4 l.min⁻¹ however due to the excess precursor pulsed, agglomerates started to be formed causing the rise of the pressure drop in the reactor. On the second one, to avoid sending excess precursor, a 4-port bottom windbox, where the 4th port was utilized to continuously send 5 l.min⁻¹, was used. Although the pressure drop increased in a similar trend as previously, there was no formation of such agglomerates. Furthermore, since proteins can undergo denaturation by several reasons such as temperature and presence of certain chemicals, it was decided to also study the effect of each precursor and temperature. From the FTIR spectra, there was no particular evidence that polyester was deposited onto the surface of proteins in both MLD experiments as their spectra were, in fact, very similar to the spectrum obtained for the experiment of solely pulsing MC. As for the other two spectra, from

only pulsing 12BD and heating up the protein to 50°C, no significant difference from the spectrum obtained for bare protein was observed.

In addition, identical to TiO₂, the combination of a dialkyl diester and a diol, namely DS and 14BD, was tested on protein particles. It was found that most probably no polyester was deposited on the protein particles as there was not a clear ester C=O peak in the FTIR spectra.

The influence of the polyester coating in the dissolution of the proteins was then studied. For the MLD using MC and 12BD, it was found that the delay in the dissolution was mostly caused by the presence of MC which most probably denatures the protein and thus decreases the solubility of the protein. For the MLD using DS and 14BD, the obtained dissolution curve was almost identical to the dissolution curve obtained for heated protein, meaning that the observed small delay was more caused by the heating instead of by a polyester coating. Therefore, for deposition of polyester thin films by means of MLD on proteins, new combinations of precursors need to be studied.

RECOMMENDATIONS

- Study the MLD growth behaviour using malonyl chloride and 1,2-butanediol on TiO_2 for higher number of cycles, i.e. 100 or more, to ensure that the evolution of the thickness is visualized under TEM.
- Study the MLD growth behaviour using malonyl chloride or, if possible, other acyl dichlorides, and different diols, for example ethylene glycol, 1,2-propanediol, 1,3-propanediol or 1,4-butanediol.
- Synthesize MLD films that do not require the use of chloride based precursors as they are not beneficial for both TiO_2 due to the colour change and proteins due to denaturation.

BIBLIOGRAPHY

- [1] R. W. Johnson, A. Hultqvist, and S. F. Bent. “A brief review of atomic layer deposition: from fundamentals to applications.” In: *Materials Today* 17.5 (2014), pp. 236–246. ISSN: 1369-7021. DOI: <https://doi.org/10.1016/j.mattod.2014.04.026>. URL: <http://www.sciencedirect.com/science/article/pii/S1369702114001436>.
- [2] H. Zhou and S. F. Bent. “Fabrication of organic interfacial layers by molecular layer deposition: Present status and future opportunities.” In: *Journal of Vacuum Science and Technology A: Vacuum, Surfaces, and Films* 31.4 (2013), p. 040801. DOI: 10.1116/1.4804609. URL: <http://avs.scitation.org/doi/abs/10.1116/1.4804609>.
- [3] A. C. Jones and M. L. Hitchman. “Chapter 1 Overview of Chemical Vapour Deposition.” In: *Chemical Vapour Deposition: Precursors, Processes and Applications*. The Royal Society of Chemistry, 2009, pp. 1–36. ISBN: 978-0-85404-465-8. DOI: 10.1039/9781847558794-00001. URL: <http://dx.doi.org/10.1039/9781847558794-00001>.
- [4] S. M. George, B. Yoon, and A. A. Dameron. “Surface Chemistry for Molecular Layer Deposition of Organic and Hybrid Organic-Inorganic Polymers.” In: *Accounts of Chemical Research* 42.4 (2009), pp. 498–508. ISSN: 0001-4842. DOI: 10.1021/ar800105q. URL: <https://doi.org/10.1021/ar800105q>.
- [5] A. A. Dameron, D. Seghete, B. B. Burton, S. D. Davidson, A. S. Cavanagh, J. A. Bertrand, and S. M. George. “Molecular Layer Deposition of Alucone Polymer Films Using Trimethylaluminum and Ethylene Glycol.” In: *Chemistry of Materials* 20.10 (2008), pp. 3315–3326. ISSN: 0897-4756. DOI: 10.1021/cm7032977. URL: <https://doi.org/10.1021/cm7032977>.
- [6] S. M. George. “Atomic Layer Deposition: An Overview.” In: *Chemical Reviews* 110.1 (2010), pp. 111–131. ISSN: 0009-2665. DOI: 10.1021/cr900056b. URL: <https://doi.org/10.1021/cr900056b>.
- [7] T. V. Ivanova, P. S. Maydannik, and D. C. Cameron. “Molecular layer deposition of polyethylene terephthalate thin films.” In: *Journal of Vacuum Science and Technology A: Vacuum, Surfaces, and Films* 30.1 (2012), 01A121. DOI: 10.1116/1.3662846. URL: <http://avs.scitation.org/doi/abs/10.1116/1.3662846>.

- [8] G. Ozaydin-Ince, A. M. Coclite, and K. K. Gleason. "CVD of polymeric thin films: applications in sensors, biotechnology, microelectronics/organic electronics, microfluidics, MEMS, composites and membranes." In: *Reports on Progress in Physics* 75.1 (2012), p. 016501. URL: <http://stacks.iop.org/0034-4885/75/i=1/a=016501>.
- [9] P. T. Hammond. "Building biomedical materials layer-by-layer." In: *Materials Today* 15.5 (2012), pp. 196–206. ISSN: 1369-7021. DOI: [https://doi.org/10.1016/S1369-7021\(12\)70090-1](https://doi.org/10.1016/S1369-7021(12)70090-1). URL: <http://www.sciencedirect.com/science/article/pii/S1369702112700901>.
- [10] A. R aupke, F. Albrecht, J. Maibach, A. Behrendt, A. Polywka, R. Heiderhoff, J. Helzel, T. Rabe, H.-H. Johannes, W. Kowalsky, E. Mankel, T. Mayer, P. G orrn, and T. Riedl. "Conformal and Highly Luminescent Monolayers of Alq3 Prepared by Gas-Phase Molecular Layer Deposition." In: *ACS Applied Materials and Interfaces* 6.2 (2014), pp. 1193–1199. ISSN: 1944-8244. DOI: 10.1021/am404918g. URL: <https://doi.org/10.1021/am404918g>.
- [11] L. Mai, Z. Giedraityte, M. Schmidt, D. Rogalla, S. Scholz, A. D. Wieck, A. Devi, and M. Karppinen. "Atomic/molecular layer deposition of hybrid inorganic–organic thin films from erbium guanidinate precursor." In: *Journal of Materials Science* 52.11 (2017), pp. 6216–6224. ISSN: 1573-4803. DOI: 10.1007/s10853-017-0855-6. URL: <https://doi.org/10.1007/s10853-017-0855-6>.
- [12] T. C. Wan, M. K. Y. Kitty, C. K. Wing, M. C. S. K., C. W. Kin, Y. C. Tung, L. Z. Tong, and D. A. B. "Layer-by-Layer Deposition of Rhenium-Containing Hyperbranched Polymers and Fabrication of Photovoltaic Cells." In: *Chemistry – A European Journal* 13.1 (), pp. 328–335. DOI: 10.1002/chem.200600838. eprint: <https://onlinelibrary.wiley.com/doi/pdf/10.1002/chem.200600838>. URL: <https://onlinelibrary.wiley.com/doi/abs/10.1002/chem.200600838>.
- [13] D. H. Kim, S. E. Atanasov, P. Lemaire, K. Lee, and G. N. Parsons. "Platinum-Free Cathode for Dye-Sensitized Solar Cells Using Poly(3,4-ethylenedioxythiophene) (PEDOT) Formed via Oxidative Molecular Layer Deposition." In: *ACS Applied Materials and Interfaces* 7.7 (2015), pp. 3866–3870. ISSN: 1944-8244. DOI: 10.1021/am5084418. URL: <https://doi.org/10.1021/am5084418>.
- [14] S. E. Atanasov, M. D. Losego, B. Gong, E. Sachet, J.-P. Maria, P. S. Williams, and G. N. Parsons. "Highly Conductive and Conformal Poly(3,4-ethylenedioxythiophene) (PEDOT) Thin Films via Oxidative Molecular Layer Deposition." In: *Chemistry of Materials* 26.11 (2014), pp. 3471–3478. DOI: 10.1021/cm500825b. eprint: <https://doi.org/10.1021/cm500825b>. URL: <https://doi.org/10.1021/cm500825b>.
- [15] T. Yoshimura, S. Tatsuura, and W. Sotoyama. "Polymer films formed with monolayer growth steps by molecular layer deposition." In: *Applied Physics Letters* 59.4

- (1991), pp. 482–484. DOI: 10.1063/1.105415. URL: <http://aip.scitation.org/doi/abs/10.1063/1.105415>.
- [16] S. A. Vasudevan, Y. Xu, S. Karwal, H. G.M. E. van Ostaay, G. M. H. Meesters, M. Talebi, E. J. R. Sudholter, and J. Ruud van Ommen. “Controlled release from protein particles encapsulated by molecular layer deposition.” In: *Chemical Communications* 51.63 (2015), pp. 12540–12543. ISSN: 1359-7345. DOI: 10.1039/C5CC03232F. URL: <http://dx.doi.org/10.1039/C5CC03232F>.
- [17] Y. Du and S. M. George. “Molecular Layer Deposition of Nylon 66 Films Examined Using in Situ FTIR Spectroscopy.” In: *The Journal of Physical Chemistry C* 111.24 (2007), pp. 8509–8517. ISSN: 1932-7447. DOI: 10.1021/jp067041n. URL: <https://doi.org/10.1021/jp067041n>.
- [18] D. S. Bergsman, R. G. Closser, and S. F. Bent. “Mechanistic Studies of Chain Termination and Monomer Absorption in Molecular Layer Deposition.” In: *Chemistry of Materials* 0.ja (0), null. DOI: 10.1021/acs.chemmater.8b01468. eprint: <https://doi.org/10.1021/acs.chemmater.8b01468>. URL: <https://doi.org/10.1021/acs.chemmater.8b01468>.
- [19] X. Meng. “An overview of molecular layer deposition for organic and organic–inorganic hybrid materials: mechanisms, growth characteristics, and promising applications.” In: *Journal of Materials Chemistry A* 5.35 (2017), pp. 18326–18378.
- [20] P. Sundberg and M. Karppinen. “Organic and inorganic–organic thin film structures by molecular layer deposition: A review.” In: *Beilstein Journal of Nanotechnology* 5 (2014), pp. 1104–1136. ISSN: 2190-4286. DOI: 10.3762/bjnano.5.123.
- [21] P. W. Loscutoff, H. Zhou, S. B. Clendenning, and S. F. Bent. “Formation of Organic Nanoscale Laminates and Blends by Molecular Layer Deposition.” In: *ACS Nano* 4.1 (2010), pp. 331–341. ISSN: 1936-0851. DOI: 10.1021/nn901013r. URL: <https://doi.org/10.1021/nn901013r>.
- [22] M. Putkonen, J. Harjuoja, T. Sajavaara, and L. Niinisto. “Atomic layer deposition of polyimide thin films.” In: *Journal of Materials Chemistry* 17.7 (2007), pp. 664–669. ISSN: 0959-9428. DOI: 10.1039/B612823H. URL: <http://dx.doi.org/10.1039/B612823H>.
- [23] S. L. D., P. Esa, V. Marko, H. Mikko, and R. Mikko. “Atomic Layer Deposition of Ta₂O₅/Polyimide Nanolaminates.” In: *Chemical Vapor Deposition* 15.7-9 (), pp. 221–226. DOI: 10.1002/cvde.200906770. eprint: <https://onlinelibrary.wiley.com/doi/pdf/10.1002/cvde.200906770>. URL: <https://onlinelibrary.wiley.com/doi/abs/10.1002/cvde.200906770>.
- [24] S. Yoshida, T. Ono, and M. Esashi. “Deposition of conductivity-switching polyimide film by molecular layer deposition and electrical modification using scanning probe microscope.” In: *Micro & Nano Letters* 5.5 (2010), pp. 321–323.

- [25] S. Yoshida, T. Ono, and M. Esashi. "Local electrical modification of a conductivity-switching polyimide film formed by molecular layer deposition." In: *Nanotechnology* 22.33 (2011), p. 335302. URL: <http://stacks.iop.org/0957-4484/22/i=33/a=335302>.
- [26] T. Miyamae, K. Tsukagoshi, O. Matsuoka, S. Yamamoto, and H. Nozoye. "Preparation of Polyimide-Polyamide Random Copolymer Thin Film by Sequential Vapor Deposition Polymerization." In: *Japanese Journal of Applied Physics* 41.2R (2002), p. 746. URL: <http://stacks.iop.org/1347-4065/41/i=2R/a=746>.
- [27] Y.-S. Park, S.-E. Choi, H. Kim, and J. S. Lee. "Fine-Tunable Absorption of Uniformly Aligned Polyurea Thin Films for Optical Filters Using Sequentially Self-Limited Molecular Layer Deposition." In: *ACS Applied Materials & Interfaces* 8.18 (2016). PMID: 27092573, pp. 11788–11795. DOI: 10.1021/acsami.6b02142. eprint: <https://doi.org/10.1021/acsami.6b02142>. URL: <https://doi.org/10.1021/acsami.6b02142>.
- [28] A. Kim, M. A. Filler, S. Kim, and S. F. Bent. "Layer-by-Layer Growth on Ge(100) via Spontaneous Urea Coupling Reactions." In: *Journal of the American Chemical Society* 127.16 (2005). PMID: 15839714, pp. 6123–6132. DOI: 10.1021/ja042751x. eprint: <https://doi.org/10.1021/ja042751x>. URL: <https://doi.org/10.1021/ja042751x>.
- [29] H. Zhou and S. F. Bent. "Molecular Layer Deposition of Functional Thin Films for Advanced Lithographic Patterning." In: *ACS Applied Materials & Interfaces* 3.2 (2011). PMID: 21302918, pp. 505–511. DOI: 10.1021/am1010805. eprint: <https://doi.org/10.1021/am1010805>. URL: <https://doi.org/10.1021/am1010805>.
- [30] H. Zhou, M. F. Toney, and S. F. Bent. "Cross-Linked Ultrathin Polyurea Films via Molecular Layer Deposition." In: *Macromolecules* 46.14 (2013), pp. 5638–5643. DOI: 10.1021/ma400998m. eprint: <https://doi.org/10.1021/ma400998m>. URL: <https://doi.org/10.1021/ma400998m>.
- [31] Y. Chen, B. Zhang, Z. Gao, C. Chen, S. Zhao, and Y. Qin. "Functionalization of multiwalled carbon nanotubes with uniform polyurea coatings by molecular layer deposition." In: *Carbon* 82 (2015), pp. 470–478. ISSN: 0008-6223. DOI: <https://doi.org/10.1016/j.carbon.2014.10.090>. URL: <http://www.sciencedirect.com/science/article/pii/S0008622314010689>.
- [32] D. S. Bergsman, R. G. Closser, C. J. Tassone, B. M. Clemens, D. Nordlund, and S. F. Bent. "Effect of Backbone Chemistry on the Structure of Polyurea Films Deposited by Molecular Layer Deposition." In: *Chemistry of Materials* 29.3 (2017), pp. 1192–1203. DOI: 10.1021/acs.chemmater.6b04530. eprint: <https://doi.org/10.1021/acs.chemmater.6b04530>. URL: <https://doi.org/10.1021/acs.chemmater.6b04530>.

- [33] P. W. Loscutoff, H.-B.-R. Lee, and S. F. Bent. "Deposition of Ultrathin Polythiourea Films by Molecular Layer Deposition." In: *Chemistry of Materials* 22.19 (2010), pp. 5563–5569. ISSN: 0897-4756. DOI: 10.1021/cm1016239. URL: <https://doi.org/10.1021/cm1016239>.
- [34] J. S. Lee, Y.-J. Lee, E. L. Tae, Y. S. Park, and K. B. Yoon. "Synthesis of Zeolite As Ordered Multicrystal Arrays." In: *Science* 301.5634 (2003), p. 818. URL: <http://science.sciencemag.org/content/301/5634/818.abstract>.
- [35] N. M. Adamczyk, A. A. Dameron, and S. M. George. "Molecular Layer Deposition of Poly(p-phenylene terephthalamide) Films Using Terephthaloyl Chloride and p-Phenylenediamine." In: *Langmuir* 24.5 (2008), pp. 2081–2089. ISSN: 0743-7463. DOI: 10.1021/la7025279. URL: <https://doi.org/10.1021/la7025279>.
- [36] Q. Peng, K. Efimenko, J. Genzer, and G. N. Parsons. "Oligomer Orientation in Vapor-Molecular-Layer-Deposited Alkyl-Aromatic Polyamide Films." In: *Langmuir* 28.28 (2012). PMID: 22765908, pp. 10464–10470. DOI: 10.1021/la3017936. eprint: <https://doi.org/10.1021/la3017936>. URL: <https://doi.org/10.1021/la3017936>.
- [37] H.-I. Shao, S. Umemoto, T. Kikutani, and N. Okui. "Layer-by-layer polycondensation of nylon 66 by alternating vapour deposition polymerization." In: *Polymer* 38.2 (1997), pp. 459–462. ISSN: 0032-3861. DOI: [https://doi.org/10.1016/S0032-3861\(96\)00504-6](https://doi.org/10.1016/S0032-3861(96)00504-6). URL: <http://www.sciencedirect.com/science/article/pii/S0032386196005046>.
- [38] T. Yoshimura, S. Tatsuura, W. Sotoyama, A. Matsuura, and T. Hayano. "Quantum wire and dot formation by chemical vapor deposition and molecular layer deposition of one-dimensional conjugated polymer." In: *Applied Physics Letters* 60.3 (1992), pp. 268–270. DOI: 10.1063/1.106681. eprint: <https://doi.org/10.1063/1.106681>. URL: <https://doi.org/10.1063/1.106681>.
- [39] T. Yoshimura, S. Ito, T. Nakayama, and K. Matsumoto. "Orientation-controlled molecule-by-molecule polymer wire growth by the carrier-gas-type organic chemical vapor deposition and the molecular layer deposition." In: *Applied Physics Letters* 91.3 (2007), p. 033103. ISSN: 0003-6951. DOI: 10.1063/1.2754646. URL: <https://doi.org/10.1063/1.2754646>.
- [40] T. Yoshimura and Y. Kudo. "Monomolecular-Step Polymer Wire Growth from Seed Core Molecules by the Carrier-Gas-Type Molecular Layer Deposition." In: *Applied Physics Express* 2.1 (2009), p. 015502. URL: <http://stacks.iop.org/1882-0786/2/i=1/a=015502>.
- [41] T. Yoshimura, R. Ebihara, and A. Oshima. "Polymer wires with quantum dots grown by molecular layer deposition of three source molecules for sensitized photovoltaics." In: *Journal of Vacuum Science & Technology A* 29.5 (2011), p. 051510.

- DOI: 10.1116/1.3620644. eprint: <https://doi.org/10.1116/1.3620644>. URL: <https://doi.org/10.1116/1.3620644>.
- [42] T. Yoshimura and S. Ishii. "Effect of quantum dot length on the degree of electron localization in polymer wires grown by molecular layer deposition." In: *Journal of Vacuum Science & Technology A* 31.3 (2013), p. 031501. DOI: 10.1116/1.4793478. eprint: <https://doi.org/10.1116/1.4793478>. URL: <https://doi.org/10.1116/1.4793478>.
- [43] M. Lillethorup, D. S. Bergsman, T. E. Sandoval, and S. F. Bent. "Photoactivated Molecular Layer Deposition through Iodo Ene Coupling Chemistry." In: *Chemistry of Materials* 29.23 (2017), pp. 9897–9906. DOI: 10.1021/acs.chemmater.7b01780.
- [44] D. M. King, X. Liang, and A. W. Weimer. "Functionalization of fine particles using atomic and molecular layer deposition." In: *Powder Technology* 221 (2012), pp. 13–25. ISSN: 0032-5910. DOI: <https://doi.org/10.1016/j.powtec.2011.12.020>. URL: <http://www.sciencedirect.com/science/article/pii/S0032591011006942>.
- [45] M. Nisula and M. Karppinen. "Atomic/Molecular Layer Deposition of Lithium Terephthalate Thin Films as High Rate Capability Li-Ion Battery Anodes." In: *Nano Letters* 16.2 (2016), pp. 1276–1281. ISSN: 1530-6984. DOI: 10.1021/acs.nanolett.5b04604. URL: <https://doi.org/10.1021/acs.nanolett.5b04604>.
- [46] D. Seghete, B. D. Davidson, R. A. Hall, Y. J. Chang, V. M. Bright, and S. M. George. "Sacrificial layers for air gaps in NEMS using alucone molecular layer deposition." In: *Sensors and Actuators A: Physical* 155.1 (2009), pp. 8–15. ISSN: 0924-4247. DOI: <https://doi.org/10.1016/j.sna.2008.12.016>. URL: <http://www.sciencedirect.com/science/article/pii/S0924424708006080>.
- [47] M. N. Singh, K. S. Y. Hemant, M. Ram, and H. G. Shivakumar. "Microencapsulation: A promising technique for controlled drug delivery." In: *Research in Pharmaceutical Sciences* 5.2 (2010), pp. 65–77. ISSN: 1735-5362 1735-9414. URL: <http://www.ncbi.nlm.nih.gov/pmc/articles/PMC3093624/>.
- [48] J. H. Hamman, G. M. Enslin, and A. F. Kotzé. "Oral Delivery of Peptide Drugs." In: *BioDrugs* 19.3 (2005), pp. 165–177. DOI: 10.2165/00063030-200519030-00003. URL: <https://doi.org/10.2165/00063030-200519030-00003>.
- [49] A. Morlando, V. Sencadas, D. Cardillo, and K. Konstantinov. "Suppression of the photocatalytic activity of TiO₂ nanoparticles encapsulated by chitosan through a spray-drying method with potential for use in sunblocking applications." In: *Powder Technology* 329 (2018). cited By 0, pp. 252–259. DOI: 10.1016/j.powtec.2018.01.057. URL: <https://www.scopus.com/inward/record.uri?eid=2-s2.0-85041417519&doi=10.1016%2fj.powtec.2018.01.057&partnerID=40&md5=543a624a27495627ceb98b50f2946528>.

- [50] A. Regiel-Futyra, M. Kus-Liskiewicz, S. Wojtyła, G. Stochel, and W. Macyk. “The quenching effect of chitosan crosslinking on ZnO nanoparticles photocatalytic activity.” In: *RSC Adv.* 5 (97 2015), pp. 80089–80097. DOI: 10.1039/C5RA12667C. URL: <http://dx.doi.org/10.1039/C5RA12667C>.
- [51] W. A. Lee, N. Pernodet, B. Li, C. H. Lin, E. Hatchwell, and M. H. Rafailovich. “Multicomponent polymer coating to block photocatalytic activity of TiO₂ nanoparticles.” In: *Chem. Commun.* (45 2007), pp. 4815–4817. DOI: 10.1039/B709449C. URL: <http://dx.doi.org/10.1039/B709449C>.
- [52] L. F. Hakim, J. L. Portman, M. D. Casper, and A. W. Weimer. “Aggregation behavior of nanoparticles in fluidized beds.” In: *Powder Technology* 160.3 (2005), pp. 149–160. ISSN: 0032-5910. DOI: <https://doi.org/10.1016/j.powtec.2005.08.019>. URL: <http://www.sciencedirect.com/science/article/pii/S0032591005003888>.
- [53] P. Poodt, J. van Lieshout, A. Illiberi, R. Knaapen, F. Roozeboom, and A. van Asten. “On the kinetics of spatial atomic layer deposition.” In: *Journal of Vacuum Science & Technology A* 31.1 (2013), 01A108. DOI: 10.1116/1.4756692. eprint: <https://doi.org/10.1116/1.4756692>. URL: <https://doi.org/10.1116/1.4756692>.
- [54] H. Van Bui, F. Grillo, and J. R. van Ommen. “Atomic and molecular layer deposition: off the beaten track.” In: *Chem. Commun.* 53 (1 2017), pp. 45–71. DOI: 10.1039/C6CC05568K. URL: <http://dx.doi.org/10.1039/C6CC05568K>.
- [55] D. C. Cameron and T. V. Ivanova. “Molecular Layer Deposition of Polymeric Films.” In: *Meeting Abstracts*. The Electrochemical Society, pp. 1885–1885. ISBN: 2151-2043.
- [56] T. A. Robertson, W. Y. Sanchez, and M. S. Roberts. “Are commercially available nanoparticles safe when applied to the skin?” In: *J Biomed Nanotechnol* 6 (2010). DOI: 10.1166/jbn.2010.1145. URL: <https://doi.org/10.1166/jbn.2010.1145>.
- [57] Y. Wang, J. Li, L. Wang, T. Xue, and T. Qi. “Preparation of Rutile Titanium Dioxide White Pigment via Doping and Calcination of Metatitanic Acid Obtained by the NaOH Molten Salt Method.” In: *Industrial & Engineering Chemistry Research* 49.16 (2010), pp. 7693–7696. DOI: 10.1021/ie1007147. URL: <https://doi.org/10.1021/ie1007147>.
- [58] E. R. Kisin, A. R. Murray, M. J. Keane, X. C. Shi, D. Schwegler-Berry, O. Gorelik, S. Arepalli, V. Castranova, W. E. Wallace, V. E. Kagan, and A. A. Shvedova. “Single-walled carbon nanotubes: geno- and cytotoxic effects in lung fibroblast V79 cells.” In: *J Toxicol Environ Health A* 70 (2007). DOI: 10.1080/15287390701601251. URL: <https://doi.org/10.1080/15287390701601251>.

- [59] Y. Yu, Y. Zhu, J. Guo, H. Yue, H. Zhang, C. Liu, S. Tang, and B. Liang. "Suppression of TiO₂ Photocatalytic Activity by Low-temperature Pulsed CVD-grown SnO₂ Protective Layer." In: *Industrial and Engineering Chemistry Research* (2018). cited By 0; Article in Press. DOI: 10.1021/acs.iecr.8b00270. URL: <https://www.scopus.com/inward/record.uri?eid=2-s2.0-85047750487&doi=10.1021%2facr.8b00270&partnerID=40&md5=1f6963ff51442f894de1f00bf547178f>.
- [60] J. Guo, S. Yuan, Y. Yu, J. R. van Ommen, H. Van Bui, and B. Liang. "Room-temperature pulsed CVD-grown SiO₂ protective layer on TiO₂ particles for photocatalytic activity suppression." In: *RSC Adv.* 7 (8 (2017)), pp. 4547–4554. DOI: 10.1039/C6RA27976G.
- [61] J. Guo, H. Van Bui, D. Valdesueiro, S. Yuan, B. Liang, and J. R. van Ommen. "Suppressing the Photocatalytic Activity of TiO₂ Nanoparticles by Extremely Thin Al₂O₃ Films Grown by Gas-Phase Deposition at Ambient Conditions." In: *Nanomaterials* 8.2 (2018). ISSN: 2079-4991. DOI: 10.3390/nano8020061. URL: <http://www.mdpi.com/2079-4991/8/2/61>.
- [62] X. Liang and A. W. Weimer. "Photoactivity passivation of TiO₂ nanoparticles using molecular layer deposited (MLD) polymer films." In: *Journal of Nanoparticle Research* 12.1 (2010), pp. 135–142. ISSN: 1572-896X. DOI: 10.1007/s11051-009-9587-0. URL: <https://doi.org/10.1007/s11051-009-9587-0>.
- [63] B.-X. Wei, L. Zhao, T.-J. Wang, H. Gao, H.-X. Wu, and Y. Jin. "Photo-stability of TiO₂ particles coated with several transition metal oxides and its measurement by rhodamine-B degradation." In: *Advanced Powder Technology* 24.3 (2013), pp. 708–713. ISSN: 0921-8831. DOI: <https://doi.org/10.1016/j.apt.2012.12.009>. URL: <http://www.sciencedirect.com/science/article/pii/S0921883113000022>.
- [64] H. L. F., K. D. M., Z. Y., G. C. J., G. S. M., and W. A. W. "Nanoparticle Coating for Advanced Optical, Mechanical and Rheological Properties." In: *Advanced Functional Materials* 17.16 (2007), pp. 3175–3181.
- [65] L. J. M. "Introduction." In: *Encapsulation and Controlled Release Technologies in Food Systems*. Wiley-Blackwell, 2016. Chap. 1, pp. 1–15. ISBN: 9781118946893. DOI: 10.1002/9781118946893.ch1. eprint: <https://onlinelibrary.wiley.com/doi/pdf/10.1002/9781118946893.ch1>. URL: <https://onlinelibrary.wiley.com/doi/abs/10.1002/9781118946893.ch1>.
- [66] D. J. McClements and Y. Li. "Structured emulsion-based delivery systems: Controlling the digestion and release of lipophilic food components." In: *Advances in Colloid and Interface Science* 159.2 (2010), pp. 213–228. ISSN: 0001-8686. DOI: <https://doi.org/10.1016/j.cis.2010.06.010>. URL: <http://www.sciencedirect.com/science/article/pii/S0001868610001235>.

- [67] I. Caraballo. "Factors affecting drug release from hydroxypropyl methylcellulose matrix systems in the light of classical and percolation theories." In: *Expert Opinion on Drug Delivery* 7.11 (2010), pp. 1291–1301.
- [68] C. M. Henry. "New Wrinkles in Drug delivery." In: *Chemical & Engineering News* 82.9 (2004), pp. 37–42.
- [69] S. J. Risch. "Encapsulation: Overview of Uses and Techniques." In: *Encapsulation and Controlled Release of Food Ingredients*. Chap. 1, pp. 2–7. DOI: 10.1021/bk-1995-0590.ch001. eprint: <https://pubs.acs.org/doi/pdf/10.1021/bk-1995-0590.ch001>. URL: <https://pubs.acs.org/doi/abs/10.1021/bk-1995-0590.ch001>.
- [70] P. Maljaars, H. Peters, D. Mela, and A. Masclee. "Ileal brake: A sensible food target for appetite control. A review." In: *Physiology and Behavior* 95.3 (2008), pp. 271–281. ISSN: 0031-9384. DOI: <https://doi.org/10.1016/j.physbeh.2008.07.018>. URL: <http://www.sciencedirect.com/science/article/pii/S0031938408002278>.
- [71] S. Frokjaer and D. E. Otzen. "Protein drug stability: a formulation challenge." In: *Nature Reviews Drug Discovery* 4 (2005), p. 298. DOI: 10.1038/nrd1695. URL: <http://dx.doi.org/10.1038/nrd1695>.
- [72] Z. Shariatnia. "Bonding of phosphoramides onto B-C59 nanostructure as drug delivery systems." In: *Physical Chemistry Research* 6.1 (2018), pp. 15–29. DOI: 10.22036/pcr.2017.89125.1389. URL: <https://www.scopus.com/inward/record.uri?eid=2-s2.0-85035805378&doi=10.22036%2fpcr.2017.89125.1389&partnerID=40&md5=95270ed96b64188c4ccb56dcafe723fc>.
- [73] S. K. J. M. K. Chourasia. "Pharmaceutical approaches to colon targeted drug delivery systems." In: *Journal of pharmacy & pharmaceutical sciences* 6.1 (2003), pp. 33–66.
- [74] H. Pu, L. Chen, X. Li, F. Xie, L. Yu, and L. Li. "An Oral Colon-Targeting Controlled Release System Based on Resistant Starch Acetate: Synthetization, Characterization, and Preparation of Film-Coating Pellets." In: *Journal of Agricultural and Food Chemistry* 59.10 (2011), pp. 5738–5745. DOI: 10.1021/jf2005468. URL: <https://doi.org/10.1021/jf2005468>.
- [75] C. Berkland, M. J. Kipper, B. Narasimhan, K. K. Kim, and D. W. Pack. "Microsphere size, precipitation kinetics and drug distribution control drug release from biodegradable polyanhydride microspheres." In: *Journal of Controlled Release* 94.1 (2004), pp. 129–141. ISSN: 0168-3659. DOI: <https://doi.org/10.1016/j.jconrel.2003.09.011>. URL: <http://www.sciencedirect.com/science/article/pii/S0168365903004449>.

- [76] J. Bezemer, R Radersma, D. Grijpma, P. Dijkstra, C. van Blitterswijk, and J Feijen. "Microspheres for protein delivery prepared from amphiphilic multiblock copolymers. 2. Modulation of release rate." In: *Journal of controlled release : official journal of the Controlled Release Society* 67.2-3 (2000), 249—260. ISSN: 0168-3659. DOI: 10.1016/S0168-3659(00)00212-1. URL: [https://doi.org/10.1016/S0168-3659\(00\)00212-1](https://doi.org/10.1016/S0168-3659(00)00212-1).
- [77] D. Valdesueiro, G. M. H. Meesters, M. T. Kreutzer, and J. R. van Ommen. "Gas-Phase Deposition of Ultrathin Aluminium Oxide Films on Nanoparticles at Ambient Conditions." In: *Materials* 8.3 (2015), pp. 1249—1263. ISSN: 1996-1944. URL: <http://www.mdpi.com/1996-1944/8/3/1249>.
- [78] D. A. King and M. G. Wells. "Reaction mechanism in chemisorption kinetics: nitrogen on the 100 plane of tungsten." In: *Proceedings of the Royal Society of London A: Mathematical, Physical and Engineering Sciences* 339.1617 (1974), pp. 245—269. ISSN: 0080-4630. DOI: 10.1098/rspa.1974.0120. eprint: <http://rspa.royalsocietypublishing.org/content/339/1617/245.full.pdf>. URL: <http://rspa.royalsocietypublishing.org/content/339/1617/245>.
- [79] D. Zhang, M. J. Quayle, G. Petersson, J. R. van Ommen, and S. Folestad. "Atomic scale surface engineering of micro- to nano-sized pharmaceutical particles for drug delivery applications." In: *Nanoscale* 9.32 (2017), pp. 11410—11417. ISSN: 2040-3364. DOI: 10.1039/C7NR03261G. URL: <http://dx.doi.org/10.1039/C7NR03261G>.
- [80] A. Tanskanen and M. Karppinen. "Iron-based inorganic-organic hybrid and superlattice thin films by ALD/MLD." In: *Dalton Transactions* 44.44 (2015), pp. 19194—19199. ISSN: 1477-9226. DOI: 10.1039/C5DT02488A. URL: <http://dx.doi.org/10.1039/C5DT02488A>.
- [81] D. L. Zara. "Manufacture and process development of nano-engineered pharmaceutical particles." PhD Thesis Proposal. Doctoral dissertation. 2017.
- [82] N. C. for Biotechnology Information. *Pyromellitic Dianhydride*. Retrieved on July 6, 2018, from https://pubchem.ncbi.nlm.nih.gov/compound/pyromellitic_dianhydride-section=Solubility.
- [83] LookChem.com. *3,3',4,4'-Biphenyltetracarboxylic dianhydride*. Retrieved on July 6, 2018, from <https://www.lookchem.com/3-3-4-4--Biphenyltetracarboxylic-dianhydride/>. 2008.
- [84] C. L. Yaws and M. A. Satyro. "Chapter 1 - Vapor Pressure – Organic Compounds." In: *The Yaws Handbook of Vapor Pressure (Second Edition)*. Gulf Professional Publishing, 2015, pp. 1—314. ISBN: 978-0-12-802999-2. DOI: <https://doi.org/10.1016/B978-0-12-802999-2.00001-5>. URL: <https://www.sciencedirect.com/science/article/pii/B9780128029992000015>.

- [85] LookChem.com. *Malonyl Chloride*. Retrieved on February 14, 2018, from <http://www.lookchem.com/Malonyl-chloride/>. 2008.
- [86] ChemicalBook. *Oxalyl Chloride*. Retrieved on July 6, 2018, from http://www.chemicalbook.com/ChemicalProductProperty_EN_CB7854408.htm. 2017.
- [87] Sigma-Aldrich. *Ethylenediamine*. Retrieved on July 6, 2018, from https://www.sigmaaldrich.com/catalog/product/sial/e26266?lang=en®ion=NL&gclid=EAIaIQobChMI0vmip_CK3AIVQxIbCh2ttw1WEAAYASAAEgIYZfD_BwE. 2018.
- [88] Sigma-Aldrich. *p-Phenylenediamine*. Retrieved on July 6, 2018, from <https://www.sigmaaldrich.com/catalog/product/sigma/p6001?lang=en®ion=NL>. 2018.
- [89] Sigma-Aldrich. *Malonyl Chloride*. Retrieved on July 6, 2018, from <https://www.sigmaaldrich.com/catalog/substance/malonylchloride14095166367811?lang=en®ion=NL>. 2018.
- [90] Sigma-Aldrich. *1,2-butanediol*. Retrieved on July 6, 2018, from https://www.sigmaaldrich.com/catalog/product/sial/18930?lang=en®ion=NL&gclid=EAIaIQobChMI_PG4hvKK3AIVQWYbCh0jIwR-EAAYASAAEgLr1PD_BwE. 2018.
- [91] Sigma-Aldrich. *1,4-butanediol*. Retrieved on July 6, 2018, from <https://www.sigmaaldrich.com/catalog/product/sial/493732?lang=en®ion=NL>. 2018.
- [92] J. R. van Ommen. *Controlled release from particles encapsulated by molecular layer deposition*. Patent WO2016135267A1. Technische Universiteit Delft, 2016.
- [93] J. Clayden, N. Greeves, and S. Warren. *Organic Chemistry*. second. Oxford University Press, 2012.
- [94] E. M. K. Andrew Streitwieser Clayton H. Heathcock. *Introduction to Organic Chemistry*. fourth. Macmillan Publishing Company, 1992.
- [95] E. Industries. *Safety Data Sheet Aeroxide® TiO₂ P 25*. Retrieved on June 10, 2018, from <http://www.thecarycompany.com/media/pdf/specs/sds-evonik-aeroxide-tio2p25.pdf>. 2018.
- [96] J. R. van Ommen, J. M. Valverde, and R. Pfeffer. "Fluidization of nanopowders: a review." In: *Journal of Nanoparticle Research* 14.3 (2012), p. 737. ISSN: 1572-896X. DOI: 10.1007/s11051-012-0737-4. URL: <https://doi.org/10.1007/s11051-012-0737-4>.
- [97] D. Kunii and O. Levenspiel. "Fluidization Engineering (Second Edition)." In: ed. by D. Kunii and O. Levenspiel. Second Edition. Boston: Butterworth-Heinemann, 1991. ISBN: 978-0-08-050664-7.
- [98] J. Werther. "Fluidized-Bed Reactors." In: *Ullmann's Encyclopedia of Industrial Chemistry*. Vol. 15. 2127, pp. 319–366.

- [99] J. Wu, W. Liu, C. Xue, S. Zhou, F. Lan, L. Bi, H. Xu, X. Yang, and F.-D. Zeng. "Toxicity and penetration of TiO₂ nanoparticles in hairless mice and porcine skin after subchronic dermal exposure." In: *Toxicology Letters* 191.1 (2009), pp. 1–8. ISSN: 0378-4274. DOI: <https://doi.org/10.1016/j.toxlet.2009.05.020>. URL: <http://www.sciencedirect.com/science/article/pii/S0378427409002707>.
- [100] U. R. Pothakamury and G. V. Barbosa-Cánovas. "Fundamental aspects of controlled release in foods." In: *Trends in Food Science and Technology* 6.12 (1995), pp. 397–406. ISSN: 0924-2244. DOI: [https://doi.org/10.1016/S0924-2244\(00\)89218-3](https://doi.org/10.1016/S0924-2244(00)89218-3). URL: <http://www.sciencedirect.com/science/article/pii/S0924224400892183>.
- [101] M. Atmane, J. Muriel, S. Joël, and D. Stéphane. "Flavour encapsulation and controlled release – a review." In: *International Journal of Food Science and Technology* 41.1 (), pp. 1–21. DOI: 10.1111/j.1365-2621.2005.00980.x.
- [102] W. Xiaoyuan, Y. Yahong, H. Xiaochen, and Y. Tianli. "Controlled release of protein from core-shell nanofibers prepared by emulsion electrospinning based on green chemical." In: *Journal of Applied Polymer Science* 132.16 (). DOI: 10.1002/app.41811. eprint: <https://onlinelibrary.wiley.com/doi/pdf/10.1002/app.41811>. URL: <https://onlinelibrary.wiley.com/doi/abs/10.1002/app.41811>.
- [103] B. C. Smith. *Fundamentals of Fourier Transform Infrared Spectroscopy*. second. New York: CRC Press, 2011.
- [104] D. W. Mayo, F. A. Miller, and R. W. Hannah. *Course Notes on the Interpretation of Infrared and Raman Spectra*. Hoboken: John Wiley & Sons, Inc., 2003.
- [105] PerkinElmer. *A Beginner's Guide: Thermogravimetric Analysis (TGA)*. Retrieved on May 6, 2018, from https://www.perkinelmer.com/lab-solutions/resources/docs/faq_beginners-guide-to-thermogravimetric-analysis_009380c_01.pdf. 2015.
- [106] I. Anderson Materials Evaluation. *TGA Analysis or Thermogravimetric Analysis*. Retrieved on May 6, 2018, from <http://www.andersonmaterials.com/tga.html>. 2018.
- [107] D. of Physics of University of Warwick. *Transmission Electron Microscopy (TEM)*. Retrieved on May 12, 2018, from <https://warwick.ac.uk/fac/sci/physics/current/postgraduate/regs/mpagswarwick/ex5/techniques/structural/tem/>. 2010.
- [108] B. Fultz and J. M. Howe. *Transmission Electron Microscopy and Diffractometry of Materials*. Third. Springer-Verlag, 2008.
- [109] P. Analytical. *BET*. Retrieved on May 12, 2018, from <http://particle.dk/methods-analytical-laboratory/surface-area-bet-2/>.

- [110] Micromeritics. *Surface Area Instruments*. Retrieved on May 12, 2018, from <http://www.micromeritics.com/Product-Showcase/Surface-Area.aspx>. 2018.
- [111] Q. Wang, D. Ma, and J. P. Higgins. "Analytical method selection for drug product dissolution testing." In: *Dissolution Technologies* 13.3 (2006), p. 6.
- [112] L. van Druten. "Development of Organic Vapor-Phase Deposition Techniques for Drug Encapsulation." Master of Science Thesis in Chemical Engineering. Technische Universiteit Delft, 2018.
- [113] R. Mueller, H. K. Kammler, K. Wegner, and S. E. Pratsinis. "OH Surface Density of SiO₂ and TiO₂ by Thermogravimetric Analysis." In: *Langmuir* 19.1 (2003), pp. 160–165. DOI: 10.1021/1a025785w. eprint: <https://doi.org/10.1021/1a025785w>. URL: <https://doi.org/10.1021/1a025785w>.
- [114] M. D. Porter, T. B. Bright, D. L. Allara, and C. E. D. Chidsey. "Spontaneously organized molecular assemblies. 4. Structural characterization of n-alkyl thiol monolayers on gold by optical ellipsometry, infrared spectroscopy, and electrochemistry." In: *Journal of the American Chemical Society* 109.12 (1987), pp. 3559–3568. DOI: 10.1021/ja00246a011. eprint: <https://doi.org/10.1021/ja00246a011>. URL: <https://doi.org/10.1021/ja00246a011>.
- [115] I. R. Hill and I. W. Levin. "Vibrational spectra and carbon–hydrogen stretching mode assignments for a series of n-alkyl carboxylic acids." In: *The Journal of Chemical Physics* 70.2 (1979), pp. 842–851. DOI: 10.1063/1.437517. eprint: <https://aip.scitation.org/doi/pdf/10.1063/1.437517>. URL: <https://aip.scitation.org/doi/abs/10.1063/1.437517>.
- [116] L. Mazzocchetti, M. Scandola, and A. Pollicino. "Study of the organic–inorganic phase interactions in polyester–titania hybrids." In: *Polymer* 49.24 (2008), pp. 5215–5224. ISSN: 0032-3861. DOI: <https://doi.org/10.1016/j.polymer.2008.09.029>. URL: <http://www.sciencedirect.com/science/article/pii/S0032386108008021>.
- [117] H. Fu, C. Pan, W. Yao, and Y. Zhu. "Visible-Light-Induced Degradation of Rhodamine B by Nanosized Bi₂WO₆." In: *The Journal of Physical Chemistry B* 109.47 (2005). PMID: 16853922, pp. 22432–22439. DOI: 10.1021/jp052995j. eprint: <https://doi.org/10.1021/jp052995j>. URL: <https://doi.org/10.1021/jp052995j>.
- [118] G. Martra. "Lewis acid and base sites at the surface of microcrystalline TiO₂ anatase: relationships between surface morphology and chemical behaviour." In: *Applied Catalysis A: General* 200.1 (2000), pp. 275–285. ISSN: 0926-860X. DOI: [https://doi.org/10.1016/S0926-860X\(00\)00641-4](https://doi.org/10.1016/S0926-860X(00)00641-4). URL: <http://www.sciencedirect.com/science/article/pii/S0926860X00006414>.

- [119] W. B. Kim and J. S. Lee. "Gas phase transesterification of dimethylcarbonate and phenol over supported titanium dioxide." In: *Journal of Catalysis* 185.2 (1999), pp. 307–313.
- [120] J. USA. *JEM-1400 Transmission Electron Microscope*. Retrieved on July 12, 2018, from <https://www.jeolusa.com/PRODUCTS/Transmission-Electron-Microscopes-TEM/120-kV/JEM-1400>. 2018.
- [121] K. Lars. "Protein Unfolding and Denaturants." In: *eLS*. American Cancer Society, 2012. ISBN: 9780470015902. DOI: 10.1002/9780470015902.a0003004.pub2. eprint: <https://onlinelibrary.wiley.com/doi/pdf/10.1002/9780470015902.a0003004.pub2>. URL: <https://onlinelibrary.wiley.com/doi/abs/10.1002/9780470015902.a0003004.pub2>.
- [122] J. Müller, J. Simon, P. Rohne, C. Koch-Brandt, V. Mailänder, S. Morsbach, and K. Landfester. "Denaturation via Surfactants Changes Composition of Protein Corona." In: *Biomacromolecules* 19.7 (2018). PMID: 29660271, pp. 2657–2664. DOI: 10.1021/acs.biomac.8b00278. eprint: <https://doi.org/10.1021/acs.biomac.8b00278>. URL: <https://doi.org/10.1021/acs.biomac.8b00278>.
- [123] C. Camilloni, A. G. Rocco, I. Eberini, E. Gianazza, R. Broglio, and G. Tiana. "Urea and Guanidinium Chloride Denature Protein L in Different Ways in Molecular Dynamics Simulations." In: *Biophysical Journal* 94.12 (2008), pp. 4654–4661. ISSN: 0006-3495. DOI: <https://doi.org/10.1529/biophysj.107.125799>. URL: <http://www.sciencedirect.com/science/article/pii/S0006349508703321>.
- [124] U. Anand and S. Mukherjee. "Binding, unfolding and refolding dynamics of serum albumins." In: *Biochimica et Biophysica Acta (BBA) - General Subjects* 1830.12 (2013). Serum Albumin, pp. 5394–5404. ISSN: 0304-4165. DOI: <https://doi.org/10.1016/j.bbagen.2013.05.017>. URL: <http://www.sciencedirect.com/science/article/pii/S0304416513002134>.
- [125] D. Kishore, S. Kundu, and A. M. Kayastha. "Thermal, Chemical and pH Induced Denaturation of a Multimeric beta-Galactosidase Reveals Multiple Unfolding Pathways." In: *PLOS ONE* 7 (Nov. 2012), pp. 1–9. URL: <https://doi.org/10.1371/journal.pone.0050380>.
- [126] C. I. Butré, P. A. Wierenga, and H. Gruppen. "Influence of water availability on the enzymatic hydrolysis of proteins." In: *Process Biochemistry* 49.11 (2014), pp. 1903–1912. ISSN: 1359-5113. DOI: <https://doi.org/10.1016/j.procbio.2014.08.009>. URL: <http://www.sciencedirect.com/science/article/pii/S1359511314004395>.
- [127] L. Mauer. "PROTEIN | Heat Treatment for Food Proteins." In: *Encyclopedia of Food Sciences and Nutrition (Second Edition)*. Ed. by B. Caballero. Second Edition. Oxford: Academic Press, 2003, pp. 4868–4872. ISBN: 978-0-12-227055-0. DOI:

- <https://doi.org/10.1016/B0-12-227055-X/00988-3>. URL: <http://www.sciencedirect.com/science/article/pii/B012227055X009883>.
- [128] S. Charoenrein and N. Harnkarnsujarit. "Chapter 2 - Food Freezing and Non-Equilibrium States." In: *Non-Equilibrium States and Glass Transitions in Foods*. Ed. by B. Bhandari and Y. H. Roos. Woodhead Publishing Series in Food Science, Technology and Nutrition. Woodhead Publishing, 2017, pp. 39–62.
- [129] D. Roach and C. W. Gehrke. "The hydrolysis of proteins." In: *Journal of Chromatography A* 52 (1970), pp. 393–404. ISSN: 0021-9673. DOI: [https://doi.org/10.1016/S0021-9673\(01\)96589-6](https://doi.org/10.1016/S0021-9673(01)96589-6). URL: <http://www.sciencedirect.com/science/article/pii/S0021967301965896>.
- [130] A. Williams. "AMINO ACIDS | Determination." In: *Encyclopedia of Food Sciences and Nutrition (Second Edition)*. Ed. by B. Caballero. Second Edition. Oxford: Academic Press, 2003, pp. 192–197. ISBN: 978-0-12-227055-0. DOI: <https://doi.org/10.1016/B0-12-227055-X/00039-0>. URL: <http://www.sciencedirect.com/science/article/pii/B012227055X000390>.
- [131] C. Deiana, E. Fois, S. Coluccia, and G. Martra. "Surface Structure of TiO₂ P25 Nanoparticles: Infrared Study of Hydroxy Groups on Coordinative Defect Sites." In: *The Journal of Physical Chemistry C* 114.49 (2010), pp. 21531–21538. DOI: 10.1021/jp107671k. eprint: <https://doi.org/10.1021/jp107671k>. URL: <https://doi.org/10.1021/jp107671k>.
- [132] T. Denaro, V. Baglio, M. Girolamo, G. Neri, F. Deorsola, R. Ornelas, F. Matteucci, V. Antonucci, and A. S. Aricò. "The Influence of Physico-Chemical Properties of Bare Titania Powders Obtained from Various Synthesis Routes on Their Photo-Electrochemical Performance." In: *International Journal of Electrochemical Science* 7 (2012), pp. 2254–2275.
- [133] D. L. Zara. *Calculation of Al₂O₃ monolayers, thickness and GPC from elemental analysis (e.g., ICP, INAA)*. Report. October 6, 2017.
- [134] ACD/I-Lab. *iLab v12*. Retrieved from <https://ilab.acdlabs.com/iLab2/index.php>.
- [135] M. Toledo. *TGA 2*. Retrieved on July 8, 2018, from https://www.mt.com/dam/Analytical/ThermalAnalysis/TA-PDF/TGA2_Broch_EN_30247078_V04.15_Original_38299.pdf. 2015.
- [136] D. C. Harris. *Quantitative Chemical Analysis*. 8th. New York: W. H. Freeman and Company, 2010.
- [137] U. I. Gaya. *Heterogeneous Photocatalysis Using Inorganic Semiconductor Solids*. Nigeria: Springer, 2014.

BIBLIOGRAPHY

- [138] Sigma-Aldrich. *Rhodamine B*. Retrieved on July 8, 2018, from https://www.sigmaaldrich.com/catalog/product/sigma/r6626?lang=en®ion=NL&gclid=EAIaIQobChMIhqG4s7mP3AIVyeFRCh1yuAIFEAAAYASAAEgJIafD_BwE. 2018.

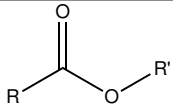
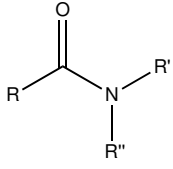
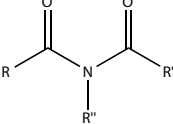
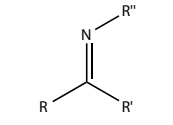
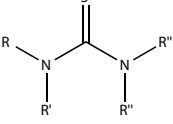
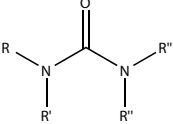
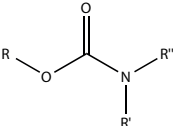
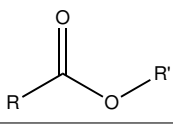


OVERVIEW OF PAST MOLECULAR LAYER DEPOSITION EXPERIMENTS

Table A.1 shows a summary of the current MLD literature and also the type of precursors were used for the deposition of each polymer film.

APPENDIX A. OVERVIEW OF PAST MOLECULAR LAYER DEPOSITION EXPERIMENTS

Table A.1: MLD precursors for: polyester, polyamide, polyimide, polyimine polythiourea, polyurea, polyurethane and polyacrylate. Adapted from D. La Zara[81]

Polymer	Characteristic Linkage	Reactant	Co-Reactant	Literature
Polyester		dichloride, diacid, diester	diol	[7, 16]
Polyamide		dichloride, diacid, diester	diamine	[17, 35–37]
Polyimide		dianhydride	diamine, dichloride	[15, 22–26]
Polyimine		dialdehyde	diamine	[38–42]
Polythiourea		diisothiocyanate	diamine	[33]
Polyurea		diisocyanate	diamine	[21, 27–32]
Polyurethane		diisocyanate	diol	[34]
Polyacrilates		diene	diiodo	[43]

OVERVIEW OF THE EXPERIMENTAL WORK

B.1 Molecular Layer Deposition Experiments

Figure B.1 shows a schematics of the MLD experimental setup. Figure B.2 shows the molecular structure of reactant and co-reactant used in this project. Table B.1 shows the bubbler temperatures and respective vapour pressure for each precursor. Table B.2 shows all the MLD experiments done throughout this project in chronological order and respective operating conditions.

APPENDIX B. OVERVIEW OF THE EXPERIMENTAL WORK

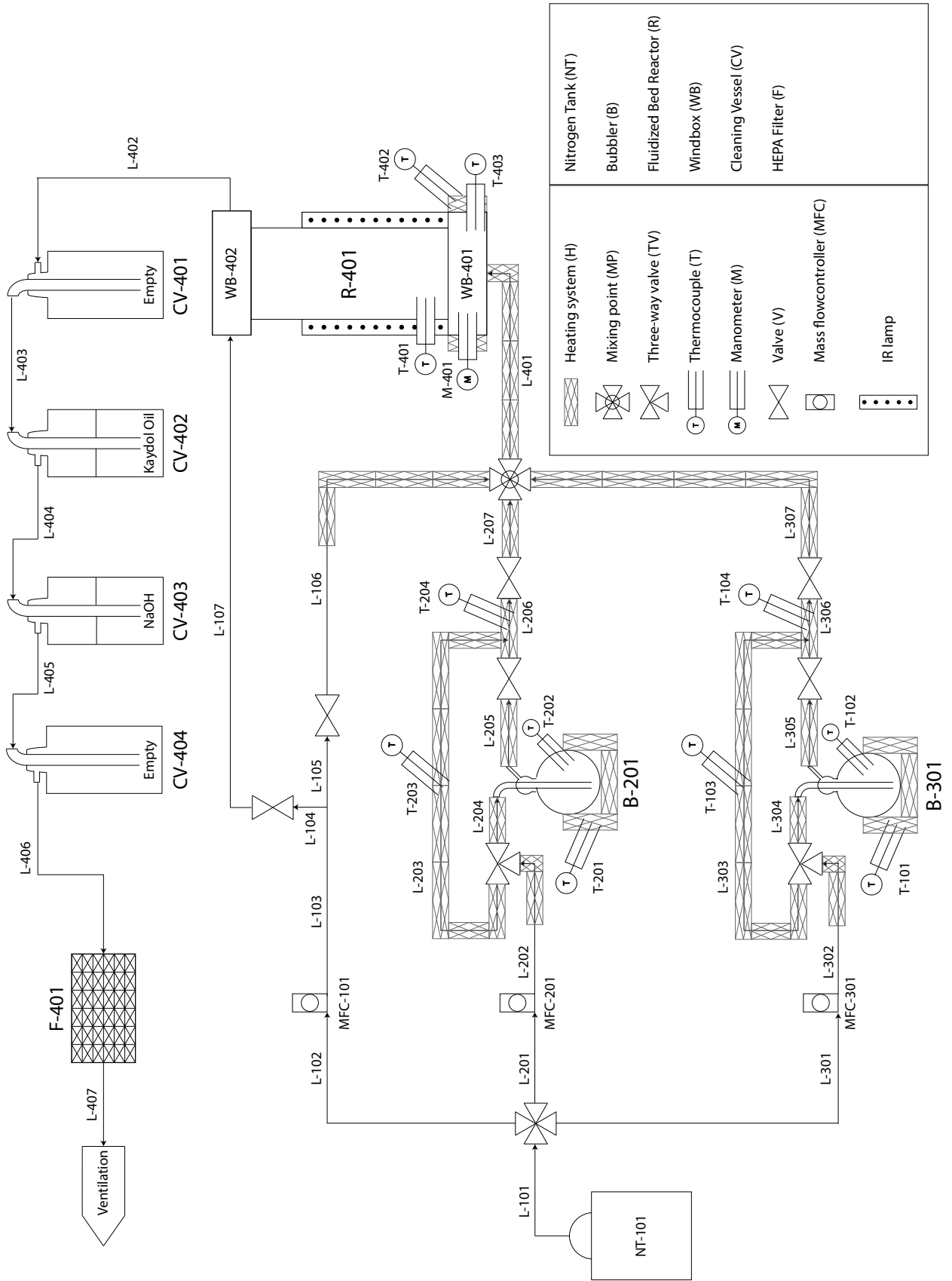
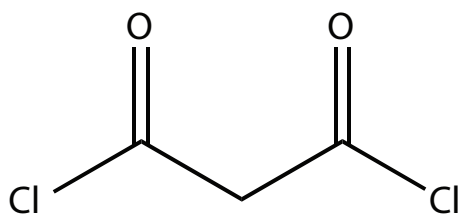
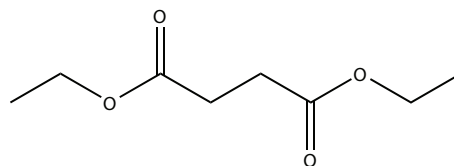


Figure B.1: Molecular Layer Deposition Experimental Setup

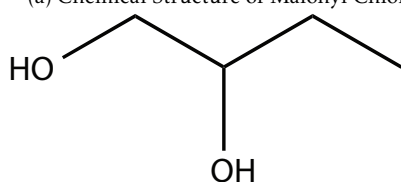
B.1. MOLECULAR LAYER DEPOSITION EXPERIMENTS



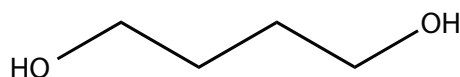
(a) Chemical Structure of Malonyl Chloride.



(b) Chemical structure of Diethyl Succinate.



(c) Chemical Structure of 1,2-butanediol.



(d) Chemical structure of 1,4-butanediol.

Figure B.2: Chemical Structure of both reactants and co-reactants used in this project.

Table B.1: List of precursors with vapour pressure at the temperature inside the bubbler

Precursor	T _{bubbler} /°C	P _v /torr
MC	40	3.16 ¹
DS	95	9.92[84]
12BD	115	46.3 [84]
12BD	90	13.3[84]
14BD	115	10.1[84]

¹at 25 °C

APPENDIX B. OVERVIEW OF THE EXPERIMENTAL WORK

 Table B.2: MLD Experiments by Chronological order. T_{B-201} and T_{L-206} represent the temperatures for the reactant bubbler and line, respectively. T_{B-301} and T_{L-306} represent the temperatures for the co-reactant bubbler and line, respectively. T_{WB-401} and T_{R-401} are temperatures of the bottom windbox and reactor, respectively.

Experiment Number	Reactant	Co-reactant	Substrate	T_{B-201} / °C	T_{B-301} / °C	T_{L-206} / °C	T_{L-306} / °C	T_{WB-401} / °C	T_{R-401} / °C	Time Sequence / min	Flow rate Sequence / $l \cdot min^{-1}$	Vibration	Number of Cycles (collected mid-experiment)
1	MC	12BD	TiO ₂	40	115	100	130	50	50	1/5/1/5	0.5/0.5/1.5/0.5	On/On/On/On	5
2	MC	12BD	TiO ₂	40	115	100	130	50	50	1/5/1/5	0.5/0.5/2/0.5	On/On/On/On	5
3	MC	12BD	TiO ₂	40	115	100	130	50	50	1/5/1/5	0.5/0.5/2.5/0.5	On/On/On/On	5
4	MC	12BD	TiO ₂	40	115	100	130	50	50	1/5/1/5	0.5/0.5/3/0.5	On/On/On/On	5
5	MC	12BD	TiO ₂	40	115	100	130	50	50	1/5/1/5	0.5/0.5/3.5/0.5	On/On/On/On	5
6	MC	12BD	TiO ₂	40	115	100	130	50	50	1/5/1/5	0.5/0.5/1.5/1.5	On/On/On/On	5
7	MC	12BD	TiO ₂	40	115	100	130	50	50	1/5/1/5	0.5/0.5/1.5/1.5	On/On/Off/Off	5
8	MC	12BD	TiO ₂	40	115	100	130	50	50	1/5/1/5	1.5/1.5/1.5/1.5	Off/Off/Off/Off	5
9	MC	12BD	TiO ₂	40	115	100	130	50	50	1/5/1/5	1.5/1.5/1.5/1.5	Off/Off/Off/Off	(5,10,15,18) 30
10	MC	12BD	-	40	115	100	130	50	50	1/5/1/5	5/5/5/5	Off/Off/Off/Off	15
11	-	-	Protein	-	-	-	-	-	-	-/1/-/1	-	On	1 hour
12	MC	12BD	Protein	40	115	100	130	50	50	1/5/1/5	1.5/1.5/1.5/1.5 (increased to 4 at 6th cycle)	On/On/On/On	10
13	-	-	Protein	-	-	-	-	-	-	-	1.5 till 5	On	7 hour
14	MC	12BD	TiO ₂	40	90	100	100	100	100	1/5/1/5	1.5/1.5/1.5/1.5	Off/Off/Off/Off	50
15	MC	12BD	TiO ₂	40	90	100	100	100	100	1/5/1/5	1.5/1.5/1.5/1.5	Off/Off/Off/Off	(5,10,15,20,30,40) 50
16	MC	12BD	TiO ₂	40	90	100	100	50	50	1/5/1/5	1.5/1.5/1.5/1.5	Off/Off/Off/Off	(5,10,15,20,30,40) 50
17	-	-	Protein	-	-	100	130	50	50	-	-	-	2 hours
18	MC	12BD	Protein	40	115	100	130	50	50	1/5/1/5	1.5+(5N ₂)/5/1.5+(5N ₂)/5	On/On/On/On	(10,15,20) 30
19	-	12BD	Protein	-	115	-	130	50	50	-/1/5	-/1/4/4	-/On/On	10
20	MC	-	Protein	40	-	100	-	50	50	1/5/-/	4/4/-/	On/On/-/	10
21	DS	-	TiO ₂	95	-	120	120	105	120	1/5/-/	1.5/1.5/-/	Off/Off/-/	(5,10,15,20,30,40) 50
22	DS	12BD	TiO ₂	95	90	120	120	115	120	1/5/1/5	1.5/1.5/1.5/1.5	Off/Off/Off/Off	(5,10,20,30,40) 50
23	DS	14BD	TiO ₂	95	115	120	120	120	120	1/5/1/5	1.5/1.5/1.5/1.5	Off/Off/Off/Off	(5,10,20,30) 50
24	DS	14BD	Protein	95	115	120	120	50	50	1/5/1/5	1.5+(5N ₂)/1.5+1.5+(5N ₂)/5	On/On/On/On	(10,20) 30

B.2 Photocatalytic Experiments

Table B.3 gives a summary of the conditions used for the photocatalytic tests performed throughout this project.

Table B.3: Photocatalytic Activity Tests by Chronological order

Test Number	Experiment Number	Number of Cycles	Mass of powder / mg	Volume of solution / ml	Dye Concentration / mg.l ⁻¹
1		5	30	30	12
2	15	20	30	30	12
3		50	30	30	12
4		5	30	30	12
5	23	20	15	30	6
6		50	30	30	12

B.3 Dissolution Tests

Table B.4 gives a summary of the conditions used for the dissolutions tests performed throughout this project.

Table B.4: Dissolution Tests by Chronological order

Dissolution Number	Experiment Number	Mass / mg	Volume / ml	Stirrer Speed / Mot	Dissolution Time / h
1	Bare	100	100	8	1
2	12	100	100	8	24
3	Bare	100	100	8	24
4	18	100	100	8	24
5	17 ²	100	100	8	0.5
6	20	100	100	8	0.5
7	19	100	100	8	0.5
8	24	100	100	8	0.5

²Sample kept in the drawer at room temperature

CHARACTERISTICS OF BARE SUBSTRATES

C.1 TiO₂ P25 nanoparticles

The used FTIR spectra and the TGA curves of bare TiO₂ will be discussed. Both the FTIR spectrum measured on November 6, 2017, and the TGA performed on November 22, 2017, were measured by a previous master student during their thesis project.

The FTIR spectra obtained for bare TiO₂ is shown in Figure C.1. Three distinct features are seen in this spectrum are the peaks at 3700-3600 cm⁻¹, the broad peak ranging from 3600-2500 cm⁻¹ and the peaks at roughly 1620 cm⁻¹ and 1540 cm⁻¹. The peaks between 3700-3600 cm⁻¹ can be attributed to -OH groups strongly bonded to the surface of TiO₂ nanoparticles[131]. The broad peak ranging from 3600-2500 cm⁻¹ can be assigned to adsorbed H₂O molecules and hydrogen bonded -OH groups, whereas the

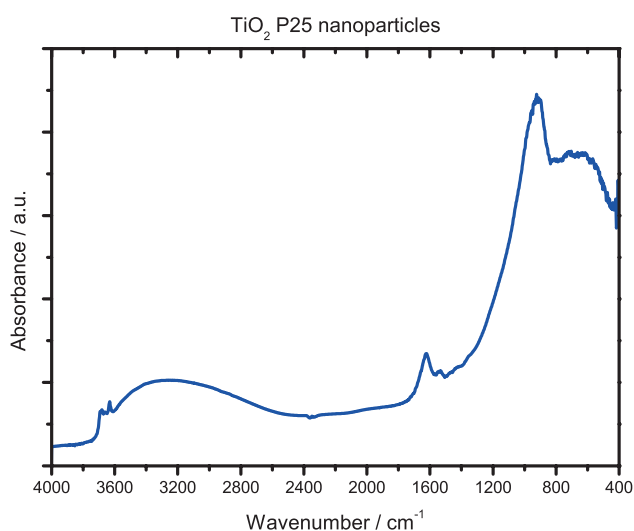


Figure C.1: FTIR spectrum obtained for bare TiO₂ measured in DRIFTS at room temperature.

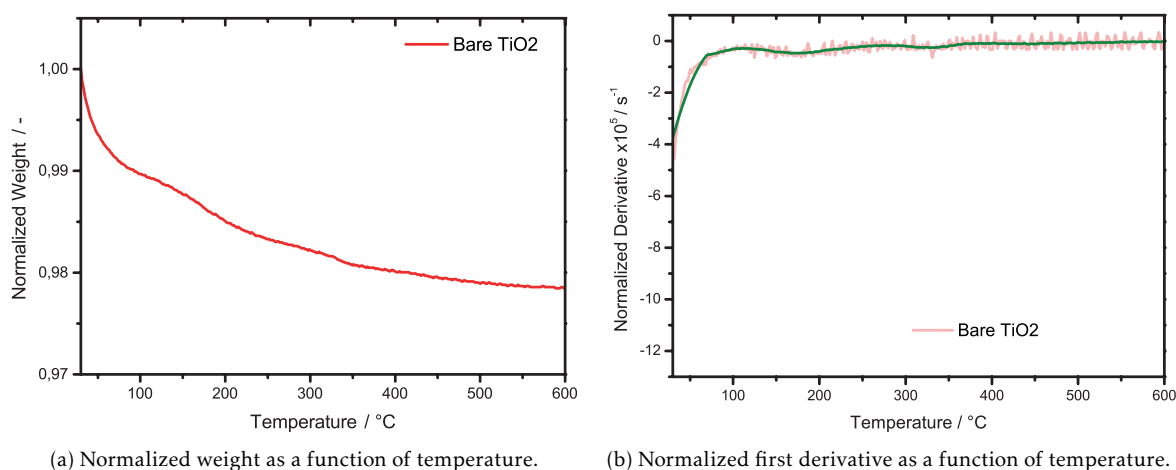


Figure C.2: Figure (a) is the thermogravimetric curve for bare TiO_2 in $100 \text{ ml}\cdot\text{min}^{-1}$ of air with an heating rate of $5^\circ\text{C}\cdot\text{min}^{-1}$ and (b) the respective first order derivative. As the derivative was too noisy (red), it was applied 50pt Savitzky-Golay smoothing in OriginPro 9.0 to observe the fundamental trend (green line).

peak at 1620 cm^{-1} can be fully attributed to adsorbed water. Regardless of fact that the TiO_2 was firstly placed in the oven at 120°C before measuring the FTIR spectrum, it can be inferred that significant adsorption of water is still present in some extent. This shows that upon contacting with air, TiO_2 quickly adsorbs water and therefore heating should be carried out under inert atmosphere before starting an experiment in order to remove more of the adsorbed water[112]. The peak at 1540 cm^{-1} is typically assigned to the carboxylate ion[104], which arises in TiO_2 samples due to carboxylic groups interacting with the TiO_2 surface[116].

The obtained TGA curve is shown in Figure C.2a. The values were normalized with respect to the initial mass. It can be seen that the mass loss is approximately 2% in total. The mass loss up to 120°C is normally attributed in literature to the loss of physisorbed water, whereas at higher temperatures the mass loss is assigned to the loss of hydroxyl groups (chemisorbed water) and combustion of carbonaceous material adsorbed to the surface of TiO_2 [113, 132]. It is expected that the mass loss between $120\text{-}250^\circ\text{C}$ is principally due to the loss of the hydroxyl groups whereas from $250\text{-}500^\circ\text{C}$, it is mainly due to the combustion of carbonaceous material. When analysing the TGA of coated TiO_2 samples, it is therefore relevant to realise that mass loss in the temperature range of 120°C and 500°C may also be attributed to the combustion of the carbonaceous material and not only to polyester coating.

C.2 Protein Particles

In this section, the FTIR spectrum and the results of the dissolution test of uncoated protein particles will be discussed.

In Figure C.3, the region between $3500\text{-}3200 \text{ cm}^{-1}$ can be attributed to both asymmetric and symmetric amine N–H stretches of aliphatic and aromatic amines. In the region

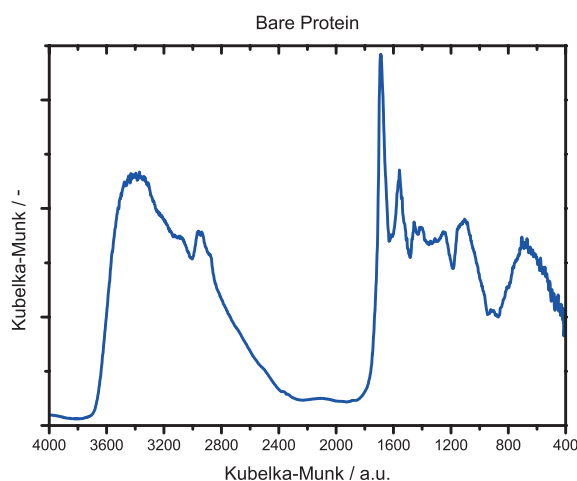
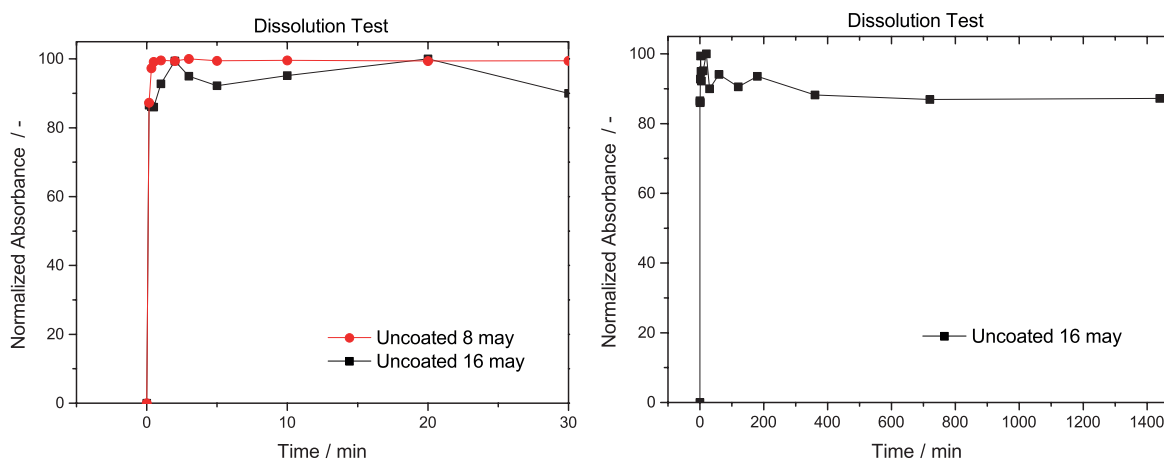


Figure C.3: FTIR spectrum obtained for bare protein measured in DRIFTS at room temperature.

of 3000-2850 cm^{-1} , the aliphatic C-H stretches can be found. Due to the presence of a large peak at 1690 cm^{-1} , the exact identification of an ester C=O peak in the region 1755-1735 cm^{-1} is expected to be more difficult than in TiO_2 nanoparticles as the effect of a nano-sized polyester is too small.

The dissolution of uncoated protein was carried out twice at different instances in time. In Figure C.4a, it can be seen that the dissolution curves are quite similar however the curve of uncoated protein performed on May 16, 2018, shows a few oscillations. Only this dissolution test was performed at a different random place on the table that was under a ventilation shaft. These oscillations were attributed to the position of the stirrer plate regarding the ventilation shaft since it was never observed this type of behaviour during the remaining tests.

In Figure C.4b, it can be observed that there is a slight decrease in absorbance over time which is attributed to the hydrolysis of the protein[126].



(a) Normalized Absorbance at $\lambda=280$ nm as a function of the time until 30 min.

(b) Normalized Absorbance at $\lambda=280$ nm as a function of the time until 24 hours.

Figure C.4: Normalized Absorbance at $\lambda=280$ nm of uncoated protein as a function of the time (a) until 30 minutes and (b) until 24 hours. The curves were normalized regarding the highest absorbance value.

FOURIER TRANSFORM INFRARED SPECTROSCOPY

This appendix describes how the integrated peak areas corresponding to the carbonyl ester peak, C=O, were calculated. This procedure was applied to every sample for which the integrated peak area was obtained unless otherwise specified.

1. The spectra obtained with the Nicolet 8700 Spectrophotometer is given in absorbance units. However, as described in Subsection 2.6.1, for quantitative analysis of the results obtained in DRIFTS mode, the data should be in Kubelka-Munk units. This conversion can be done by OMNIC 8.0 software.
2. Afterward, the spectrum of the bare substrate is subtracted. For both studied particles, it was always used the same bare substrate spectrum. TiO₂ spectrum was measured on November 6, 2017 by another student during their master thesis project and used a subtraction factor of 1. For the protein, the bare spectrum was measured on March 29, 2018 and was used a subtraction factor of 0.6624. This subtraction factor for the protein was chosen in order to maximize the peaks of interest, in this case, the ester C=O peak.
3. Using the peak area tool from OMNIC 8.0, the area of the ester C=O can be calculated from the subtracted spectrum. Figure D.1 shows that both the range and baseline can be adjusted for the calculation of the areas under the ester peak. It was decided to always use the same position for both the range and baseline. The used range and baseline for TiO₂ were from 1808.930 to 1685.507 and 1808.930 to 1724.077 for the protein. These ranges were chosen to not have a skewed baseline.
4. For each analysis, the spectrum was measured twice or thrice depending on the amount of powder remaining at different points in time. Hence, the variability of the measurement, variability in the sample and in the surrounding environment

APPENDIX D. FOURIER TRANSFORM INFRARED SPECTROSCOPY

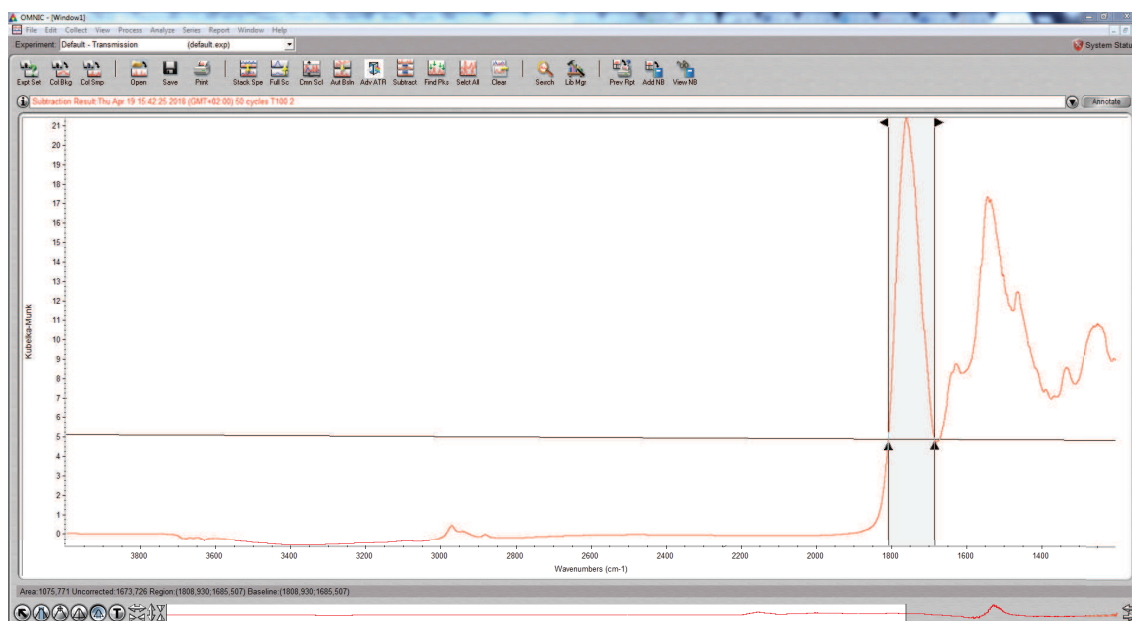


Figure D.1: The procedure used in OMNIC 8.0 to calculate the ester peaks, C=O. As it can be seen, the range and baseline for integration can be adjusted.

are taken into account. Steps 1 to 3 were repeated every time a new measurement was done.

5. Following this, the average peak area (μ) and standard deviation (σ) were calculated for each sample as shown in Equation D.1 and Equation D.2, respectively.

$$\mu = \frac{\sum_i x_i}{N} \quad (\text{D.1})$$

$$\sigma = \sqrt{\frac{\sum_i (x_i - \mu)^2}{N - 1}} \quad (\text{D.2})$$

where x_i represents each calculated area and N is the number of measurements with each sample, N=2 or N=3 in this case

THERMOGRAVIMETRIC ANALYSIS

This analysis gives the percentage of weight loss with increasing temperature[3] allowing to know the amount of deposited material. This is possible as the film is a polyester that will decompose with increasing temperature. Such technique can be only used if the substrate is not heat-sensitive (e.g., TiO₂). Proteins, instead, undergo decomposition/degradation upon high-temperature treatments, thus they cannot be characterized by TGA.

In section E.1, it will be described how to interpret the thermogravimetric curves of MLD coated TiO₂ nanoparticles when analysed in air. In section E.2, it will be described how can the loading and thickness be estimated from the obtained thermogravimetric curves.

E.1 Interpreting a Thermogravimetric Curve

Figure E.1a shows the normalized weight in function of the temperature and Figure E.1b shows the normalized first order derivative in function of the temperature for 50 MLD cycles of MC and 12BD deposited at a reactor temperature of 100°C. The values were normalized according to the initial weight.

By comparing both the TGA curve obtained for bare TiO₂ (Figure C.2a) and the TGA curve obtained for the coated sample, it can be seen that the weight loss up to 120°C is less for the coated sample than for the uncoated one. This indicates that the coating process indeed guarantees that there is less physisorbed water on the particles. Furthermore, the weight loss of the coated sample between 120°C and 500°C is notably more when compared to bare TiO₂. For bare TiO₂, this weight loss is attributed to the loss of chemisorbed water, in the form of –OH surface groups and some carbonaceous residues and adventitious carbon [113, 132]. However, for coated particles this weight loss can be attributed to the loss of coating.

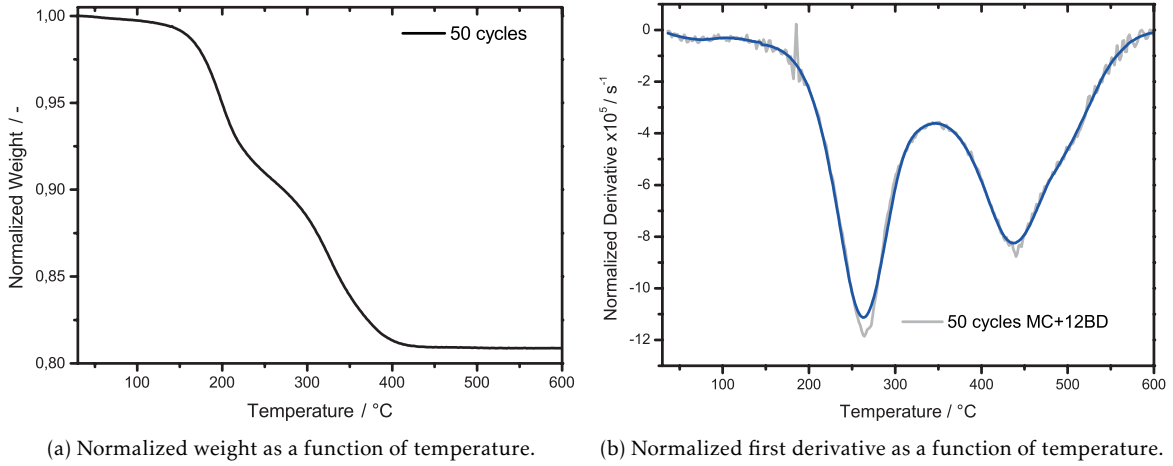


Figure E.1: Thermogravimetric curve for 50 MLD cycles of MC and 12BD on TiO_2 in $100 \text{ ml} \cdot \text{min}^{-1}$ of air with an heating rate of $5^\circ\text{C} \cdot \text{min}^{-1}$ (a) and the respective first order derivative (b). As the derivative was too noisy (grey), it was applied 50pt Savitzky-Golay smoothing in OriginPro 9.0 to observe the fundamental trend (blue line).

E.2 Calculation of the Loading and Thickness

The coating is assumed to be lost between 120°C and 500°C as already described in section E.1. This means that the loading of carbonaceous material initially on the surface can be calculated as:

$$f_{\text{carbon}} = \frac{m_{120} - m_{500}}{m_{500}} \times 100\% \quad (\text{E.1})$$

where m_{120} and m_{500} are the mass at 120°C and 500°C respectively.

In Equation E.1, the loading is expressed with respect to uncoated and dried TiO_2 . As described in section E.1, bare TiO_2 already contains some adventitious carbon. This was calculated as $0.45 \pm 0.005 \text{ wt}\%$ and thus the loading related to the actual coating can be calculated by:

$$f_{\text{coating}} = f_{\text{carbon}} - 0.45 \quad (\text{E.2})$$

It is possible to calculate the thickness of the coating from its loading by methods already developed by this research group[133]. The method was developed to calculate the thickness of Al_2O_3 thin films on spherical particles based on the loading of Al_2O_3 given by e.g. Inductively Coupled Plasma Optical Emission Spectroscopy but it can be easily applied to calculate the thickness of an organic coating with loadings obtained from TGA. Based on this, the thickness can be calculated as:

$$\delta = \frac{d_{\text{core}}}{2} \times \left(\sqrt[3]{\frac{f_{\text{coating}}}{100} \times \frac{\rho_{\text{core}}}{\rho_{\text{coating}}} + 1} - 1 \right) \quad (\text{4.1})$$

The density of the polyester coating is unknown and was predicted using the online available software from ACD/Labs: ACD/I-Lab v12[134]. The predicted polyester densities for each combination of precursors can be seen in Table E.1. The diameter d_{core} can

be calculated as:

$$d_{core} = \frac{6}{\rho_{core} \times S_{BET}} \quad (E.3)$$

where S_{BET} is the surface area obtained from BET. The S_{BET} for TiO₂ P25 nanoparticles, as measured on May 8, 2018, is 52.4 m².g⁻¹.

Table E.1: Predicted polyester densities for each combination of precursors. The densities were estimated by setting up an oligomer consisting of ten repeating units.

Reactant	Co-Reactant	Density / g.cm ⁻³
Malonyl Chloride	1,2-Butanediol	1.283±0.06
Diethyl Succinate	1,2-Butanediol	1.242±0.06
	1,4-Butanediol	1.236±0.06

After calculating the thickness, this value can be plotted as function of the number of cycles. As the film growth should be linear, the value of GPC can be obtained from the slope of the plot as shown in Equation E.4.

$$\delta = GPC.N_C \quad (E.4)$$

where N_C is the number of cycles. The y-intercept of the linear fitting is fixed at zero. This estimated value of GPC can then be compared with the expected GPC for each combination of precursors. The expected values of GPC are present in Table E.2. These values were calculated according to the number of C-O and C-C bond and their typical lengths, which are 0.141 and 0.153 nm respectively[93] and assuming that the polyester monomer is completely linear.

Table E.2: Expected Thickness for one layer of polyester according to each combination of precursors

Reactant	Co-Reactant	Number of C-O bonds	Number of C-C bonds	Expected Thickness /nm
Malonyl Chloride	1,2-Butanediol	4	3	1.023
Diethyl Succinate	1,2-Butanediol	4	4	1.176
	1,4-Butanediol	4	6	1.482

E.3 Error propagation

The error present in the TGA measurements can be traced back to two distinct sources: the error in the external balance with which the initial mass is measured and the error in the internal balance with which variations in mass are established. The former has an uncertainty of 0.1 mg while the internal balance in the TGA machine has weighing accuracy of 0.005%[135].

In Equation E.1, the numerator is calculated by the weight loss measured by the TGA machine, independently of the initial weight set in the machine. The denominator is an absolute weight determined after subtraction of the weight loss measured and therefore it is dependent of the initial mass established. Since the uncertainty in the external balance

for weighing samples between 4-20 mg causes a greater error in the determined mass at 500°C than the relative error of 0.005% caused by the balance of the TGA machine, it is considered that the error in the mass at 500°C is entirely due to the uncertainty of the external balance. For divisions[136], the uncertainty is calculated as:

$$\%e_{final} = \sqrt{\%e_{numerator}^2 + \%e_{denominator}^2} \quad (E.5)$$

where % e represents the relative error of a value. As the relative error in the numerator, which is related to difference determined by the TGA machine, is expected to be much less than the relative error in the denominator, which is related to the error determined by the initial mass weighing, the $\%e_{numerator}$ was neglected. This means that the error of the loading of carbonaceous material originally on the surface can be calculated as:

$$e_{carbon} = \frac{0.1}{m_{500}} \times f_{carbon} \quad (E.6)$$

By applying this method to bare TiO₂, a loading of adventitious carbon of 0.45±0.005%. Since this loading is subtracted from the loading calculated for the MLD coated samples as shown in Equation E.2, the uncertainty in the final loading has to be determined by the propagation of uncertainty during the subtraction. This propagation of uncertainty is given by[136]:

$$e_{final} = \sqrt{e_1^2 + e_2^2} \quad (E.7)$$

where e is the absolute error in the terms subtracted. This means that the absolute error in the coating loading is given by:

$$e_{coating} = \sqrt{e_{carbon}^2 + 0.005^2} \quad (E.8)$$

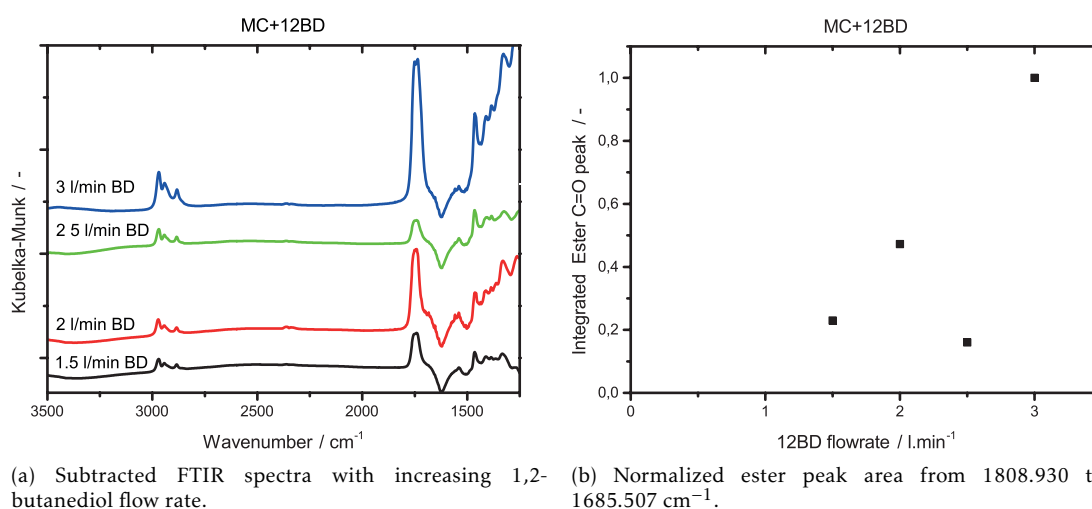
A similar method can be applied to the thickness of the coating determined from the TGA loading. As the thickness is calculated by Equation 4.1, the error can be estimated by:

$$e_{thickness} = \frac{\delta}{100} \times \sqrt{\%e_{d_{core}}^2 + \left(\frac{1}{3} \times \sqrt{\%e_{coating}^2 + \%e_{\rho_{coating}}^2}\right)^2} \quad (E.9)$$

It is assumed that the density of the TiO₂ P25 nanoparticles is a known value, therefore the relative error in d_{core} is equal to the relative error in the S_{BET} following Equation E.5. This error is set to be maximum 5% [112]. Although the standard deviations are given for the density of the coating in Table E.1, it is not known how the software calculated these densities. Thus, a relative error of 10% was assumed in the coating densities.

OPTIMIZATION OF THE OPERATING CONDITIONS

In this appendix the MLD experiments using malonyl chloride and 1,2-butanediol at low reactor temperatures and low flow rates will be briefly discussed. It was known from past experiments in the PPE research group from TU Delft that a 1,2-butanediol flow rate of 1 l.min^{-1} was not enough to ensure that vapour reached the reactor and thus reacting with the malonyl chloride on the surface of TiO_2 P25 nanoparticles. Therefore, this project started by optimizing the diol flow rate. Four MLD experiments of only 5 cycles with different diol flow rates while the remaining steps stayed constant were performed to understand the optimal diol flow rate. The operating conditions for these experiments are described in Table B.2. The different diol rates used were: (i) 1.5 l.min^{-1} , (ii) 2 l.min^{-1} , (iii) 2.5 l.min^{-1} and (iv) 3 l.min^{-1} while the other steps had a flow rate of 0.5 l.min^{-1} .



(a) Subtracted FTIR spectra with increasing 1,2-butanediol flow rate.

(b) Normalized ester peak area from 1808.930 cm^{-1} to 1685.507 cm^{-1} .

Figure F.1: FTIR spectra obtained for different 12BD flow rates. Figure (a) shows the spectra after being subtracted by the bare TiO_2 spectrum in Kubelka-Munk units. Figure (b) shows the peak area under the ester peak from 1808.930 cm^{-1} to 1685.507 cm^{-1} for all samples in (a). They were normalized with respect to the highest one. These spectra were measured once.

The FTIR spectra for each sample are shown in Figure F.1a. It is possible to see that the intensity of the ester C=O peak around 1740 cm^{-1} increases with increasing diol flow rate, except for the sample with $2.5\text{ l}\cdot\text{min}^{-1}$, as shown by the integrated area under the ester peak in Figure F.1b. Furthermore, both the asymmetric and symmetric C–H stretching peaks appear with increasing trend as well. These samples were then analysed under TGA and the obtained thermogravimetric curves are depicted in Figure F.2a. As it can be observed the weight loss for both the samples with $1.5\text{ l}\cdot\text{min}^{-1}$ and $2\text{ l}\cdot\text{min}^{-1}$ are identical whereas for the sample with $3\text{ l}\cdot\text{min}^{-1}$ is higher. Although, the sample with $3\text{ l}\cdot\text{min}^{-1}$ seemed a better option, it was not the chosen diol flow rate as it increased the pressure drop quite quickly. The difference between the weight loss using $1.5\text{ l}\cdot\text{min}^{-1}$ and using $2\text{ l}\cdot\text{min}^{-1}$ was not significant and therefore it was decided to use $1.5\text{ l}\cdot\text{min}^{-1}$ for the following experiments.

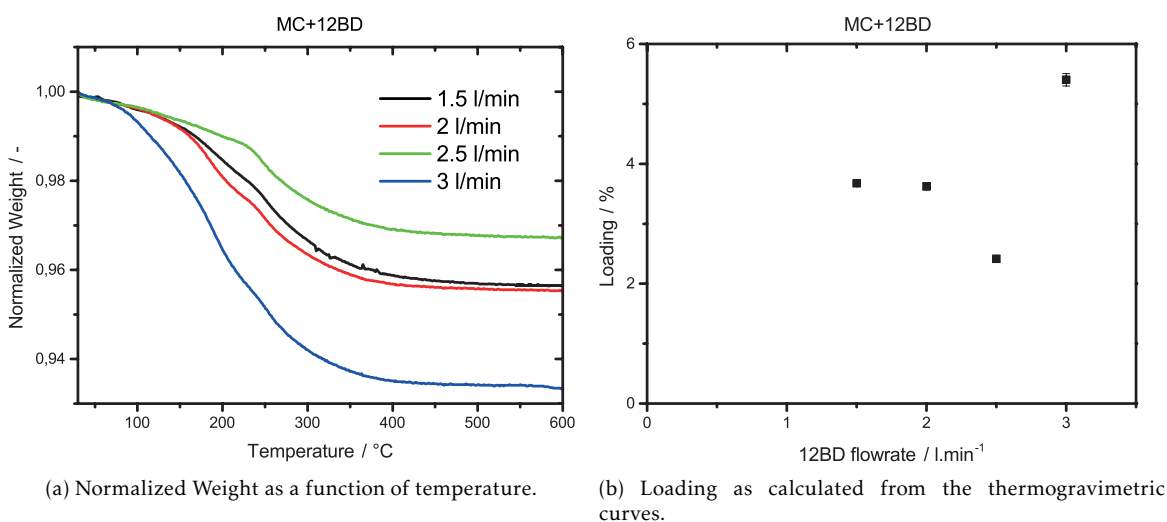


Figure F.2: Thermogravimetric analysis in air with an heating rate of $5^{\circ}\text{C}\cdot\text{min}^{-1}$. Figure (a) shows the normalized weight as a function of temperature for increasing flow rate of 12BD in MLD using MC and 12BD. These curves were consequently used to calculate the loading shown in Figure (b). The error bars, although they are too small to be visible, represent the uncertainty propagated in the TGA measurements.

Following this, it was tested the influence of the flow rate of the other steps of a MLD cycle and the influence of the vibration. Therefore, three experiments up to 5 cycles were carried out. Firstly, the flow rate of the last purge was changed from 0.5 to $1.5\text{ l}\cdot\text{min}^{-1}$ with vibration the whole experiment, then the same flow rate but no vibration during the diol and last purge steps and finally all steps with $1.5\text{ l}\cdot\text{min}^{-1}$ without vibration in any step. The operating conditions were identical to the conditions used previously and are shown in Table B.2. Vibration was switched off since $1.5\text{ l}\cdot\text{min}^{-1}$ is sufficient flow rate to fluidize TiO_2 nanoparticles and it is known that agglomerates are more easily formed when vibration is on for long times.

In Figure F.3 it can be seen the presence of the ester C=O peak around 1740 cm^{-1} and the C–H stretching peaks around $3000\text{--}2850\text{ cm}^{-1}$ [104] in all spectra. Furthermore, these peaks increase when the vibration is switched off and all pulse flow rates are $1.5\text{ l}\cdot\text{min}^{-1}$ as it can be observed in Figure F.3b. The increase of polyester on the surface is

also comproved by the TGA which is shown in Figure F.4. Therefore, the optimal flow rate conditions were determined to be $1.5 \text{ l}\cdot\text{min}^{-1}$ for every pulse and with vibration switched off.

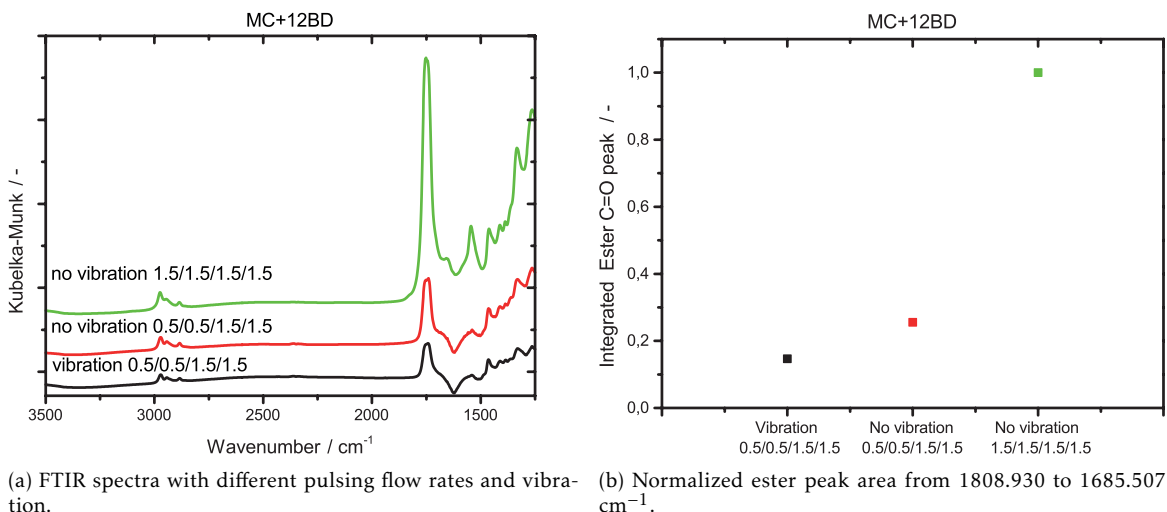


Figure F.3: Figure (a) shows the FTIR spectra after being subtracted by the bare TiO_2 spectrum in Kubelka-Munk units. Figure (b) shows the peak area under the ester peak from 1808.930 cm^{-1} to 1685.507 cm^{-1} for all samples in (a). These spectra were measured once.

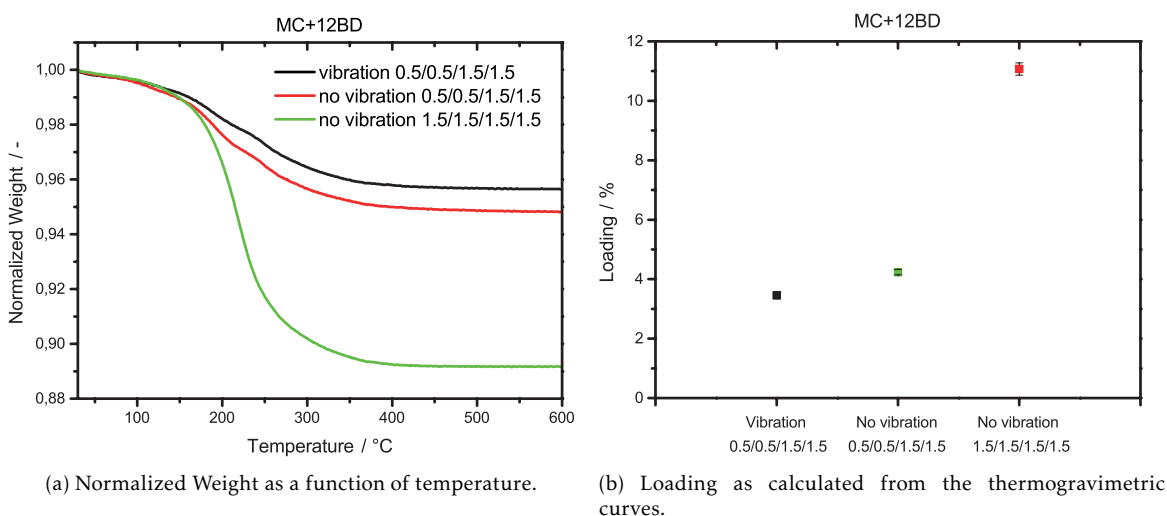
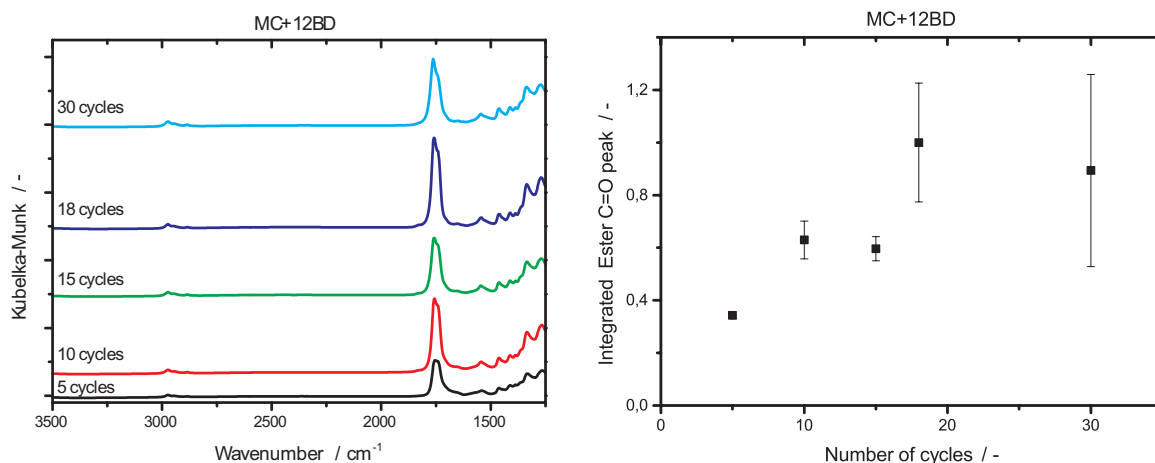


Figure F.4: Thermogravimetric analysis in air with an heating rate of $5^\circ\text{C}\cdot\text{min}^{-1}$. Figure (a) shows the normalized weight as a function of temperature for changing the pulsing flow rates and turning off the vibration. These curves were consequently used to calculate the loading shown in Figure (b). The error bars, although they are too small to be visible, represent the uncertainty propagated in the TGA measurements.

Subsequently, an experiment up to 30 MLD cycles was performed in order to study the MLD growth at low temperatures ($T_{\text{Reactor}}=50^\circ\text{C}$ and $T_{\text{diol}}=115^\circ\text{C}$). All the operating conditions are present in Table B.2. Samples were collected at 5, 10, 15, 18 cycles during the experiment. The experiment was stopped at 18 cycles instead of at 20 cycles due to liquid malonyl chloride raising up through the bubbler's inlet and clogging the lines. Thus, the line was disassembled and the valves cleaned. The experiment was then

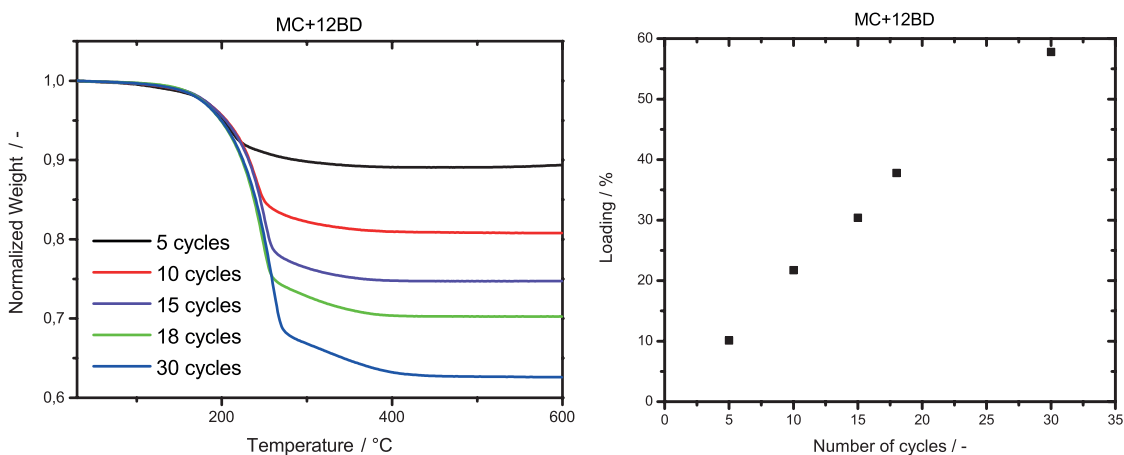
APPENDIX F. OPTIMIZATION OF THE OPERATING CONDITIONS



(a) Subtracted FTIR spectra with increasing number of cycles. (b) Normalized ester peak area from 1808.930 to 1685.507 cm⁻¹.

Figure F.5: FTIR spectra obtained for different number of cycles for MLD using MC and 12BD at $T_{Reactor}=50^{\circ}\text{C}$ and $T_{diol}=50^{\circ}\text{C}$. Figure (a) shows the spectra after being subtracted by the bare TiO₂ spectrum in Kubelka-Munk units. Figure (b) shows the peak area under the ester peak from 1808.930 cm⁻¹ to 1685.507 cm⁻¹ for all samples in (a). The error bar represents the standard deviation.

restarted and stopped at 30 cycles. Figure F.5a shows the FTIR spectra obtained for different number of MLD cycles using malonyl chloride and 1,2-butanediol at $T_{Reactor}=50^{\circ}\text{C}$ and $T_{diol}=115^{\circ}\text{C}$. It can be seen that a peak arises around 1760 cm⁻¹ in all spectra. As mentioned previously in subsection 4.2.1, it is slightly out of the usual range for an ester C=O peak however it can still be attributed to an ester[104]. The intensity of this peak decreases from 18 to 30 cycles as it can be observed in Figure F.5b which may be explained by the problems arising during the experiment. These samples were then analysed under TGA and the respective curves are depicted in Figure F.6a. It can be seen that the weight

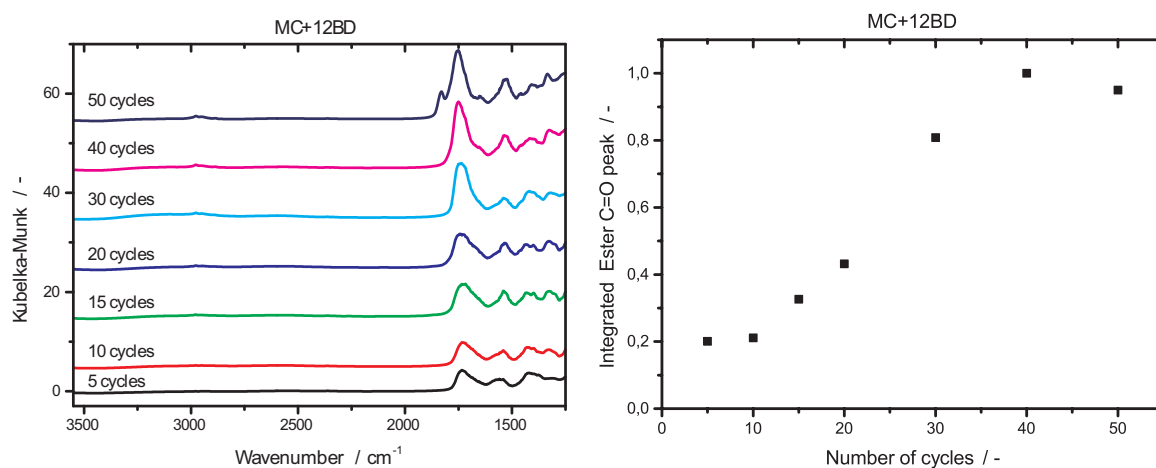


(a) Normalized Weight as a function of temperature. (b) Loading as calculated from the thermogravimetric curves.

Figure F.6: Thermogravimetric analysis in air with an heating rate of 5°C.min⁻¹. Figure (a) shows the normalized weight as a function of temperature for increasing number of MLD cycles on TiO₂ using MC and 12BD at $T_{Reactor}=50^{\circ}\text{C}$ and $T_{diol}=50^{\circ}\text{C}$. These curves were consequently used to calculate the loading shown in Figure (b). The error bars, although they are too small to be visible, represent the uncertainty propagated in the TGA measurements.

loss increases linearly with increasing number of cycles as shown in Figure F.6b. However, there is discordance between the weight loss and the integrated area under the ester peak which indicates that although there is more material deposited on the surface with increasing number of cycles, this additional material is not only polyester coating. The high weight loss can also be attributed to condensation of the precursors in the reactor since the temperature of the diol bubbler is more than two-fold higher than the reactor temperature. Furthermore, the powder was completely orange and quite agglomerated. The sample with 30 MLD cycles was also visualized under TEM despite no pictures are shown in this project. It was not possible to visualize any carbonaceous film around the particles and thus strongly supporting the conclusion that the weight loss was more due to condensation of the precursor than to the formation of polyester.

An experiment using a lower diol bubbler temperature ($T_{diol}=90^{\circ}\text{C}$) and maintaining the reactor temperature was then performed. This experiment was up to 50 cycles and the remaining operating conditions are present in Table B.2. The FTIR spectra is shown in Figure F.7a. The ester C=O peak ($1755\text{-}1735\text{ cm}^{-1}$) can be found in all spectra however a shift to higher wavenumbers is observed which suggests a resonance competition for the lone-pair electrons of the ether oxygen (C–O) by carbonyl group and the new conjugating group as it was earlier described in subsection 4.2.1. The FTIR spectrum of the 50 MLD cycles using malonyl chloride and 1,2-butanediol at $T_{Reactor}=50^{\circ}\text{C}$ and $T_{diol}=90^{\circ}\text{C}$ also shows a peak at 1830 cm^{-1} which it is assigned to an acid chloride implying that there is unreacted malonyl chloride on the particles.



(a) Subtracted FTIR spectra with increasing number of cycles. (b) Normalized ester peak area from 1808.930 to 1685.507 cm^{-1} .

Figure F.7: FTIR spectra obtained for different number of cycles of MLD using MC and 12BD at $T_{Reactor}=50^{\circ}\text{C}$ and $T_{diol}=90^{\circ}\text{C}$. Figure (a) shows the spectra after being subtracted by the bare TiO_2 spectrum in Kubelka-Munk units. Figure (b) shows the peak area under the ester peak from 1808.930 cm^{-1} to 1685.507 cm^{-1} for all samples in (a). These spectra were measured once.

The TGA curves for each samples are shown in Figure F.8a and the respective weight losses are presented in Figure F.8b. It can be seen that the weight loss evolves linearly with increasing cycles. In this experiment, some condensation was observed but unlike

the experiment with $T_{diol}=115^{\circ}\text{C}$, there was not the formation of agglomerates and the colour of the powder was light orange instead of completely orange.

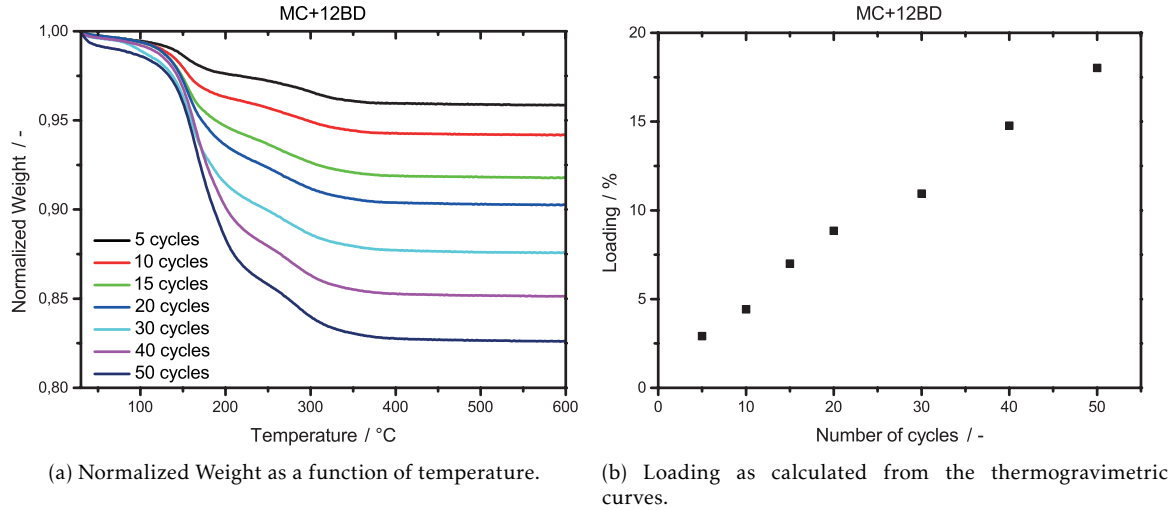


Figure F.8: Thermogravimetric analysis in air with an heating rate of $5^{\circ}\text{C}\cdot\text{min}^{-1}$. Figure (a) shows the normalized weight as a function of temperature for increasing number of MLD cycles on TiO_2 using MC and 12BD at $T_{Reactor}=50^{\circ}\text{C}$ and $T_{diol}=90^{\circ}\text{C}$. These curves were consequently used to calculate the loading shown in Figure (b). The error bars, although they are too small to be visible, represent the uncertainty propagated in the TGA measurements.

From the above described results and the results discussed in subsection 4.1.1, it can be concluded that the optimal temperature conditions to operate the MLD set-up are $T_{Reactor}=100^{\circ}\text{C}$ and $T_{diol}=90^{\circ}\text{C}$ since in this manner it was verified that little condensation occurred in the reactor and thus obtaining a more successful gas-phase deposition.

P H O T O C A T A L Y T I C T E S T

G.1 Calculation of Kinetic Constant from UV-Vis

The rate of degradation of a contaminant, in this case rhodamine B, is usually assumed to follow a Langmuir adsorption model[137] as shown in Equation G.1.

$$r = -\frac{dC}{dt} = k_1 \times \frac{K_{ads}C}{K_{ads}C + 1} \quad (G.1)$$

where C is the concentration of rhodamine B, k_1 is the kinetic constant and K_{ads} is the adsorption constant of rhodamine B. In dilute solutions of the contaminant where $C < 10^{-3} \text{ mol.dm}^{-3}$, $K_{ads}C$ becomes $\ll 1$ and the reaction follows pseudo-first order kinetics. In more concentrated solutions such as $C < 5 \times 10^3 \text{ mol.dm}^{-3}$, $K_{ads}C$ becomes $\gg 1$ and the reaction becomes pseudo-zero order. Since rhodamine B has molecular mass of $479.01 \text{ g.mol}^{-1}$ [138] and the concentration of rhodamine B used was 12 mg.l^{-1} , this corresponds to a molar concentration of $2.5 \times 10^{-5} \text{ mol.l}^{-1}$. Therefore, it was assumed that the reaction followed a pseudo-first order kinetics and Equation G.1 can be written as Equation G.2.

$$\frac{dC}{dt} = -kC \quad (G.2)$$

where k is the pseudo-first order kinetic constant. By integrating Equation G.2 as shown in Equation G.3, Equation G.4 is obtained.

$$\int_{C_0}^{C_t} \frac{1}{C} dC = \int_0^t k dt \quad (G.3)$$

$$\ln\left(\frac{C_0}{C_t}\right) = k \times t \quad (G.4)$$

where C_0 and C_t are the initial concentration and concentration at time t of rhodamine B, respectively.

From Equation 2.4, the concentration is directly proportional to the absorbance for a constant length of the cuvette. Hence, Equation G.4 can be written as:

$$\ln\left(\frac{A_0}{A_t}\right) = k \times t \quad (4.2)$$

Therefore, the kinetic constant k can be obtained by plotting $\ln\left(\frac{A_0}{A_t}\right)$ in function of the time, where A_0 is the absorbance at $\lambda = 554$ nm at 0 minutes and A_t is the absorbance at $\lambda = 554$ nm at time t . The y-intercept was always fixed to 0.